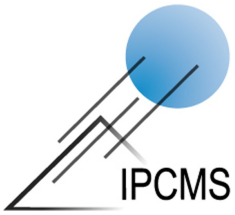

UNIVERSITÉ DE STRASBOURG

École Doctorale de Physique et Chimie-Physique

Institut de Physique et Chimie des Matériaux de Strasbourg

Thèse de doctorat présentée par

Monica SANCHES PIAIA

Pour l'obtention du titre de:

Docteur de l'Université de Strasbourg

Discipline: Physique de la matière condensée

Mélange à quatre ondes magnéto-optique femtoseconde dans les films de Grenat

Soutenue le 18 juillet 2014 devant le jury composé de:

Dr. Niels KELLER	Rapporteur externe, Université Versailles Saint-Quentin
Dr. Fabrice VALLÉE	Rapporteur externe, Université Claude Bernard Lyon-1
Dr. Pierre GILLIOT	Examinateur interne, Université de Strasbourg
Dr. Jean-Yves BIGOT	Directeur de thèse, Université de Strasbourg
Dr. Bernard BARBARA	Membre invité, Institut Néel, Grenoble
Dr. Marie BARTHELEMY	Membre invité, Université de Strasbourg

Abstract

The studies on the interaction of light with magnetic materials has been motivated since the last two decades with different motivation as pulse propagation studies, magnetic imaging purposes and to improve the speed of writing and reading data. The storage media commonly used are based on the movement of a magnetic head along a magnetic surface. The magnetization of the sub-nanometer regions is changed with magnetic field pulses.

In addition to the fragility, the low writing frequency of this kind of media motivates the use of light pulses to induce the change of the magnetization.

Since 1996, when it was proved that a ferromagnetic nickel film can be demagnetized using $60fs$ laser pulses [1], this research field has been widely explored. How the light pulses excite the material and how the material relaxes to its fundamental state are mechanisms that have been studied with techniques like the pump and probe. It consists in using a pulse to excite the material and a second pulse, retarded by a well-known variable delay, to probe the state of the material in different instants of the phenomenon. This technique is used in a Faraday [2] or Kerr [3] configurations, which means the probe beam will present a different polarization state with and without the presence of the pump. The probe is analysed in transmission (Faraday) or reflection (Kerr) using techniques of beam polarization analysis. This change can be explained by a nonlinear interaction of the field with the material responsible for generating an emitted field proportional to the polarization state of the sample. With these techniques it is possible to study the evolution in time of the magnetization behavior.

In metalic materials, in the first $20fs$, the electrons are excited by the laser pulse and acquire energy higher than the Fermi level, there is no temperature description for this regime. The electrons interact with each other via the Coulomb interaction during some hundreds of femtoseconds (thermalization time). When they are all thermalized and in a Fermi-Dirac distribution, the magnetization modulus has been reduced. The energy starts to be dissipated to the lattice in the picosecond scale via spin-phonon scattering. In this time scale, the magnetization precession takes place, being the precession frequency in the GHz scale. The precession damping happens in a temporal range from $50ps$ to $5ns$. The energy is then dissipated to the environment.

Let us mention that the ultrafast regime of charges and spins relaxation involves highly nonequilibrium densities of interacting electrons which require many-body theory modeling or density functional theory approaches in the dynamical regime. Such procedures are difficult and seldom provide realistic predictions. Therefore, phenomenological approaches like those based on temperature dependent coupled baths are rather privileged.

The goal of this thesis is to study the magneto-optical effects occurring before the thermalization time. In this time range, the system regime is still in phase with the laser field and is called coherent.

The simplest way to model the magneto-optical response of a material is to consider a hydrogen-like atom. When in an eight-level system, its behavior can be described by a hamiltonian composed by a nonperturbed term and a term that contains its interaction with the laser field. The evolution in time of the electron in this system is given by the Liouville formalism, with the evolution of the density matrix. The density matrix describes the probability of finding the system in different quantum states. Its diagonal elements represent the population of each level and its nondiagonal elements show the interferences between two states and are called coherences. The populations relaxation to the fundamental decays with time T_1, the lifetime of the excited level, and the coherences, with time T_2, much shorter than T_1.

In 2009, our group has demonstrated the existance of a coherent component present in the magneto-optical response obtained in a Kerr configuration [4]. This configuration allows to measure signals where the populations and coherences dynamics are overlapped. It was shown that this coherent component is polarization dependent and is more important when pump and probe polarizations are paralell, being reduced when the polarizations are perpendicular. This way, substracting one from the other, it is possible to extract the coherent component.

In this thesis, we show that it is possible to measure directly the coherent dynamics in a magneto-optical four-wave mixing configuration. The four-wave mixing is a well-known third order self-diffraction effect based on the interaction of three fields in a medium. The two first ones create a grating responsible for diffracting the third one in different directions, according to the orders of diffraction. Being $\overrightarrow{k}_p$ the pump direction and $\overrightarrow{k}_s$ the probe direction, we show that the magneto-optical time-resolved pump and probe signals measured in the direction $2\overrightarrow{k}_p - \overrightarrow{k}_s$ and $2\overrightarrow{k}_s - \overrightarrow{k}_p$ in the two-beam configuration do not contain the populations contribution as the Faraday or the Kerr signals. The same can be reproduced in the three-beam configuration.

In a first time, we have used $120fs$ amplified pulses to prove the feasibility of this technique by measuring the Faraday and magneto-optical four-wave mixing signals generated on a bismuth-doped garnet sample of formula $(GdTmPrBi)_3(FeGa)_5O_{12}$.

Ferromagnetic garnets have been elaborated and studied since the 1950s. They are interesting for presenting important magneto-optical properties. Having general formula of $(X^{3+})_3(Fe^{3+})_2(Fe^{3+})_3O_{12}$, the garnet structure is made by three sublattices: the dodecahedral, the octahedral and tetrahedral (each one of the parenthesis of the general formula represents, in order, a sublattice). The ions inside the octahedral and tetrahedral sites are aligned in a ferromagnetic way, while the two sublattices are coupled in an antiferromagnetic way. The different number of tetrahedral and octahedral sites results in a non compensation of the magnetic moment and in the spontaneous magnetization of the material.

The ferromagnetic garnet structure accepts several substitutions. Bismuth substitution is responsible for increasing the magneto-optical effects because it induces the splitting of the iron orbitals. This effect induces charge transfer between the oxygen and iron orbitals.

The ferromagnetic garnet studied in this thesis [5] was produced by liquid phase epitaxy [6] by the group of Dr. Bernard Barbara in Grenoble. The $7\mu m$ film was grownth on both sides of the $500\mu m$ gadolinium gallium garnet substrate [7].

The magneto-optical four-wave mixing signals generated in a two-beam configuration in this garnet sample in the $2\overrightarrow{k}_p - \overrightarrow{k}_s$ direction with $120fs$ pulses have proved the efficacity of the technique in measuring directly the coherent component of the magneto-optical response. However, the time resolution was not enough to measure the coherence time T_2.

We also show that it is possible to study populations and coherences dynamics via a magneto-optical four-wave mixing experiment in the three-beam configuration. The populations dynamics is obtained by fixing the delay τ between the first and the second pulses and varying the delay T between the first and the third pulses. The coherences dynamics is obtained by fixing T and varying τ. These experiments were performed with $47fs$ pulses, what limits the time resolution and does not allow either to obtain T_2, but they show how complete the three-beam configuration is to study the populations and coherences dynamics.

To improve the time resolution, we have used $10fs$ nonamplified pulses to measure the magneto-optical four-wave mixing signals emitted in the directions $2\overrightarrow{k}_p - \overrightarrow{k}_s$ and $2\overrightarrow{k}_s - \overrightarrow{k}_p$. The combination of the coherent response with characteristic time T_2 with the pulse duration creates a time shift between the signals obtained in these two directions. This shift, as the exponential decay of the signal, gives access to the time T_2. We have found that this shift is of $(1,3 \pm 0,5)fs$ for the magneto-optical response, that describes the spins behavior, and of $(1,7 \pm 0,5)fs$ for the optical response, that describe the charges behavior. It is not possible then to affirm that these times are equal or not due to their close values. Using a fit function generated by the convolution of a gaussian pulse and an exponential decay with time T_2 it is possible to obtain $2fs \leq T_2 \leq 3,5fs$.

Being the temporal phase of extreme importance when dealing with sub-$10fs$ laser pulses, we have performed simulations of the four-wave mixing signal considering a two-level system and a homogeneous broadening generated with pulses with different phases. We show that the center of the signal depends on the duration of the pulse considered to measure it and that for the same coherence time, pulses with different phases generate different shifts between the directions $2\overrightarrow{k}_p - \overrightarrow{k}_s$ and $2\overrightarrow{k}_s - \overrightarrow{k}_p$. This shows that it is important to have phase and amplitude characterization for the pulses used to measure this signals. The intensity autocorrelation trace obtained from the experimental pulses is very similar to the simulated trace that takes into account no spectral phase, what allows one to say that, in our case, the phase of the experimental pulse is minimal and does not play an important role in the determination of the center of the signal.

In conclusion, we show that it is possible to measure the coherent magnetization dynamics of a bismuth-doped garnet sample in a magneto-optical four-wave mixing configuration with enough time resolution to estimate the coherence time.

Résumé

Les études sur l'interaction de la lumière avec des matériaux magnétiques sont motivé depuis les deux dernières décennies par différentes raisons comme les études de propagation d'impulsion, à des fins d'imagerie magnétique et pour améliorer la vitesse de d'écriture et de lecture de données. Les techniques de stockage couramment utilisés sont fondés sur le mouvement d'une tête magnétique le long d'une surface magnétique. L'aimantation des régions sous-nanométrique est modifiée par des impulsions de champ magnétique.

En plus de la fragilité, la basse fréquence d'écriture de ce type de support justifie l'utilisation d'impulsions de lumière pour induire le changement de l'aimantation.

Depuis 1996, quand il a été prouvé qu'un film de nickel ferromagnétique peut être désaimanté en utilisant des impulsions laser de $60 fs$ [1], ce domaine de recherche est largement exploré. Grâce aux techniques pompe-sonde, il est possible d'étudier les mécanismes qui régissent l'excitation du matériau par une impulsion lumineuse ainsi que la relaxation de la matière vers l'état fondamental. Ce procédé expérimental consiste à utiliser une première impulsion pour exciter le matériau et une seconde, retardée d'un durée variable connue, pour sonder l'état de la matière à des différents instants du phénomène. Cette technique est utilisée dans une configuration Faraday [2] ou Kerr [3], ce qui signifie que le faisceau sonde présentera un état de polarisation différent avec et sans la présence de la pompe. La sonde est analysée en transmission (Faraday) ou en réflexion (Kerr) en utilisant des techniques d'analyse de polarisation du faisceau. Ce changement peut être expliqué par une interaction non-linéaire du champ avec le matériau qui induit un champ proportionnelle à l'état de polarisation de l'échantillon. Avec ces techniques, il est possible d'étudier l'évolution dans le temps du comportement de l'aimantation.

Dans les matériaux métallique, pendant les premières $20 fs$, les électrons sont excités par l'impulsion laser et acquièrent une énergie plus élevée que le niveau de Fermi, il n'y a pas de description de température pour ce régime. Les électrons interagissent les uns avec les autres via l'interaction de Coulomb pendant quelques centaines de femtosecondes (temps de thermalisation). Une fois thermalisés, les électrons adoptent une distribution de Fermi-Dirac, ce qui correspond à une réduction du module de l'aimantation. L'énergie

commence alors à se dissiper vers le réseau en quelques picosecondes via des interactions spin-phonon. C'est à cette échelle de temps qu'il est possible d'observer de phénomène de la précession de l'aimantation. L'amortissement de la précession se détend entre $50ps$ et $5ns$. L'énergie se dissipe finalement vers l'environnement.

Notons que le régime ultra-rapide de relaxation des charges et des spins implique des densités d'électrons qui interagissent hors équilibre nécessitant une modélisation de la théorie à plusieurs corps ou des approches de théorie de la densité fonctionnelle dans le régime dynamique. De telles procédures sont difficiles et fournissent rarement des prévisions réalistes. Par conséquent, les approches phénoménologiques comme ceux fondées sur les bains couplés dépendants de la température sont plutôt privilégiés.

L'objectif de cette thèse est d'étudier les effets magnéto-optiques survenus avant le temps de thermalisation. Dans cette échelle de temps, le régime du système est toujours en phase avec le champ laser et est appelé régime cohérente.

La façon la plus simple de modéliser la réponse magnéto-optique d'un matériau est de considérer l'analogie avec l'atome d'hydrogène. Lorsque dans un système à huit niveaux, son comportement peut être décrit par un hamiltonien composé par un terme non perturbé et un terme qui décrit son interaction avec le champ laser. L'évolution dans le temps de l'électron dans ce système est donné par le formalisme de Liouville, avec l'évolution de la matrice densité. Celle-ci décrit la probabilité de trouver le système dans différents états quantiques. Ses éléments diagonaux représentent la population de chaque niveau et les éléments non diagonaux décrivent les interférences entre deux états et sont appelées cohérences. Les populations relaxent vers l'état fondamental avec le temps T_1, la durée de vie du niveau excité, et les cohérences, avec le temps T_2, beaucoup plus courte que T_1.

En 2009, notre groupe a démontré l'existence de cette composante cohérente présente dans la réponse magnéto-optique obtenue dans une configuration Kerr [4]. Cette configuration permet de mesurer des signaux où les populations et les cohérences dynamiques sont superposées. Il a été montré que cette composante cohérente dépend de la polarisation et est plus importante quand les polarisations de la pompe et de la sonde sont parallèles, que quand elles sont perpendiculaires. De cette façon, à l'aide d'une soustraction, il est possible d'extraire la composante cohérente.

Dans cette thèse, nous montrons qu'il est possible de mesurer directement la dynamique cohérente grâce à une configuration magnéto-optique de mélange à quatre ondes. Le mélange à quatre ondes est un effet d'auto-diffraction du troisième ordre bien connu fondé sur l'interaction de trois champs dans un milieu. Les deux premiers créent un réseau de diffraction qui diffracte le troisième dans des directions différentes, en fonction des ordres de diffraction. Étant $\overrightarrow{k}_p$ la direction de la pompe et $\overrightarrow{k}_s$ la direction de la sonde, nous montrons que les signaux pompe-sonde magnéto-optiques résolus en temps mesurés dans

les direction $2\overrightarrow{k}_p - \overrightarrow{k}_s$ et $2\overrightarrow{k}_s - \overrightarrow{k}_p$ dans la configuration à deux faisceaux ne contiennent pas la contribution des populations comme les signaux Kerr ou Faraday. Le même résultat peut être reproduit dans la configuration à trois faisceaux.

Dans un premier temps, nous avons utilisé des impulsions laser amplifiées de $120fs$ pour prouver la faisabilité de cette technique en mesurant les signaux de mélange à quatre ondes magnéto-optique et le signal Faraday généré dans un échantillon de grenat dopé au bismuth de formule $(GdTmPrBi)_3(FeGa)_5O_{12}$.

Les grenats ferromagnétiques sont élaborés et étudiés depuis les années 1950. Ce matériaux sont intéressants car ils présentent d'importantes propriétés magnéto-optiques. Ayant la formule générale de $(X^{3+})_3(Fe^{3+})_2(Fe^{3+})_3O_{12}$, la structure du grenat est composée de trois sous-réseaux: le site dodécaèdrique, le site octaédriques et le site tétraédrique (chacun des parenthèses de la formule générale représente, dans l'ordre, un sous-réseau). Les ions à l'intérieur des sites octaédriques et tétraédriques sont alignés de manière ferromagnétique, tandis que les deux sous-réseaux sont couplés de manière antiferromagnétique. Le nombre différent de sites tétraédriques et octaédriques se traduit par une non compensation du moment magnétique et par l'aimantation spontanée de la matière.

La structure ferromagnétique du grenat accepte plusieurs substitutions. Celle avec du bismuth est responsable de l'augmentation des effets magnéto-optiques, car elle induit une séparation énergétique des orbitales de fer. Cet effet provoque un transfert de charges entre les orbitales d'oxygène et de fer.

Le grenat ferromagnétique étudié dans cette thèse [5] a été produit par épitaxie de phase liquide [6] par le groupe du Dr. Bernard Barbara à Grenoble. Le film de $7\mu m$ d'épaisseur a été déposé des deux côtés du substrat de GGG [7].

L'étude des signaux magnéto-optiques du mélange à quatre ondes générées dans une configuration à deux faisceaux, dans cet échantillon de grenat et dans la direction $2\overrightarrow{k}_p - \overrightarrow{k}_s$ avec des impulsions de $120fs$, a pu permettre la mesure directe de la composante cohérente de la réponse magnéto-optique. Cependant, la résolution utilisé n'était pas suffisant pour mesurer le temps de cohérence T_2.

Nous montrons également qu'il est possible d'étudier la dynamique des populations et des cohérences par une expérience de mélange à quatre ondes magnéto-optique dans une configuration à trois faisceaux. La dynamique des populations est obtenue en fixant le retard τ entre la première et la deuxième impulsion et en faisant varier le retard T entre les première et troisième impulsion. La dynamique des cohérences est obtenu en fixant T et en variant τ. Ces expériences ont été réalisées avec des impulsions de $47fs$, ce qui limite la résolution temporelle et ne permettent pas non plus d'obtenir T_2, mais ils démontrent l'efficacité de la configuration à trois faisceaux pour étudier la dynamique des populations

et des cohérences.

Pour améliorer la résolution temporelle, nous avons utilisé des impulsions non amplifiées de $10fs$ pour mesurer les signaux de mélange à quatre-ondes magnéto-optique émis dans les directions $2\overrightarrow{k}_p - \overrightarrow{k}_s$ et $2\overrightarrow{k}_s - \overrightarrow{k}_p$. La combinaison de la réponse cohérente avec un temps caractéristique T_2 et la durée d'impulsion crée un décalage temporel entre les signaux obtenus dans ces deux directions. Ce décalage, comme la décroissance exponentielle du signal, donne accès au temps T_2. Nous avons trouvé que ce décalage est de $(1,3 \pm 0,5)fs$ pour la réponse magnéto-optique, qui décrit le comportement de spins et de $(1,7 \pm 0,5)fs$ pour la réponse optique, qui décrit le comportement des charges. Il n'est donc pas possible d'affirmer que ces temps sont égaux ou non en raison de leurs valeurs proches. En utilisant une fonction d'ajustement généré par la convolution d'une impulsion gaussienne et une décroissance exponentielle avec le temps T_2, il est possible d'obtenir $2fs \leq T_2 \leq 3,5fs$.

En étant donné l'extrême importance de la phase temporelle lorsqu'il s'agit des impulsions laser sous-$10fs$, nous avons mené des simulations du signal de mélange à quatre ondes fondées sur un système à deux niveaux et sur un élargissement homogène généré par des impulsions de phases différentes. Nous montrons que le centre du signal dépend de la durée de l'impulsion utilisée et que pour le même temps de cohérence, les impulsions avec différentes phases génèrent différents décalages temporels entre les signaux émis dans les directions $2\overrightarrow{k}_p - \overrightarrow{k}_s$ et $2\overrightarrow{k}_s - \overrightarrow{k}_p$. Cela montre qu'il est important d'avoir la caractérisation de la phase et de l'amplitude de l'impulsion utilisée pour mesurer ces signaux. La trace d'auto-corrélation de l'intensité obtenue à partir des impulsions expérimentales est très semblable à la trace simulée qui ne prend en compte aucune phase spectrale, ce qui permet de dire que, dans notre cas, la phase de l'impulsion expérimentale est minime et ne joue pas un rôle important dans la détermination du centre du signal.

En conclusion, on montre qu'il est possible de mesurer la dynamique d'aimantation cohérente d'un échantillon de grenat dopé au bismuth dans une configuration de mélange à quatre ondes magnéto-optique avec une résolution temporelle suffisante estimer le temps de cohérence.

Acknowledgement

I would like to thank M. Niels Keller, M. Fabrice Vallée, M. Pierre Gilliot and M. Bernard Barbara for accepting to judge this work.

I would like to infinitely thank Jean-Yves Bigot for receiving me in his group for the development of this thesis. I have always been amazed by your work and the way you do it and it was a great experience for me to be able to work with you for these three years. I thank you for all and every little and major thing you have done for me. I will never forget it.

I thank Marie Barthelemy for the discussions, for helping me, for calming me down, for cheering me up and for being a fundamental piece in this work. I would have not arrived here without you. You've been through the amazing troubles ultrashort pulses brought me with me and had always a funny and smart way to deal with them. Thank you for your time and attention.

Thank you, Valérie Halté, for the always funny corridor and lunch talks and for the precious advices of lab work, nothing counts as much as the experience. Thanks for my 'weekend à la campagne' and for making me feel at home. You've always been thoughtful and kind to me. I hope she gets that from you!

Thank you, Michèle Albrecht, for the many hours spent in the lab helping me. Thank you for the support and for sharing your infinite knowledge of life and electronics.

Thank you, Nabila Kadiri, for the coffee talks, for the company, for the incentive and for sharing your experience. Thanks for always being there.

Thank you, Mircea Vomir, for all the silly questions you have answered and for all the experimental tricks you have taught me. They were of extreme value, don't forget to teach them to Stephanie.

Thank you, Ahmed Maghraoui, for the laughs, for the French and Arabic lessons, for the help when I needed an extra arm, for listening and for sharing the life in the lab with me. Thank you for helping me when I was not sure about what I was doing and thank you for sharing your calm. Take care of your beautiful family!

Thank you, Amani Zagdoud, for sharing your PhD experiences and helping me in so many ways. Thank you, Jiwan Kim, for the Coke cans, postcards and for the infinite laughs. Thank you, Erwan Terrier, for the talks, laughs and for always being so kind to me, even when I was not! Good luck for all of you, you have amazing careers in front of you. Thank you, Hélène Vonesch, Hasan Kesserwan, Sacha Kovalenko, Vishal Shokeen and Marwan Deb that even for a short time showed me how lucky I was to be in Femtomag.

Thanks to this group that taught me so much. Thanks for sharing your special moments with me and for letting me share mine with you.

Thank you, Leandro Hostalácio Freire de Andrade, for allowing me to enter in an Optics lab for the first time. You were there in the beginning and I wouldn't be here if it wasn't for you. Thank you for the teaching and for the trust.

Thank you, Sacha Maillot, for sharing the office, the laughs, the smell and all the PhD inscription information I never knew, every year!

Thanks to Estelle Brunette, who I disturbed so many times in these three years and who always promptly helped me.

Thanks to all the students with who I had the pleasure of sharing experiences, laughs and worries. Thank you Silvia Zanettini, Ferdaous Ben Romdhane, Manuel Gruber, Maxime Liard, Débora Persuy...

I would also like to thank everybody I worked with, directly or indirectly during this thesis and that, somehow, helped me getting here: Dominique Quince, Xavier Ledoux, Sophie Siegel, Isabelle Colrat, Nicolas Beyer, Gauthier Dekyndt, Gilles Versini, Olivier Crégut, Nicolas Bergeard, Beatrice Masson and many more...

Thank you, Felipe, for countless conversations about everything and nothing and for being my company and sharing topics when I needed. You know that for many times you were the only one.

Thank you, Náthali, for adopting me and for always being there with your wise advices.

Thank you, Karina, for helping me accept the PhD joys and tragedies and for making me realize that no, I'm not alone and that yes, it happens to all PhD students, everywhere!

I thank my Brazilian friends for not forgeting me, simple as that. For making me remember, even if not very often, what I had built and what expects me at home. Thank you Thais, Vivian, Patricia, Alessandro, Gustavo, Fabiana, Felipe... And God, thank you for whoever invented Whatsapp!

I thank all my family, specially my grandparents that never let me forget where I came from.

Thank you, Lucia and José Carlos, my heart aunt and uncle, who always made me

feel important and thank you, Victor and Carla, for making me forget the thousands of kilometers between us.

I thank my parents, Richard and Sueli, that always encouraged me in this great adventure and that, even being far, never stopped trusting me. This is all for you, for all education and love you invested on me.

Thank you, Carol, my super sister, for always cheering me up when I though I couldn't make it and for sharing with me all aspects of this great experiment I have performed in my life. You never, ever, stopped believing in me, even when I did. Be sure I will never, ever, stop believing in you.

Agradecimentos

Eu gostaria de agradecer os senhores Niels Keller, Fabrice Vallée, Pierre Gilliot e Bernard Barbara por terem aceitado julgar este trabalho.

Eu gostaria de agradecer infinitamente Jean-Yves Bigot por me receber em seu grupo para o desenvolvimento dessa tese. Eu sempre fui fascinada pelo seu trabalho e pela maneira como você o faz e foi uma grande experiência pra mim poder trabalhar com você durante esses três anos. Eu te agradeço por cada uma e todas as pequenas e grandes coisas que você fez por mim. Eu nunca esquecerei.

Eu agradeço Marie Barthelemy pelas discussões, por me ajudar, por me acalmar, por me animar e por ser uma peça fundamental nesse trabalho. Eu não teria chegado até aqui sem você. Você passou comigo pelos fantásticos problemas que os pulsos ultra-curtos me trouxeram e sempre teve um jeito engraçado e inteligente de lidar com eles. Obrigada pelo seu tempo e atenção.

Obrigada, Valérie Halté, pelas sempre divertidas conversas de corredor e durante o almoço e pelos preciosos conselhos no laboratório, nada conta mais que a experiência. Obrigada pelo meu "weekend à la campagne" e por me fazer me sentir em casa. Você sempre foi atenciosa e gentil comigo. Espero que ela herde isso de você!

Obrigada, Michèle Albrecht, pelas várias horas passadas no laboratório me ajudando. Obrigada pelo apoio e por compartilhar comigo sua infinita sabedoria de vida e de eletrônica.

Obrigada, Nabila Kadiri, pelas conversas no café, pela companhia, pela ajuda pelo incentivo e por compartilhar sua experiência. Obrigada por estar sempre lá.

Obrigada, Mircea Vomir, por todas as perguntas bobas que você respondeu e por todos os truques experimentais que você me ensinou. Eles foram extremamente valiosos, não esqueça de ensiná-los a Stephanie.

Obrigada, Ahmed Maghraoui, pelas risadas, pelas lições de francês e de árabe, pela ajuda quando eu precisava de uma mão no laboratório, por me ouvir e por compartilhar a vida no laboratório comigo. Obrigada por me ajudar quando eu não estava certa sobre o que eu estava fazendo e obrigada por compartilhar a sua calma. Cuide bem da sua linda

família!

Obrigada, Amani Zagdoud, por compartilhar sua experiência de doutorado comigo e por me ajudar de várias maneiras. Obrigada, Jiwan Kim, pelas latas de Coca-Cola, pelos cartões postais e pelas inúmeras risadas. Obrigada, Erwan Terrier, pelas conversas, risadas e por sempre ser tão gentil comigo, mesmo quando eu não era! Boa sorte a todos vocês, vocês tem carreiras brilhantes pela frente. Obrigada, Hélène Vonesch, Hassan Kesserwan, Sacha Kovalenko, Vishal Shokeen e Marwan Deb que mesmo por um curto espaço de tempo me mostraram como eu tive sorte de estar na equipe Femtomag.

Obrigada a essa equipe que me ensinou tanto. Obrigada por compartilhar momentos especiais comigo e por me permitir compartilhar os meus.

Obrigada, Leandro Hostalácio Freire de Andrade, por ter permitido que eu entrasse em um laboratório de óptica pela primeira vez. Você estava lá quando eu comecei e eu não estaria aqui se não fosse por você. Obrigada pelos ensinamentos e pela confiança.

Obrigada, Sacha Maillot, por compartilhar a sala, as risadas, o cheiro e toda a informação da reinscrição no doutorado que eu nunca sabia, todo ano!

Obrigada, Estelle Brunette, quem eu perturbei tantas vezes nesses três anos e quem sempre me ajudou prontamente.

Obrigada a todos os estudantes com quem eu tive o prazer de compartilhar experiências, risadas e preocupações. Obrigada Silvia Zanettini, Ferdaous Ben Romdhane, Manuel Gruber, Maxime Liard, Débora Persuy...

Eu também gostaria de agradecer todos com quem eu trabalhei direta ou indiretamente durante o doutorado e que, de alguma maneira, me ajudaram a chegar aqui: Dominique Quince, Xavier Ledoux, Sophie Siegel, Isabelle Colrat, Nicolas Beyer, Gauthier Dekyndt, Gilles Versini, Olivier Crégut, Nicolas Bergeard, Beatrice Masson e vários outros...

Obrigada, Felipe, pelas inúmeras conversas sobre tudo e nada e por ser minha companhia e sempre compartilhar tópicos quando eu precisava. Você sabe bem que por muitas vezes foi o único.

Obrigada, Náthali, por ter me adotado e por estar sempre por perto com seus sábios conselhos.

Obrigada, Karina, por me ajudar a aceitar as alegrias e tragédias do doutorado e por me fazer perceber que não, eu não estou sozinha e que sim, acontece com todo os doutorandos, em todos os países!

Eu agradeço meus amigos brasileiros por não terem me esquecido, simples assim. Por me fazerem lembrar, mesmo que não muito frequentemente, o que eu construi e o que me espera em casa. Obrigada Thais, Vivian, Patricia, Alessandro, Gustavo, Fabiana, Felipe...

E Deus, obrigada por quem quer que seja que inventou o Whatsapp!

Eu agradeço toda a minha família, especialmente meus avós que nunca me deixaram esquecer de onde eu venho.

Obrigada, Lucia e José Carlos, minha tia e meu tio de coração, que sempre me fizeram sentir importante e obrigada, Victor e Carla, por me fazerem esquecer dos milhares de kilômetros entre nós.

Eu agradeço meus pais, Richard e Sueli, que sempre me encorajaram nessa grande aventura e que, mesmo estando longe, nunca deixaram de confiar em mim. Isso tudo é pra vocês, por toda educação e amor que vocês investiram em mim.

Obrigada, Carol, minha super irmã, por sempre me animar quando eu não me sentia capaz e por compartilhar comigo todos os aspectos dessa maravilhosa experiência que eu fiz na minha vida. Você nunca, nunca, deixou de acreditar em mim, mesmo quando eu deixei. Tenha certeza que eu nunca, nunca, vou deixar de acreditar em você.

Contents

Introduction and motivation

Magnetic storage is the most used method of data storage in commercial hard-drives devices. In 1999, this industry represented already one third of the semiconductors industry, being the research in magnetism and magnetic materials attractive for the 50 billion dollars/year market the magnetic recording industry generates [8]. In these devices, the magnetic head moves very close to the magnetic surface where the data is recorded in order to change the magnetization of sub-micrometer regions using magnetic field pulses. This magnetization reversal is obtained in a few nanoseconds, what gives a frequency of writing of less than $1GHz$.

In order to improve the speed of writing and reading, it is important to investigate the interaction of laser pulses, instead of pulsed magnetic fields, with matter. Moreover, advances in magnetic imaging are also a great motivation for the study of the interaction of light with matter, considering the many medical and material applications.

Ultrafast magneto-optics is a research field that has been propelled tending to the THz frequencies of data writing as well as offering a way of exploring fundamental mechanisms involved in the magnetic processes and better understanding the phenomena governing the dynamics of the magnetization.

The interaction of ultrashort laser pulses with matter has been investigated with this motivation since the 1990s. In 1996, our group has shown that $60fs$ laser pulses can demagnetize ferromagnetic materials like nickel [1]. Since then, the study of the mechanisms of relaxation of the magnetization in different magnetic materials has been widely explored using experimental methods like the time-resolved magneto-optical Kerr effect in pump and probe experiments. It consists in using two identical laser pulses separated in time by a controlled delay to investigate ultrafast phenomena.

The interaction between laser fields and magnetic materials can be studied in different time scales [9]. On the micro and millisecond range, the important phenomenon is the motion of the magnetic domain walls. At the nanosecond scale, the magnetization of each domain is reversed to be parallel to the external applied field, it happens when the energy brought by the field is bigger than the anisotropy barrier. When the energy absorbed

by the ferromagnetic material is dissipated to the lattice, via the spin-phonon scattering, the magnetization starts precessing around the effective magnetic field with a frequency that varies from a fraction of a GHz for soft materials like permalloy to $\sim 100GHz$ in highly anisotropic materials like $CoPt$ or $FePt$. This motion of precession is damped in the $50ps$ to $5ns$ temporal range, depending on the material. In the femtosecond scale, the dominant mechanisms responsible for a change of the magnetization are the spin-orbit interaction, responsible for connecting the electrons orbital motion to their internal spin degree of freedom, and the exchange interaction. A scheme of these different time scales and different mechanisms is shown in figure 1.

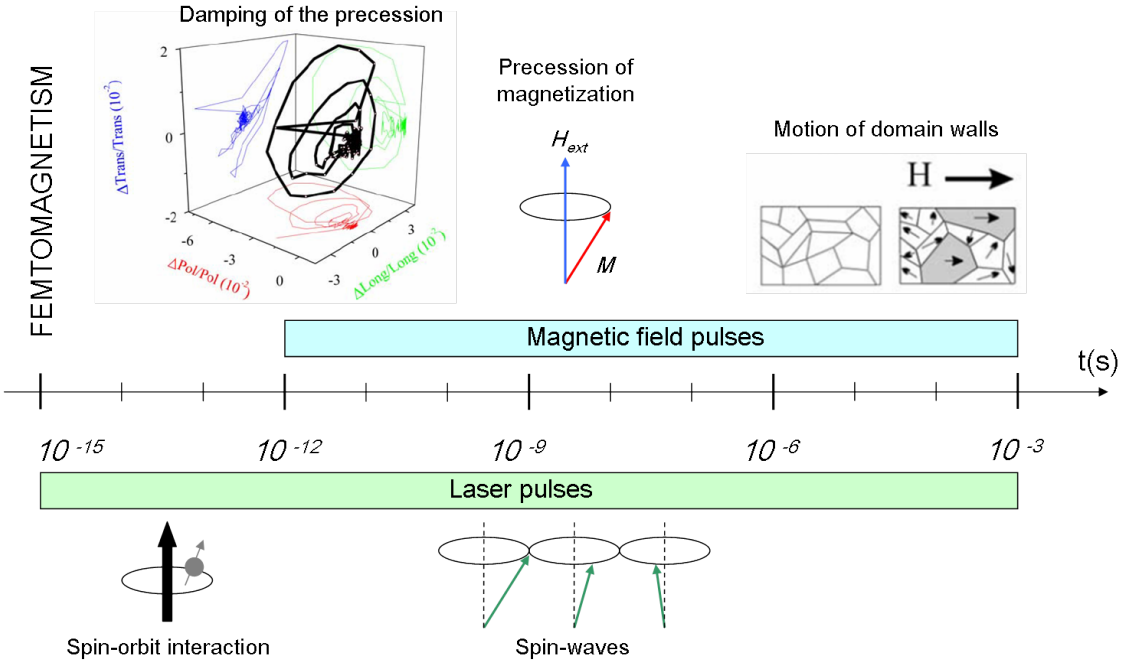

Figure 1: Temporal scale of different magnetic phenomena. Figures from references [10] and [11].

When one considers a temperature approach for the electron dynamics of a metallic film, different scales and mechanisms are also considered for the dynamics of the charges (electrons and holes). First, in a time shorter than $20fs$, the electrons are excited by the laser field. They acquire a large kinetic energy above the Fermi level and are found in a regime that can not be described by a temperature. The electrons interact with each other via the Coulomb interaction, during the thermalization time that lasts some hundreds of femtoseconds. They thermalize to a hot Fermi-Dirac distribution, as shown in figure 2, respecting the Pauli exclusion principle. Simultaneously, the dissipation of the energy

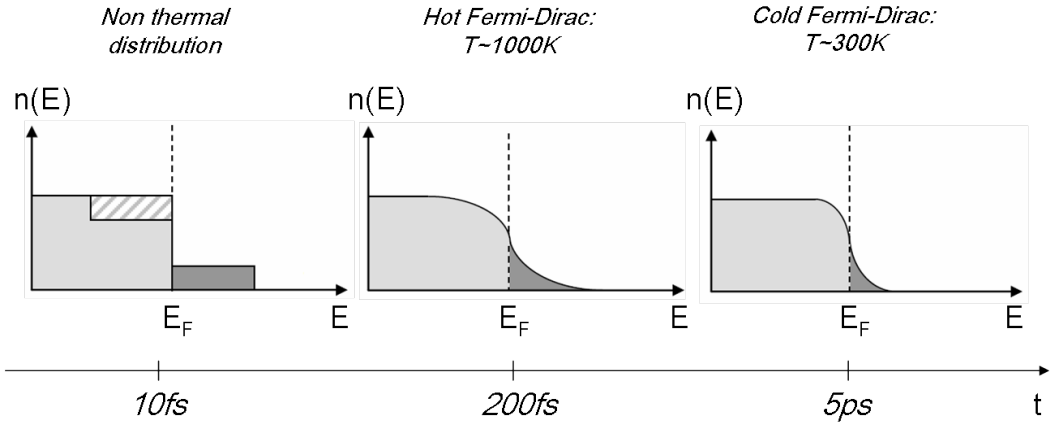

Figure 2: Scheme of electron dynamics in a metal after ultrashort optical excitation. $n(E) = \left[1 + exp\left(\frac{E-E_F}{k_B T}\right)\right]^{-1}$ is the Fermi-Dirac distribution (E_F is the Fermi level energy, k_B is the Boltzman constant and T is the temperature).

stored in the system to the lattice takes place in the picosecond scale.

The electron kinetics in metals can then be studied using different techniques such as the two-photon emission and a variety of femtosecond optical methods [12]. Most of them are based on the pump and probe technique [13] [14] [15].

Origins of the ferromagnetism and magnetization

The ferromagnetism describes the capacity of certain materials of having a magnetization different from zero even when no magnetic field is applied. Iron, nickel and cobalt are ferromagnetic, as well as some rare earth elements under the Curie temperature. It is well known that the magnetization in a ferromagnetic material decreases when the material is heated. When the Curie temperature is reached, the magnetic order is lost and no magnetization is left.

The first phenomenological description of the magnetization was proposed by Pierre Weiss in 1907 [16]. He proposed the existence of a molecular field, that can be considered as a microscopic mean field, originated from the other magnetic moments of the material, that interact with each magnetic moment of the material. Taking into account that this field is proportional to the magnetization, he proposed a model to explain the Curie temperature and the paramagnetism. The Weiss theory gives information about the magnitude of the magnetization, but nothing can be said about its direction.

The phenomenological approach of molecular field was theoretically justified when Werner Heisenberg introduced the exchange interaction on the basis of quantum theory

in 1928 [17]. He proposed that this interaction is the origin of the molecular field. The exchange interaction reflects the electrostatic Coulomb repulsion of electrons on neighbouring atoms (associated to the Pauli exclusion principle). The exchange energy in a system of spins is then described by the sum of the interactions of all and every spin with each other. It is strongest for adjacent moments and in ferromagnetic materials it favors a parallel alignment of the spins.

Another model to understand the ferromagnetic behaviour of materials was proposed by Edmund C. Stoner in 1938 [18]. This model takes into account the band structure of the ferromagnet and assumes magnetic moment arises from mobile d-band electrons. As it relies on the different occupation of the spins when the temperature increases, without considering a reduced exchange splitting, it predicts too high Curie temperatures.

These models do not describe the variation of the magnetization direction nor, for example, the existence of an easy axis in a crystalline sample. For that, one must consider the Stoner-Wohlfahrt model [19] and calculate the minimum of free energy of the system (composed by the exchange, shape anisotropy, magneto-crystalline anisotropy, Zeeman and demagnetization energies), given by

$$E_{total} = E_{exchange} + E_{anisotropy} + E_{Zeeman} + E_{demagnetization}. \quad (1)$$

The magnetic anisotropy of the system may arise from the shape of the sample, from magneto-crystalline effects and from the interaction with an external field. The shape anisotropy of the sample influences the preferential direction of the magnetization due to long distance magnetic dipolar interactions. For a thin film, for example, the shape anisotropy places the easy axis of magnetization in the plane of the sample.

The magneto-crystalline anisotropy has its origin in the spin-orbit interaction and explains why an easy axis of magnetization alignment is observed independently of the sample shape. It corresponds to a preferential orientation of the magnetic moments in the material following symmetry rules. The free energy of the magneto-crystalline anisotropy is the work to change the magnetization direction.

The Zeeman interaction describes the interaction between the magnetization and the external field applied to the sample. This interaction tends to align the magnetic moments parallel or anti-parallel to the external field.

The interaction of a laser pulse with a material submitted to a static magnetic field adds energy to the system and different energy contributions must be considered. It is then necessary to consider all the energy contributions and the possible changes induced by the laser field perturbation on them.

Magnetization dynamics studies - history

The first important studies using the pump and probe technique were based on an all-optical configuration and aimed studying the relaxation processes in metallic materials after the laser excitation. The first one was performed in 1983 in Cu [20] and a fast increase and decrease of the reflectivity was observed after the femtosecond and picosecond laser excitation, being attributed to the initial heating of electrons above the lattice temperature. It showed the ability of temporally measuring the contribution of the electron and lattice to the heating of the metal. These results have been confirmed with better time resolution [21] [22] [23].

Since then, different femtosecond techniques have been developed to study the relaxation processes in metals like the photoemission, that allows studying the thermalization of electron [24] [25] [26] and time-resolved pump and probe experiments measuring the second harmonic generation efficiency [27] or the transient reflectivity [28].

In parallel, the same techniques had been used to investigate the magnetization dynamics in magnetic materials. The first ultrafast time-resolved studies of the effects of a laser pulse in the magnetization of a material have been performed in simple materials like Fe, Ni and Gd samples. In 1984, any magnetic effects were observed up to the melting point of Ni and Fe samples excited by pulses of $5 - 20ps$ duration [29]. Later, in 1991, studies using $10ns$ pulses to heat the sample and $30ps$ pulses to probe it estimated the spin-lattice relaxation time in Gd films to be $100 \pm 80ps$ using the time-resolved photo-emission technique [30]. This relaxation time was later confirmed by the theoretical predictions [31]. The problem so far was the pulse duration, which was longer than the time scales of interest.

In 1996, using a $60fs$ laser pulses and performing magneto-optical Kerr effect experiments, our group demonstrated the ultrafast loss of magnetic order of a ferromagnetic Ni film [1]. It was found that the magnetization of the film reaches a minimum value in the sub-picosecond time scale after laser excitation. The proposal to understand such effects was to extend the electrons thermalization model (called two-temperature model) to spin effects. These models will be more explored in sections 1.2.1 and 1.2.2.1. They allowed the authors to find electrons and spins temperatures dynamics that differ in the first few picoseconds.

This pioneer study has motivated several research efforts to understand the fundamental mechanisms at the origin of the demagnetization. The results presented were confirmed by several studies of the spin dynamics that used the magneto-optical Kerr spectroscopy [32], the second harmonic generation technique [33] [34], the two-photon photoemission experiment [35], etc. Moreover, a complete demagnetization of a ferromagnetic film of

$CoPt_3$ was shown by our group in 1998 [36]. It was shown that, at high laser intensities, the hysteresis disappears in such films and that a paramagnetic state is achieved in ultrashort time scales. Similar results have been reproduced in Ni films confirming that the demagnetization and the electrons thermalization happen simultaneously [34] [37].

At the same time, magnetization reversal studies were led in particles and tried to prove the consistency of the Néel-Brown model [38] [39] that treats the magnetization reversal as a phenomenon thermally activated. It states that at any finite temperature, thermal fluctuations cause the spins to undergo a brownian-like motion around the easy axis, with a finite probability that the moment will flip from one easy direction to another. The first experimental evidence of magnetization reversal in a single ferromagnetic nanoparticle following this model was reported in 1997 [40].

A difference between the time-resolved Kerr ellipticity and rotation and their temperature and magnetic field dependence was observed in $Cu/Ni/Cu$ wedges [41]. The rotation and ellipticity have been shown to be different and an estimation of the spin relaxation was made between $0,5$ and $1ps$.

A more complete and detailed study of the Kerr rotation and ellipticity analysing the real and imaginary parts of the dielectric tensor has been performed by our group in 2002 [42]. Using $20fs$ pulses, the authors studied the spins and charges thermalization at high repetition rates. It was shown that, after the thermalization of the electrons, the real and imaginary parts of the Voigt vector are identical. In addition, their relative variation was found to be ten times larger than that of the diagonal elements of the tensor, what shows that the spins dominate the magneto-optical response. However, during the electrons thermalization, the two components of the Voigt vector follow different dynamics, what put in question the formalism used to describe the nonthermalized spin dynamics and implies new formalisms for the laser induced demagnetization. For example, it was shown that in $CoPd$ samples, an ultrafast change in the spin-orbit coupling leads the quenching of the perpendicular magnetic anisotropy of the samples, what results in a demagnetization [43]. However, only the incoherent contribution of this process was observed due to the temporal resolution and experimental configuration.

Precession

In adition to the ultrafast demagnetization, the laser pulse may also induce a precession of the magnetization around an effective field, that considers the anisotropy and the external field, to be more explored in section 1.2.2.2.

The first studies in the area showed the possibility of optically generating magnetic precession on a time scale of $10ps$ in a ferromagnetic $CoPt_3$ alloy film [44] and in a

$NiFe/NiO$ film [45]. This variations include a large contribution from the lattice heating. A microscopic non quantitative model that allows to derive the proper time scales from quantum-mechanical principles was proposed in 2005 [46].

In 2005, our group has studied the three-dimensional trajectory in space of the precession [47]. It was observed that the initial change of the modulus and of the orientation of the magnetization occurs in a few hundreds of femtoseconds and that it is followed by its precession and damping around the effective field. The polarimetric analysis used in the experiments has been presented as a well suited method to study the change of the anisotropy associated to the dynamical heating of the lattice.

In these last years, the study of the precession has created an important variety of methods to investigate the mechanisms involved in the ultrafast magneto-optical response of materials. It has been used combined with acoustic pulses to investigate the magnetization dynamics of ferromagnetic Ni films [48], combined with rare earth doping, to study the influence of the doping concentration in Co films [49], etc.

The possibility of starting a precession motion with phase that depends on the right or left circular polarization of light has prooved its existence [50]. This dependence is attributed to a coherent interaction between photons and spins. The inverse Faraday effect is used to explain the purely optical and nonthermal excitation in a $DyFeO_3$ ferromagnet.

In the literature, the nonthermal effects are usually distinguished in photomagnetic effects, that are a result of an effective excitation of the system after the absorption of a photon, and in optomagnetic effects, that are not related to the absorption but to the inverse magneto-optical Faraday effect [51].

The photoinduced anisotropy is claimed to be at the origin of the photomagnetic effects in garnets [52]. The Pb^{+2} impurities replace the rare-earth ions in the dodecahedral site and act like an electron receptor. It creates holes in the Fe ions in the tetrahedral sublattice. To keep the neutrality, some ions Fe^{3+} become Fe^{4+}. The photoexcitation induces a charge transfer between the ions Fe^{3+} and Fe^{4+} what moves the Fe^{4+} ions to sites with different symmetry, changing the magnetic anisotropy. The optical switching has been proved to be due to absorption only and to be wavelength and polarization independent [53].

The optomagnetic effects are explained with the phenomenological approach of the creation of a strong magnetic field during the laser pulse due to the inverse Faraday effect (when the polarization of light induces changes in the magnetization of the material [52]). The microscopic approach of the effect can be seen as the action of two different frequency components of the laser pulse. The first one stimulates an optical transition to a virtual state with high spin-orbit coupling (with large probability of spin-flip, then) and the second

one stimulates the relaxation to the fundamental state with spin-flip.

However, a new approach has been used to explain both phenomena. Studies in $GdFeCo$, known for the antiferromagnetic coupling between Gd and Fe magnetic moments while in fundamental state, show a transient ferromagnetic-like state leading to the switching of the magnetization driven by ultrafast heating [54]. This state is due to the different demagnetization rate of the rare-earth and the Fe sublattices and to the angular momentum transfer between them. This explanation does not consider a macrospin approach nor a micromagnetic one. It requires the use of atomistic-level spin calculations.

Coherent response

In 2009, our group has shown the existence of a coherent component in the magneto-optical response, associated to the magnetization dynamics, and that this component is polarization dependent [4]. It is important to emphasize here that the great challenge of the measurement of the coherent component is being able to isolate it from the population dynamics (thermalization dynamics of the spins) present in the Faraday signal. The lifetime of the spins populations is given by the time T_1 and the dephasing dynamics of the coherent response is characterized by the time T_2.

In this study, it was shown that if the polarization of the pump and probe beams are parallel, one sees the coherent component, what is very much reduced when the polarizations are perpendicular, as shown in the curves from figure 3. This way, it is possible to extract the coherent component from a Kerr rotation signal by subtracting one from the other.

This method proves the existence of the coherent magneto-optical component associated to the spin states as the magnetic signals are obtained after a difference under opposite polarity of the static magnetic field. However, this method suffers from the fact that it does not allow measuring only the coherent contribution. For that, in this thesis we have used the magneto-optical four-wave mixing, a procedure similar to the well known self-diffraction effect [55].

Objectives

The present thesis aims at studying the coherent dynamics of charges and spins that happens before the thermalization time. We will show that the magneto-optical four-wave mixing configurations allow to measure directly the coherent dynamics in a garnet film, a process that we attribute to the spin-orbit interaction. The challenge faced is the very short time scale during which these coherent magneto-optical processes occur. It required

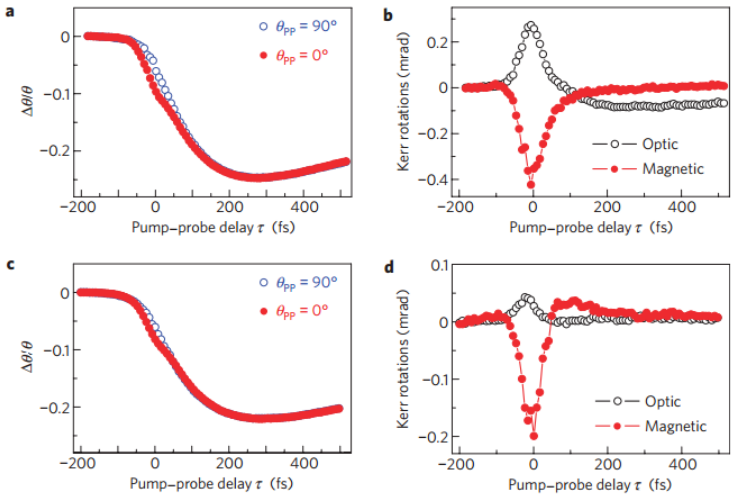

Figure 3: Differential Kerr rotation for a Ni film (a) and for a $CoPt_3$ film (c) for pump and probe polarizations parallel or perpendicular. Electronic and magnetic coherent contributions to the dynamics of the probe polarization for a Ni film (b) and for a $CoPt_3$ film (d). Figure from reference [4].

a specific set-up with ultrashort optical pulses.

The coherence time T_2 can have optical or magneto-optical origin. In this thesis, we aim to measure the electronic coherence time and the electromagnetic coherence time using the four-wave mixing and the magneto-optical four-wave mixing configurations.

Manuscript organization

This thesis is organized as follows:

- Chapter 1: the optical and magneto-optical effects that will allow understanding the experimental results are presented. We will describe the linear and nonlinear magneto-optical response of magnetic films and discuss the various relaxation processes involving the charges and spins dynamics. We discuss the influence of the spectral phase on the four-wave mixing signal, point of interest in this thesis.

- Chapter 2: we describe a theoretical approach that allows understanding coherent magneto-optical effects in magnetic systems represented by discrete spins states. We present the hamiltonian of the spin-orbit interaction as well as a hydrogen-like model, approximated by eight states, which is consistent for describing ultrafast magneto-optical effects and, correspondingly, the dynamics of the coherences and populations of these states.

- Chapter 3: in the first part, we describe the sample studied. We review some important properties of garnets, starting from the garnets found in nature and then we describe the properties brought by different components to the synthetic ones. In the second part, the experimental techniques used in this thesis are presented, from the description of the femtosecond pulse generation and the different systems that we have used to the data analysis procedures.

- Chapter 4: the results that we obtained with different laser systems are presented. We then discuss the corresponding time evolution of the spins and the charges, both from the point of view of their coherences and populations dynamics.

Introduction et motivation

Le stockage magnétique est la méthode de sauvegarde de données la plus utilisée dans les disques durs commerciaux. En 1999, cette industrie représentait déjà un tiers de l'industrie des semi-conducteurs, étant la recherche dans le magnétisme et les matériaux magnétiques attractif pour le marché de 50 milliards de dollars par an que l'industrie d'enregistrement magnétique génère [8].Dans ces dispositifs, la tête magnétique se déplace très près de la surface magnétique où les données sont enregistrées, dans le but de modifier l'aimantation de régions sous-micrométriques en utilisant des impulsions magnétiques. Ce renversement de l'aimantation est obtenu en quelques nanosecondes, ce qui donne une fréquence d'écriture de moins de $1GHz$.

Afin d'améliorer la vitesse d'écriture et de lecture, il est important d'étudier l'interaction des impulsions laser, au lieu de champs magnétiques pulsés, avec la matière. En outre, les progrès de l'imagerie magnétique sont également une grande motivation pour l'étude de l'interaction de la lumière avec la matière, compte tenu des nombreuses applications médicales et matérielles.

La magnéto-optique ultra-rapide est un domaine de recherche qui a permit d'atteindre des fréquences d'écriture de données de l'ordre du THz tout en offrant une façon d'explorer les mécanismes fondamentaux impliqués dans les processus magnétiques et de mieux comprendre les phénomènes qui régissent la dynamique de l'aimantation.

L'interaction des impulsions laser ultracourtes avec la matière a été étudiée depuis les années 1990. En 1996, notre groupe a montré que des impulsions laser de $60fs$ peuvent démagnétiser des matériaux ferromagnétiques comme le nickel [1]. Depuis lors, l'étude des mécanismes de relaxation de l'aimantation dans les différents matériaux magnétiques a été largement explorée en utilisant des procédés expérimentaux comme l'effet Kerr magnéto-optique résolue en temps dans des expériences pompe-sonde. Il consiste à utiliser deux impulsions laser identiques séparés temporellement par un retard contrôlé pour étudier des phénomènes ultra-rapides.

L'interaction entre le champ laser et les matériaux magnétiques peut être étudié à différentes échelles de temps [9]. A l'échelle de la micro et de la milliseconde, le phénomène

important est le mouvement des parois de domaines magnétiques. A l'échelle de la nanoseconde, l'aimantation de chaque domaine est inversée pour être parallèle au champ appliqué externe, ce qui se produit quand l'énergie apportée par le champ est plus grande que la barrière d'anisotropie. Lorsque l'énergie absorbée par le matériau ferromagnétique est dissipée vers le réseau, via diffusion spin-phonon, l'aimantation commence sa précession autour du champ magnétique effectif avec une fréquence qui varie d'une fraction de GHz pour des matériaux tendres comme le permalloy à $\sim 100GHz$ pour des matériaux très anisotropes comme $CoPt$ ou $FePt$. Ce mouvement de précession est amorti dans le plage temporelle allant de $50ps$ à $5ns$, en fonction du matériau. A l'échelle femtoseconde, les mécanismes dominants responsables du changement de l'aimantation sont l'interaction spin-orbite, qui lie le mouvement orbital des électrons à leur degré de liberté de spin interne, et l'interaction d'échange. Un schéma avec ces différentes échelles de temps et des différents mécanismes est illustré dans la figure 4.

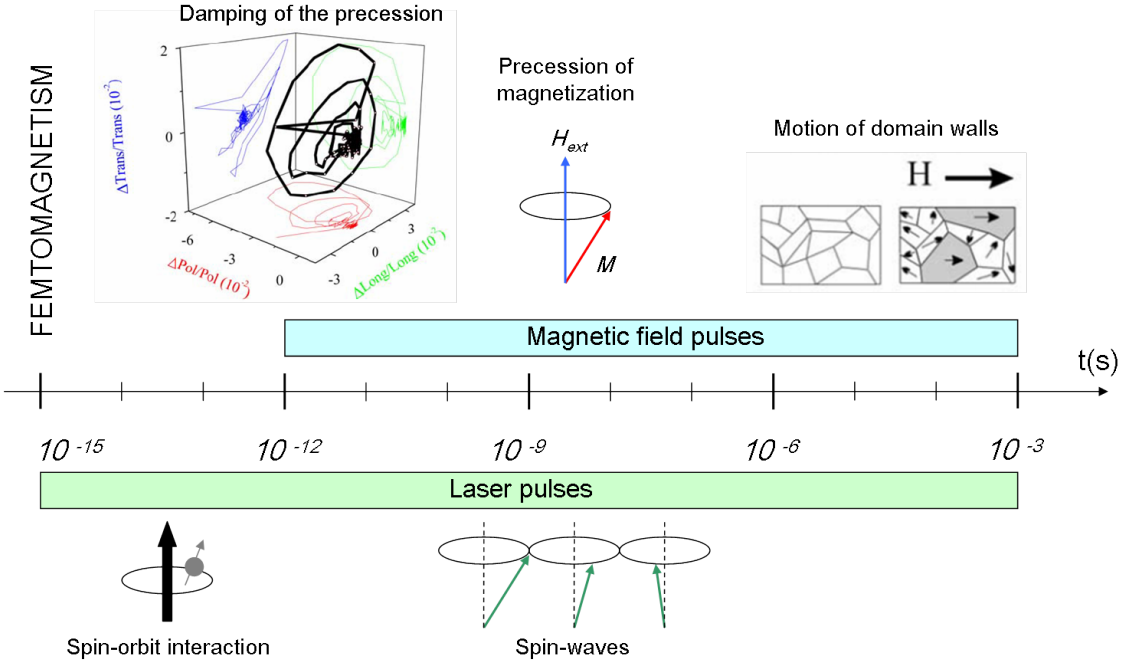

Figure 4: Echelle temporelle des différents phénomènes magnétiques. Figures de références [10] et [11].

Si l'on considère d'un point de vue thermique la dynamique des électrons d'un film métallique, différentes échelles et des mécanismes sont également considérés pour la dynamique des charges (électrons et trous). Tout d'abord, dans un temps plus court que $20fs$, les électrons sont excités par le champ laser. Ils acquièrent une grande énergie

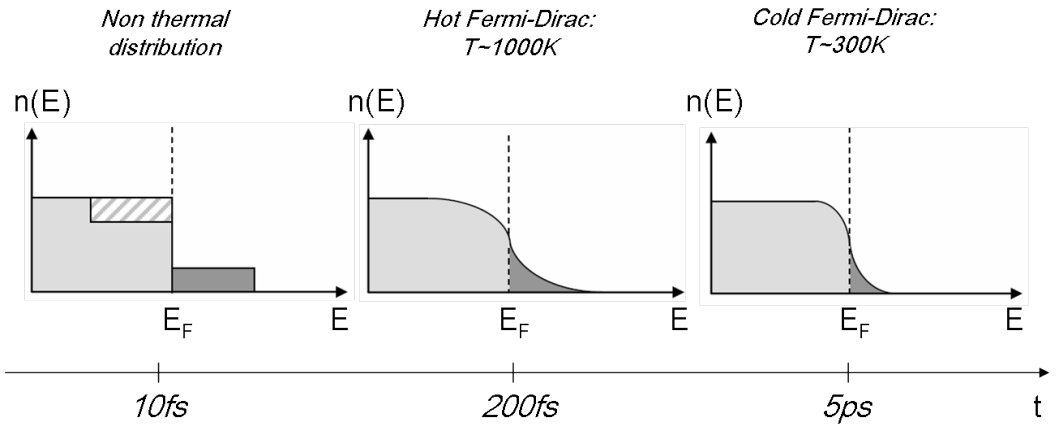

Figure 5: Schéma de la dynamique des électrons dans un métal après excitation optique ultracourte. $n(E) = \left[1 + exp\left(\frac{E-E_F}{k_B T}\right)\right]^{-1}$ est la distribution de Fermi-Dirac (E_F est l'énergie du niveau de Fermi, k_B est la constante de Boltzman et T est la temperature).

cinétique au-dessus du niveau de Fermi et se trouvent dans un régime qui ne peut pas être décrit thermiquement. Les électrons interagissent les uns avec les autres par l'interaction de Coulomb, pendant le temps de thermalisation qui dure quelques centaines de femtosecondes. Ils thermalisent pour atteindre une distribution de Fermi-Dirac chaude, comme le montre la figure 5, en respectant le principe d'exclusion de Pauli. En même temps, la dissipation de l'énergie stockée dans le système vers le réseau a lieu à l'échelle de la picoseconde.

La cinétique des électrons dans les métaux peut alors être étudiée en utilisant différentes techniques telles que l'émission de deux photons et une variété de méthodes optiques femtosecondes [12]. La plupart d'entre eux sont fondées sur la technique de pompe-sonde [13] [14] [15].

Origines du ferromagnétisme et de l'aimantation

Le ferromagnétisme décrit la capacité de certains matériaux d'avoir une aimantation différent de zéro, même en l'absence de champ magnétique externe. Fer, nickel et cobalt sont ferromagnétiques, ainsi que des éléments des terres rares au dessous de la température de Curie. Il est bien connu que l'aimantation dans un matériau ferromagnétique diminue lorsque le matériau est chauffé. Lorsque la température de Curie est atteint, l'ordre magnétique est perdu et aucune magnétisation reste.

La première description phénoménologique de l'aimantation a été proposé par Pierre Weiss en 1907 [16] . Il a proposé l'existence d'un champ moléculaire, qui peut être considéré

comme un champ moyen microscopique, issue d'autres moments magnétiques du matériau, qui interagissent avec chaque moment magnétique du matériau. Tenant compte du fait que ce champ est proportionnelle à l'aimantation, il a proposé un modèle pour expliquer la température de Curie et le paramagnétisme. La théorie de Weiss donne des informations sur l'amplitude de l'aimantation, mais rien ne peut être dit à propos de sa direction.

L'approche phénoménologique du champ moléculaire a été théoriquement justifiée lorsque Werner Heisenberg introduit l'interaction d'échange sur la base de la théorie quantique en 1928 [17]. Il a démontré que cette interaction est à l'origine du champ moléculaire. L'interaction d'échange reflète la répulsion coulombienne électrostatique des électrons sur les atomes voisins (associée au principe d'exclusion de Pauli). L'énergie d'échange dans un système de spins est alors décrit par la somme de toutes les interactions de chaque spin avec les autres. Cet énergie est plus forte pour les moments adjacents et dans les matériaux ferromagnétiques, elle favorise un alignement parallèle des spins.

Un autre modèle pour comprendre le comportement des matériaux ferromagnétiques a été proposé par Edmund C. Stoner en 1938 [18]. Ce modèle prend en compte la structure de bande du matériau ferromagnétique et suppose que le moment magnétique provient des électrons mobiles de la bande *d*. Comme elle repose sur la différente occupation des spins lorsque la température augmente, sans considérer une séparation énergétique réduite d'échange, il prédit des températures de Curie trop élevées.

Ces modèles ne décrivent pas la variation de la direction de l'aimantation, ni, par exemple, l'existence d'un axe d'aimantation facile dans un échantillon cristallin. Pour cela, on doit tenir compte du modèle de Stoner-Wohlfahrt [19] et calculer le minimum d'énergie libre du système (composé par l'énergie d'échange, l'énergie d'anisotropie de forme, l'énergie de l'anisotropie magnéto-cristalline, l'énergie Zeeman et l'énergie de désaimantation), donnée par

$$E_{total} = E_{echange} + E_{anisotropie} + E_{Zeeman} + E_{desaimantation}. \tag{2}$$

L'anisotropie magnétique du système peut provenir de la forme de l'échantillon, des effets magnéto-cristallins et de l'interaction avec un champ externe. L'anisotropie de forme de l'échantillon influe sur la direction préférentielle de l'aimantation due à des interactions dipolaires magnétiques à longue distance. Pour un film mince, par exemple, l'anisotropie de forme oriente l'axe de facile de l'aimantation dans le plan de l'échantillon.

L'anisotropie magnéto-cristalline prend son origine dans l'interaction spin-orbite et explique pourquoi un axe facile d'aimantation est observée indépendamment de la forme de l'échantillon. Il correspond à une orientation préférentielle des moments magnétiques dans le matériau selon les règles de symétrie. L'énergie libre de l'anisotropie magnéto-

cristalline correspond au travail pour changer la direction de l'aimantation.

L'interaction Zeeman décrit l'interaction entre l'aimantation et le champ externe appliqué à l'échantillon. Cette interaction a tendance à aligner les moments magnétiques parallèle ou anti-parallèle au champ externe.

L'interaction d'une impulsion laser d'un matériau soumis à un champ magnétique statique ajoute de l'énergie au système et ainsi des contributions d'énergie différentes doivent être considérées. Il est alors nécessaire d'examiner toutes les contributions d'énergie et les changements possibles induits par la perturbation du champ laser.

Etudes sur la dynamique de l'aimantation - historique

Les premières études en utilisant la technique pompe-sonde se sont fondés sur une configuration uniquement optique et visaient à étudier les processus de relaxation dans les matériaux métalliques après excitation laser. La première a été réalisée en 1983 sur le Cu [20], une augmentation puis une diminution rapides de la réflectivité ont étés observées après l'excitation laser à des échelles de l'ordre de la femtoseconde et de la picoseconde, ce qui a été attribué au chauffage initial d'électrons à une température supérieure à celle du réseau. Il a été montré la possibilité de mesurer temporellement la contribution des électron et du réseau au chauffage du métal. Ces résultats ont été confirmés avec une meilleure résolution temporelle [21] [22] [23].

Depuis lors, différentes techniques femtoseconde ont été développées pour étudier les processus de relaxation dans les métaux comme la photoémission, qui permet l'étude de la thermalisation des électrons [24] [25] [26] et des expériences pompe-sonde résolues en temps qui mesurent de l'efficacité de génération du deuxième harmoniques [27] ou la réflectivité transitoire [28].

En parallèle, les mêmes techniques ont été utilisées pour étudier la dynamique d'aimantation dans les matériaux magnétiques. Les premières études résolues en temps sur les effets d'une impulsion laser ultracourte sur l'aimantation d'un matériau ont été réalisées dans des matériaux simples comme Fe, Ni et Gd. En 1984, des effets magnétiques n'ont pas été observées jusqu'au point de fusion des échantillons de Ni et Fe excité par des impulsions de $5 - 20ps$ [29]. Plus tard, en 1991, des études utilisant des impulsions de $10ns$ pour chauffer l'échantillon et de $30ps$ pour la sonde, ont estimé le temps de relaxation spin-réseau dans les films de Gd à $100 \pm 80ps$ en utilisant la technique de photo-émission résolu en temps [30]. Ce temps de relaxation a été confirmé plus tard par les prédictions théoriques [31]. Le problème jusqu'à présent, était la durée d'impulsion, qui était plus long que les échelles de temps d'intérêt.

En 1996, en utilisant des impulsions laser de $60fs$ dans une configuration Kerr magnéto-optique, notre groupe a démontré la perte ultra-rapide de l'ordre magnétique dans un film ferromagnétique Ni [1]. On a constaté que l'aimantation du film atteint une valeur minimale dans l'échelle de temps sous-picoseconde après excitation laser. La proposition pour comprendre ces effets était d'étendre le modèle de la thermalisation des électrons (appelé modèle à deux température) aux effets de spins. Ces modèles seront plus explorés dans les sections 1.2.1 et 1.2.2.1. Ils ont permis aux auteurs de trouver que la dynamique de températures des électrons et des spins diffèrent dans les premières picosecondes.

Cette étude pionnière a motivé de nombreuses équipes de recherche pour comprendre les mécanismes fondamentaux de l'origine de la désaimantation. Les résultats présentés ont été confirmés par plusieurs études de dynamique de spin en utilisant la spectroscopie Kerr magnéto-optique [32], la technique de génération du deuxième harmoniques [33] [34], l'expérience de photoémission à deux photons [35], etc. En outre, une désaimantation complète d'un film ferromagnétique de $CoPt_3$ a été montré par notre groupe en 1998 [36]. Il a été montré que, à des intensités laser élevés, l'hystérésis disparaît et qu'un état paramagnétique est obtenu à des échelles de temps ultracourtes. Des résultats similaires ont été reproduits sur des films de Ni confirmant ainsi que la désaimantation et la thermalisation des électrons se produisent simultanément [34] [37].

Dans le même temps, les études d'inversion d'aimantation ont été menées avec des particules et ont essayé de prouver la cohérence du modèle Néel-Brown [38] [39] qui traite du renversement de l'aimantation comme un phénomène thermiquement activé. Il déclare que, à n'importe quelle température, les fluctuations thermiques obligent les spins à subir un mouvement de type brownien autour de l'axe facile d'aimantation, avec une probabilité finie que le moment bascule d'une direction à l'autre. La première preuve expérimentale de retournement de l'aimantation au sein d'une nanoparticule ferromagnétique suivant ce modèle a été signalé en 1997 [40].

Une différence entre l'ellipticité et la rotation Kerr résolu en temps et leur dépendance de la température et du champ magnétique a été observée dans $Cu/Ni/Cu$ coins [41]. On a montré que la rotation et l'ellipticité sont différentes et une estimation de la relaxation de spin a été faite entre $0,5$ et $1ps$.

Une étude plus complète et détaillée de la rotation et de l'ellipticité Kerr qui analyse les parties réelles et imaginaires du tenseur diélectrique a été effectuée par notre groupe en 2002 [42]. En utilisant des impulsions de $20fs$, les auteurs ont étudié la thermalisation de spins et de charges à des taux de répétition élevés. Il a été montré que, après la thermalisation des électrons, les parties réelles et imaginaires du vecteur de Voigt sont identiques. En outre, leur variation relative s'est avérée être dix fois plus grande que celle des éléments de la diagonale du tenseur, ce qui montre que les spins dominent la réponse magnéto-optique.

Cependant, au cours de la thermalisation des électrons, les deux composantes du vecteur Voigt suivent des dynamiques différentes, ce que remet en question le formalisme utilisé pour décrire la dynamique de spins non thermalisé et implique des nouveaux formalismes pour la démagnétisation induite par laser. Par exemple, il a été montré que dans des échantillons de $CoPd$, un changement ultra-rapide dans le couplage spin-orbite entraîne l'extinction de l'anisotropie magnétique perpendiculaire des échantillons, ce qui se traduit par une désaimantation [43]. Toutefois, seule la contribution incohérente de ce processus a été observée en raison de la résolution temporelle et de la configuration expérimentale.

Precession

En plus de la désaimantation ultra-rapide, les impulsions laser peuvent également induire une précession de l'aimantation autour d'un champ effectif, qui prend en compte l'anisotropie et le champ extérieur. Nous l'étudierons plus précisément au section 1.2.2.2.

Les premières études dans le domaine ont montré la possibilité de démarrer optiquement une précession magnétique sur une échelle de temps de $10ps$ dans un film ferromagnétique de $CoPt_3$ [44] et dans un film $NiFe/NiO$ [45]. Ces variations comprennent une large contribution du chauffage du réseau. Un modèle quantitatif non microscopique qui permet de dériver les échelles de temps appropriées à partir des principes de la mécanique quantique a été proposé en 2005 [46].

En 2005, notre groupe a étudié la trajectoire en trois dimensions dans l'espace de la précession [47]. Il a été observé que la variation du module initial et de l'orientation de l'aimantation se produit en quelques centaines de femtosecondes et qu'elle est suivie de la précession autour du champ effectif et de l'amortissement. L'analyse polarimétrique utilisée dans les expériences a été présentée comme un procédé bien adapté pour étudier la variation de l'anisotropie associée au chauffage dynamique du réseau.

Dans ces dernières années, l'étude de la précession a permis de développer une importante variété de méthodes pour étudier les mécanismes impliqués dans la réponse magnéto-optique ultra-rapide des matériaux. Elle a été combiné avec des impulsions acoustiques pour étudier la dynamique d'aimantation des filmes ferromagnétiques de Ni [48] et combiné au dopage avec de terre-rares pour étudier l'influence de la concentration de dans les films Co [49], etc.

La possibilité de lancer un mouvement de précession avec la phase qui dépend de la polarisation circulaire gauche ou droite de la lumière a été prouvé [50]. Cette dépendance est attribuée à une interaction cohérente entre les photons et les spins. L'effet Faraday inverse est utilisée pour expliquer l'excitation purement optique et non thermique dans $DyFeO_3$.

Dans la littérature, les effets non thermiques sont habituellement distingués des effets photomagnétiques, qui sont le résultat d'une excitation efficace du système après l'absorption d'un photon, et des effets optomagnétique, qui ne sont pas liés à l'absorption, mais à l'effet Faraday magnéto-optique inverse [51].

L'anisotropie photoinduite est prétendu être à l'origine des effets photomagnétiques dans les grenats [52]. Les impuretés Pb^{2+} remplacent les ions de terres rares dans le site dodécaédrique et agissent comme un récepteur d'électrons. Il crée des trous dans les ions Fe dans le sous-réseau tétraédrique. Pour garder la neutralité, certains ions Fe^{3+} deviennent Fe^{4+}. La photoexcitation induit un transfert de charges entre les ions Fe^{3+} et Fe^{4+} ce qui déplace les ions Fe^{4+} dans des sites avec une symétrie différente, en changeant l'anisotropie magnétique. Il a été démontré que le renversement optique est uniquement dû à l'absorption et est indépendant de la longueur d'onde et de la polarisation [53].

Les effets optomagnétiques sont expliqués à l'aide de l'approche phénoménologique de la création d'un champ magnétique intense pendant l'impulsion laser en raison de l'effet Faraday inverse (lorsque la polarisation de la lumière induit des changements dans l'aimantation du matériau [52]). L'approche microscopique de l'effet peut être considéré comme l'action de deux composantes de l'impulsion laser de fréquences différentes. La première stimule une transition optique à un état virtuel avec fort couplage spin-orbite (avec grande probabilité de renversement de spin) et la deuxième stimule la relaxation vers l'état fondamental avec renversement de spin.

Cependant, une nouvelle approche a été utilisée pour expliquer ces deux phénomènes. Des études sur $GdFeCo$, connu pour le couplage antiferromagnétique entre les moments magnétiques du Gd et du Fe tandis que dans l'état fondamental, montrent un état ferromagnétique transitoire menant au renversement de l'aimantation entraînée par le chauffage ultra-rapide [54]. Cet état est dû à la différence de taux de désaimantation du terre-rare et des sous-réseaux Fe et au transfert de moment angulaire entre eux. Cette explication ne tient pas compte d'une approche de macrospin ni d'une approche micromagnétique. Il nécessite l'utilisation de calculs de spin au niveau atomistique.

Réponse cohérente

En 2009, notre groupe a montré l'existence d'une composante cohérente dans la réponse magnéto-optique, associée à la dynamique d'aimantation, et que cette composante est dépendant de la polarisation [4]. Il est important de souligner ici que le grand défi de la mesure de la composante cohérente est d'être capable de l'isoler de la dynamique des populations (dynamique de la thermalisation des spins) présentes dans le signal Faraday. La durée de vie des populations de spins est donnée par le temps T_1 et la dynamique de

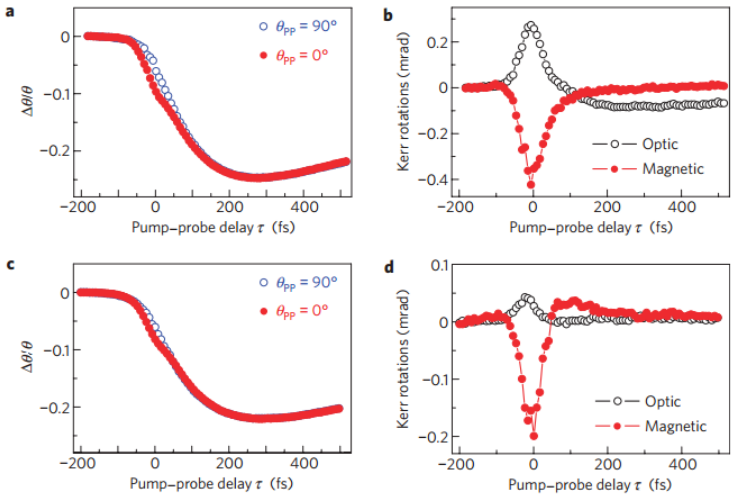

Figure 6: Rotation Kerr différentiel pour un film de Ni (a) et pour un film de $CoPt_3$ (c) pour les polarisations de pompe et sonde perpendiculaires ou parallèles. Contributions électronique et magnétique cohérentes à la dynamique de la polarisation de la sonde pour un film de Ni (b) et pour un film de $CoPt_3$ (d). Figure de la référence [4].

déphasage de la réponse cohérente est caractérisé par le temps T_2.

Dans cette étude, on a montré que si les polarisations des faisceaux sonde et pompe sont parallèles, on voit la composante cohérente, alors qu'elle est très réduite lorsque les polarisations sont perpendiculaires, comme représenté sur les courbes de la figure 6. De cette façon, il est possible d'extraire la composante cohérente d'un signal de rotation Kerr en soustrayant l'un de l'autre.

Cette méthode révèle l'existence de la composante magnéto-optique cohérent associée à des états de spin, alors que les signaux magnétiques sont obtenus après une différence de polarité opposée du champ magnétique statique. Cependant, ce procédé souffre du fait qu'il ne permet pas la mesure de la contribution cohérente seule. Pour cela, dans cette thèse, nous avons utilisé le mélange à quatre ondes magnéto-optique, une procédure similaire au bien connu effet d'auto-diffraction [55].

Objectifs

La présente thèse vise à étudier la dynamique cohérente de charges et de spins qui se passe avant la thermalisation. Nous allons montrer que les configurations de mélange à quatre ondes magnéto-optiques permettent de mesurer directement la dynamique cohérente dans un film de grenat, un processus que nous attribuons à l'interaction spin-orbite. Le défi à relever est l'échelle de temps très courte au cours de laquelle ces processus magnéto-

optiques cohérentes se produisent. Il a fallu un set-up spécifique avec des impulsions optiques ultracourtes.

Le temps de cohérence T_2 peut avoir une origine optique ou magnéto-optique. Dans cette thèse, nous cherchons à mesurer le temps de cohérence électronique et le temps de cohérence électromagnétique utilisant les configurations de mélange à quatre ondes et de mélange à quatre ondes magnéto-optiques.

Organization du manuscrit

Cette thèse est organisé comme suit:

- Chapitre 1: les effets optiques et magnéto-optiques qui permettent de comprendre les résultats expérimentaux sont présentés. Nous allons décrire la réponse magnéto-optique linéaire et non linéaire de films magnétiques et discuter les divers processus de relaxation impliquant la dynamique des charges et spins. Nous discutons de l'influence de la phase spectrale sur le signal de mélange à quatre ondes, point d'intérêt dans cette thèse.

- Chapitre 2: nous décrivons une approche théorique qui permet de comprendre les effets magnéto-optique cohérents dans les systèmes magnétiques représentés par des états de spins discrets. Nous présentons l'hamiltonien de l'interaction spin-orbite ainsi qu'un modèle d'un atome comme l'hydrogène, représenté par huit niveaux, ce qui est cohérent pour décrire les effets magnéto-optiques ultra-rapides et, par conséquent, la dynamique des cohérences et des populations de ces niveaux.

- Chapitre 3: dans la première partie, nous décrivons l'échantillon étudié. Nous examinons certaines propriétés importantes des grenats, en commençant par les grenats trouvés dans la nature, puis nous décrivons les propriétés apportées par différents composants des grenats synthétiques. Dans la deuxième partie, les techniques expérimentales utilisées dans cette thèse sont présentées, à partir de la description de la génération d'impulsions femtoseconde et des différents systèmes que nous avons utilisés jusqu'au procédures d'analyse des données.

- Chapitre 4: les résultats que nous avons obtenus avec les différents systèmes laser sont présentés. Nous discutons ensuite l'évolution dans le temps des spins et des charges, tant du point de vue de leurs dynamique des cohérences que de la dynamique des populations.

Chapter 1

Magneto-optical response in the frequency and time domains

In this chapter, we introduce different phenomena present in the interaction of light and matter. The aim of this part is to set a basis of concepts and descriptions that will allow the development of the theoretical and experimental parts that will follow.

We present the macroscopic polarization as a way to describe the response of the material to the optical excitation. We show that this polarization is composed by a linear and a nonlinear part, being this last one of different orders.

In the first part, the description of nonlinear optical effects is aimed at, as they are often mentioned throughout the thesis. The second harmonic generation, the Kerr effect, the self-phase modulation and the four-wave mixing are presented as examples of nonlinear effects, present when the light field is intense enough.

We briefly review the second harmonic generation as a particular case of the sum frequency generation and we show how the frequency doubling is made.

We present the Kerr effect and develop the behavior of the refractive index as a function of the incident light field intensity.

The instantaneous frequency of a gaussian pulse propagating in a medium with variable refractive index is obtained in the description of the self-phase modulation showing the frequency drift.

We present the four-wave mixing (FWM) configuration that has been used in the experiments performed in this thesis as a tool to access the coherences relaxation time T_2 directly. It is briefly reviewed in the case of a two-level system. We describe the different geometries and what is present in the signals emitted in each direction. We remind then the effect of the photon echo as a special case of the FWM in the case of inhomogeneous

broadening.

In the second part, the description of nonlinear magneto-optical effects is reviewed. Assuming that the laser excitation heats the material, we remind how the charges dynamics can be explained by the two-temperature model, that considers the interaction of the electrons and the lattice.

When one considers a third bath, the spins, the magnetization dynamics is described via the three-temperature model. We also present the precession as a way of studying the spins dynamics.

We present then the magneto-optical Kerr and Faraday effects and how to obtain the terms of the dielectric tensor through a polarimetric pump and probe experiment, via the Faraday or Kerr rotation and ellipticity. We present the description of the time-resolved Faraday effect, describing the different components of the Faraday rotation and ellipticity.

The magneto-optical four-wave mixing (MO-FWM) is also presented. We extend the description of the FWM to the magneto-optical configuration.

In the third part, we study the effects of propagation in the temporal field and phase profiles. The transformation between time domain and frequency domain is presented in the description of the group velocity dispersion. We show how the different refractive indices seen by each component of the spectrum can be at the origin of a chirp in the pulse and how this chirp can affect quantitatively the pulse duration.

Considering no spectral phase, we show how it is possible to analyse the MO-FWM signal as a convolution of a gaussian pulse with an exponential decay. We also present results obtained from the simulations of FWM signals (based on a two-level system and on homogeneous broadening) for different spectral phases to show the role of the phase in the coherent response of a medium to ultrashort laser pulses.

1.1 Nonlinear optical processes

The optical processes that describe the interaction of a light field with matter can be classified according to the order of the response with respect to this field. The medium polarization P couples with the laser field and oscillates at the frequency of the incident radiation. By increasing the order of dependance, the polarization can be written as follows.

$$\begin{aligned} P &= P^{(1)} + P^{(NL)} \\ &= P^{(1)} + P^{(2)} + P^{(3)} + ... \end{aligned} \tag{1.1}$$

$P^{(1)}$ is the linear polarization. Processes likes absorption, light propagation, reflection and refraction involving a weak incoming field are all related to $P^{(1)}$. The main characteristic of a linear medium is that two light beams can not interact on it.

Before the discovery of the first laser, although the Pockels and the Kerr effects had been known since the beginning of the nineteenth century, only DC fields were capable of producing enough intensity to reach a nonlinear optical regime. In 1928, C. V. Raman succeeded performing experiments in which he could see the vibration modes of molecules using the light from the sun. He discovered then the Raman effect, a third order nonlinear optical process [56]. Another breakthrough in the domain was the classic experiment by Franken et al. [57] in which the second harmonic generation was demonstrated in quartz with the use of ruby lasers. Since then, the field of nonlinear optics has continued to grow and proved to be a source of new phenomena and optical techniques.

The nonlinear optics describes the response of a material under a high power dependence on the external electric field. The different terms of the polarization, shown in equation 1.1, can be written in terms of the light oscilating electric field at frequency ω $E(\omega) = (E_x(\omega), E_y(\omega), E_z(\omega))$, as follows.

$$\begin{aligned} P_i(\omega_i) = \varepsilon_0 \sum_j \chi^{(1)}_{i,j}(\omega_i;\omega_j) E_j(\omega_j) \\ + \varepsilon_0 \sum_{j,k} \chi^{(2)}_{i,j,k}(\omega_i;\omega_j,\omega_k) E_j(\omega_j) E_k(\omega_k) \\ + \varepsilon_0 \sum_{j,k,l} \chi^{(3)}_{i,j,k,l}(\omega_i;\omega_j,\omega_k,\omega_l) E_j(\omega_j) E_k(\omega_k) E_l(\omega_l) + ... \end{aligned} \tag{1.2}$$

where $\chi^{(n)}$ is the nonlinear susceptibility tensor of n^{th} order that describes the nonlinear response of the material.

Examples of nonlinear effects are the sum frequency generation, the difference frequency generation, the Kerr effect, the Pockels effect, the self-phase modulation and the four-wave mixing.

1.1.1 Second harmonic generation

The second harmonic generation is a special case of the sum frequency generation. Examples of the different possible interactions of two waves of frequencies ω_1 and ω_2 in a nonlinear medium are shown in figure 1.1. This interaction can generate frequencies oscillating at the sum or at the difference incident frequencies.

In the case of the second harmonic generation, the oscillating electric field at frequency ω interacts with the material, which response is described by the tensors $\chi^{(1)}$ and $\chi^{(2)}$.

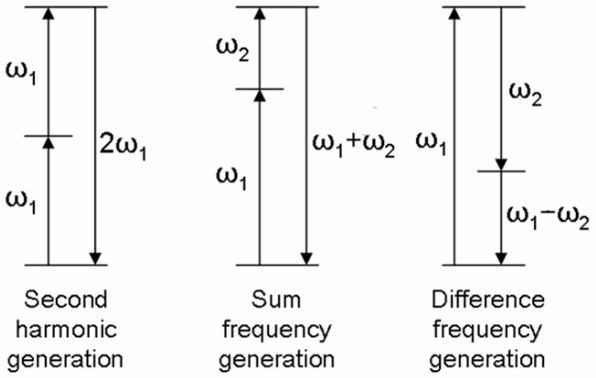

Figure 1.1: Energy diagram for the second harmonic generation, for the sum frequency generation and for the difference frequency generation.

The electrons of the material are excited to a virtual state with the energy of the first photon and then excited again with the energy from the second photon emitting then a photon with twice the energy of the incident ones but half of the frequency.

The induced polarization in the material, at frequency ω is written as

$$P = P^{(1)}(\omega) + P^{(2)}(\omega), \tag{1.3}$$

being

$$P^{(1)}(\omega) = \varepsilon_0 \chi^{(1)}(\omega;\omega) E_{0,\omega} sin(\omega t) \text{ and} \tag{1.4}$$

$$\begin{aligned} P^{(2)}(\omega) &= \varepsilon_0 \chi^{(2)}(2\omega;\omega,\omega) E_{0,\omega} E_{0,\omega} sin^2(\omega t) \\ &= \frac{\varepsilon_0}{2} \chi^{(2)}(2\omega;\omega,\omega) E_{0,\omega} E_{0,\omega} [1 - cos(2\omega t)]. \end{aligned} \tag{1.5}$$

The component that oscilates at frequency 2ω characterizes the frequency doubling.

1.1.2 Kerr effect

In 1875, John Kerr observed that an isotropic transparent substance becomes birefringent when excited by an electric field [3]. The medium takes on the characteristics of an uniaxial crystal whose optical axis corresponds to the direction of the applied field. This means that the refractive index of the medium depends on the polarization of light crossing it.

The Kerr effect is a third order nonlinear effect and can be described by a light field $E(\omega)$ that propagates in a nonlinear medium and couples with the medium polarization $P(\omega)$. The material radiates then a field with changed polarization. The reflected field,

composed by the incident field and the emitted field, has then different polarization from the incident field [58].

The polarization of the material induced by $E(\omega)$ is written as [59]

$$P(\omega) = \varepsilon_0 \left[\chi^{(1)} E_1(\omega) + \frac{3}{4} \chi^{(3)} E_1(\omega) E_2^*(\omega) E_3(\omega) \right]. \tag{1.6}$$

If the medium is isotropic,

$$P(\omega) = \varepsilon_0 \left[\chi^{(1)} + \frac{3}{4} \chi^{(3)} E_2^*(\omega) E_3(\omega) \right] E_1(\omega) = \varepsilon_0 \left[\chi^{(1)} + \frac{6\chi^{(3)}}{4 n_0 c \varepsilon_0} I \right] E_1(\omega) \tag{1.7}$$

where $I(\omega) = n_0 \varepsilon_0 c \left[E_2^*(\omega) E_3(\omega) \right] / 2$ is the intensity of the laser field. Knowing that $P = \varepsilon_0 \chi E$, equation 1.7 presents $\chi = \chi_{linear} + \chi_{nonlinear}$. As $\chi^{(1)} = n_0^2 - 1$, one can write the refractive index n as

$$n^2 - 1 = \chi^{(1)} + \frac{6\chi^{(3)}}{4 n_0 c \varepsilon_0} I. \tag{1.8}$$

With that, it is found that

$$n \cong n_0 + \frac{n_2}{2} I \text{ where } n_2 = \frac{3\chi^{(3)}}{4 n_0^2 c \varepsilon_0} I, \tag{1.9}$$

being n_0 the linear refractive index and n_2 the nonlinear refractive index [60], that describes the strength of the coupling between the electric field and the nonlinear medium.

1.1.3 Self-phase modulation

Ultrashort laser pulses have an important peak power, specially in the amplifying cavity. Being this power focalised in μm spots, the fluence at this point can reach several GW/cm^2. For these power densities, one has to take into account the variations of the index of the material due to the Kerr effect, even when the materials are transparent to the laser field. This variations produce a shift in the instantaneous phase of the pulse that has the same temporal shape as the optical intensity. This phenomenon is called self-phase modulation, a third order non-linear effect, responsible for the spectral broadening of the pulse and its frequency modulation.

For a gaussian light pulse whose simplified intensity is described by $I(t) = I_0 exp(-t^2/\tau^2)$ and using relation 1.9, the variation in time of the refractive index is given by

$$\frac{dn}{dt} = \frac{n_2}{2}\frac{dI}{dt} = -\frac{n_2 I_0}{2} \times \frac{2t}{\tau^2} exp\left(\frac{-t^2}{\tau^2}\right). \tag{1.10}$$

The phase being defined by

$$\phi(t) = \omega_0 t - kx = \omega_0 t - \frac{2\pi}{\lambda_0} n(I) L, \tag{1.11}$$

where L is the distance that light has propagated, the instantaneous frequency $\omega(t)$ is written as

$$\omega(t) = \frac{d\phi(t)}{dt} = \omega_0 - \frac{2\pi L}{\lambda_0}\frac{dn(I)}{dt}. \tag{1.12}$$

Using 1.10,

$$\omega(t) = \omega_0 + \frac{2\pi L n_2 I_0 t}{\lambda_0 \tau^2} exp\left(\frac{-t^2}{\tau^2}\right). \tag{1.13}$$

$\omega(t)$ gives the frequency shift of each part of the pulse and shows that lower frequencies are created in the negative time components of the pulse (being $t = 0$ its intensity center) and higher frequencies, in the positive time components of the pulse. The pulse is then temporally chirped, which means it presents a quadratic time dependent phase. The linear case corresponds to the carrier frequency ω_0.

1.1.4 Four-wave mixing

The four-wave mixing (FWM) is a third order nonlinear effect described by the third order nonlinear susceptibility $\chi^{(3)}$. It is based on the concept of three electromagnetic fields (ω_i, $\overrightarrow{k}_i : i = 1, 2, 3$) interacting in a medium to produce a fourth field (ω_4, $\overrightarrow{k}_4$). The first two fields cause the oscillation of the dipoles and, correspondingly, the polarization of the material is modulated at the same frequency. The third field also interacts with the material and determines in which directions the emitted field will occur, with the constraint of the conservation of energy, to be shown ahead.

From an interaction point of view, one can understand the emission of the fourth field (the FWM) as the diffraction of the third field on the grating created by the two others. In that sense, such FWM configuration allows probing the dynamics of the material, namely the coherence time of the grating, that corresponds to the notion of T_2, and its lifetime, that corresponds to T_1.

Directions of emission

The vector $\overrightarrow{Q}$ of the grating and its step Λ are a function of the angle θ between the two beams and are given by

$$\overrightarrow{Q} = \pm(\overrightarrow{k_1} - \overrightarrow{k_2}) \text{ and } \Lambda = \frac{2\pi}{|\overrightarrow{Q}|} = \frac{\lambda}{2sin(\theta/2)} \approx \frac{\lambda}{\theta} \text{ if } \theta \ll 1. \tag{1.14}$$

When a third field of wave vector $\overrightarrow{k_3}$ probes the grating, it is difracted to the m^{th} order in the direction $\overrightarrow{k_4}$ given by

$$\overrightarrow{k_4} = \overrightarrow{k_3} + m\overrightarrow{Q}. \tag{1.15}$$

In a three-beam configuration, the signal in the direction $\overrightarrow{k_4}$, is then given by

$$\text{for } \overrightarrow{Q} = \overrightarrow{k_1} - \overrightarrow{k_2} \begin{cases} \overrightarrow{k_4} = \overrightarrow{k_3}, & \text{for } m = 0; \\ \overrightarrow{k_4} = \overrightarrow{k_1} - \overrightarrow{k_2} + \overrightarrow{k_3}, & \text{for } m = 1; \\ \overrightarrow{k_4} = 2\overrightarrow{k_1} - 2\overrightarrow{k_2} + \overrightarrow{k_3}, & \text{for } m = 2; \text{ etc;} \end{cases} \tag{1.16}$$

$$\text{and for } \overrightarrow{Q} = \overrightarrow{k_2} - \overrightarrow{k_1} \begin{cases} \overrightarrow{k_4} = \overrightarrow{k_3}, & \text{for } m = 0; \\ \overrightarrow{k_4} = -\overrightarrow{k_1} + \overrightarrow{k_2} + \overrightarrow{k_3}, & \text{for } m = 1; \\ \overrightarrow{k_4} = -2\overrightarrow{k_1} - 2\overrightarrow{k_2}, + \overrightarrow{k_3} & \text{for } m = 2; \text{ etc.} \end{cases} \tag{1.17}$$

The different values of the coefficient m are associated to the different orders of nonlinearity: $m = 0$ represents a first order nonlinearity, $m = 1$ represents a third order nonlinearity and $m = 2$ represents a fifth order nonlinearity.

In a two-beam configuration, considering $\overrightarrow{k_2} = \overrightarrow{k_3}$ or $\overrightarrow{k_1} = \overrightarrow{k_3}$, the signal in the direction $\overrightarrow{k_4}$, is then given by

$$\text{for } \overrightarrow{Q} = \overrightarrow{k_1} - \overrightarrow{k_2} \text{ and } \overrightarrow{k_1} = \overrightarrow{k_3} \begin{cases} \overrightarrow{k_4} = \overrightarrow{k_1}, & \text{for } m = 0; \\ \overrightarrow{k_4} = 2\overrightarrow{k_1} - \overrightarrow{k_2}, & \text{for } m = 1; \\ \overrightarrow{k_4} = 3\overrightarrow{k_1} - 2\overrightarrow{k_2}, & \text{for } m = 2; \text{ etc;} \end{cases} \tag{1.18}$$

$$\text{and for } \overrightarrow{Q} = \overrightarrow{k_2} - \overrightarrow{k_1} \text{ and } \overrightarrow{k_2} = \overrightarrow{k_3} \begin{cases} \overrightarrow{k_4} = \overrightarrow{k_2}, & \text{for } m = 0; \\ \overrightarrow{k_4} = 2\overrightarrow{k_2} - \overrightarrow{k_1}, & \text{for } m = 1; \\ \overrightarrow{k_4} = 3\overrightarrow{k_2} - 2\overrightarrow{k_1}, & \text{for } m = 2; \text{ etc.} \end{cases} \tag{1.19}$$

These specific directions can be spatially distinguished after the material and, therefore, detected independently. This is how the population and coherence will be separated later on, as shown ahead in chapter 2.

Two-level system description

The FWM is the basis of the technique of magneto-optical four-wave mixing that we demonstrate in this thesis to be of great value to study the coherences dynamics, as mentionned in the Introduction. Here we review briefly the concept of quantum coherence. We consider the case of an electron in a two-level system, composed by a ground state a and an excited state b, as shown in figure 1.2.

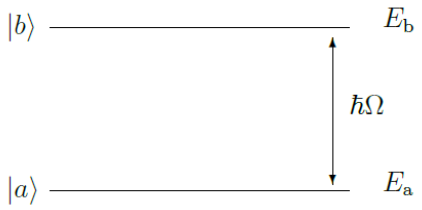

Figure 1.2: Scheme of a two-level system.

One can write the response of the system using the Liouville formalism. In the base of the states $\{|a\rangle, |b\rangle\}$, the density matrix is then given by

$$\rho = \begin{pmatrix} \rho_{aa} & \rho_{ab} \\ \rho_{ba} & \rho_{bb} \end{pmatrix} = \begin{pmatrix} 1-n & p \\ p^* & n \end{pmatrix}. \tag{1.20}$$

The diagonal elements represent the population of each energy level $|a\rangle$ and $|b\rangle$. To an isolated two-level system, the total population is constant, that is why the population of the fundamental state is $1-n$ while the population of the excited state is n. The nondiagonal elements show the interference effects between the pure states $|a\rangle$ and $|b\rangle$ and are called coherences.

The response of a system exposed to an electromagnetic field is determined by the macroscopic polarization given by the dipolar moment of the system, $\overrightarrow{D}$, and the density matrix as follows.

$$\overrightarrow{P}(t) = Tr[\rho\overrightarrow{D}] \tag{1.21}$$

The system in equilibrium is described by the non perturbed hamiltonian H_0.

$$H_0 = \begin{pmatrix} E_a & 0 \\ 0 & E_b \end{pmatrix} \tag{1.22}$$

When the system is optically excited, the hamiltonian of interaction with the field and the hamiltonian of relaxation are added,

$$H = H_0 + H_{int} + H_{relax}, \tag{1.23}$$

being H_{int} written as

$$H_{int} = -\overrightarrow{D} \cdot \overrightarrow{E} = \begin{pmatrix} 0 & -\overrightarrow{D}_{ab} \cdot \overrightarrow{E} \\ \overrightarrow{D}^*_{ab} \cdot \overrightarrow{E}^* & 0 \end{pmatrix}. \tag{1.24}$$

H_{relax} describes the return of the system to equilibrium.

In a phenomenological approach, the processus described by H_{int} and H_{relax} are described by relaxation rates. In first approximation, they are described by two phenomenological constants:

$$\text{the population variation, given by } \left(\frac{dn}{dt}\right)_{relax} = -\frac{n}{T_1} \tag{1.25}$$

$$\text{and the coherence variation, given by } \left(\frac{dp}{dt}\right)_{relax} = -\frac{p}{T_2}. \tag{1.26}$$

T_1 is the longitudinal relaxation time, which means the lifetime of the excited level and T_2 is the transverse relaxation time, that corresponds to the relaxation time of the coherence.

The evolution of the system is then reduced to two coupled equations in n and p, the optical Bloch equations.

To develop these equations, one treats the electric field as a perturbation and develops the density matrix in a series of terms of different orders. With that, it is possible to prove that, in the scope of a pump and probe experiment, where τ is the delay between the two pulses, the intensity of the diffracted signals in the direction $2\overrightarrow{k_2} - \overrightarrow{k_1}$ and $2\overrightarrow{k_1} - \overrightarrow{k_2}$, for the two-beam configuration, and in directions $\overrightarrow{k_1} - \overrightarrow{k_2} + \overrightarrow{k_3}$ and $-\overrightarrow{k_1} + \overrightarrow{k_2} + \overrightarrow{k_3}$, for the three-beam configuration, depends on T_2, as follows [61].

$$I(\tau) \propto exp\left(-\frac{2\tau}{T_2}\right) \tag{1.27}$$

Inhomoheneous spectral broadening - photon echo

The development shown so far takes into account the electronic transitions broadened in a homogeneous way. The homogeneous broadening defines the width associated to a transition. It corresponds to the relaxation rate of the coherence associates to this level. The inhomogeneous broadening comes from the study of N atoms having slightly different frequencies. When the N dipoles are out of phase, the global coherence is lost. Considering an inhomogenous distribution (two-level system with different transition energies) in the dynamic measurement of the FWM, the signal becomes a photon echo [62] [63] and the relaxation time is divided by two with respect to the one of the equivalent homogeneous system.

One can understand the phenomenon as follows: let us consider a material with inhomogeneous broadening $\Delta\omega_0$ of a particular dipole frequency ω_0. A first pulse with enough spectral width ($\Delta\omega_L \geq \Delta\omega_0$) excites the full linewidth. The assembly of dipoles will therefore oscillate with slightly different frequencies and dephase. A suitable second pulse arrives after a time τ and adds a phase π to each of the individual oscillators, what causes them to rephase. Knowing that the oscillators took a time τ to be dephased, they take the same time τ to be in phase again. It is then after a time 2τ that the photon echo is emitted.

$$I(\tau) \propto exp\left(-\frac{4\tau}{T_2}\right) \tag{1.28}$$

In a microscopic approach, one can say that the dipoles oscillation decay with a time T_2^h, called homogeneous, after the excitation. The phase relation between the dipoles oscillations decays with a time T_2^{inh}, called inhomogeneous, that is shorter than T_2^h, so the oscillations are still observed.

1.2 Nonlinear magneto-optical processes

The interaction of light with matter can be viewed in many ways. So far, the processes presented have shown the optical interaction of a light pulse with matter. If the medium in question is magnetic, the magneto-optical response of the material in a static or time

dependent magnetic field can be studied via different phenomena, that will now be presented.

To study the evolution of the magnetization and consequently the spin dynamics, it is necessary to explore magneto-optical time-resolved experiments. The aim of studying the evolution of the magnetization is to understand the timescales and mechanisms involved in the spins dynamics.

To understand the magneto-optical processes involved in the different experimental configurations, we present here the phenomenological description of the magneto-optical response using the two-temperature model and its extension, the three-temperature model. These thermal approaches describe the laser-induced magnetization dynamics caused by the heating of electrons due to the laser pulse that can be of any polarization.

We present also a brief description of the magnetization precession.

1.2.1 Charges dynamics - two-temperature model

The origin of the emission of electrons when materials are exposed to ultrashort laser pulses is set on the photoelectric effect and on the heating of the material [64]. The importance of each one of these effects depends on the laser pulse duration.

If the pulse is shorter than the characteristic time for the transfer of energy between the electron and the lattice, the electronic temperature increases.

The two-temperature model [65] describes the exchange of heat between electrons and lattice after a laser pulse excitation and is valid only after the electrons are thermalized, which means that the electron-electron scattering is no longer the dominating phenomenon.

Diffusive effects are not taken into account in this approach that is then well-adapted for metals having a thickness of the order of the laser penetration depth and appropriate to discuss the main general effects occuring in less than $10ps$.

The rate equations for the electrons temperature T_e and the lattice temperature T_l are

$$C_e(T_e)\frac{dT_e}{dt} = -G_{el}(T_e - T_l) + P(t) \text{ and} \tag{1.29}$$

$$C_l(T_l)\frac{dT_l}{dt} = G_{el}(T_e - T_l), \tag{1.30}$$

where C_e and C_l are the electronic and lattice specific heats, G_{el} is the electron-phonon coupling constant and $P(t)$ is the laser power density absorbed by the material.

The initial temperature of both the lattice and the electrons is the ambient temperature and, for a weak temperature elevation, the specific heats are constant and yh equations above become linear.

Looking in more details, it is possible to take into account the athermal electron population created by the exciting pulse. The number of excited particles $n(\epsilon, t)$ (being ϵ the difference between the energy and the Fermi energy) becomes now the relevant dynamic quantity for ultrashort times (during the thermalization of the electronic distribution).

The electronic distribution is separated into a thermalized part, characterized by T_e and a nonthermal contribution, characterized by $n(\epsilon, t)$. Then, three coupled differential equations are necessary:

$$\frac{dn}{dt} = -\alpha n(\epsilon, t) - \beta n(\epsilon, t) + P(t) \tag{1.31}$$

$$C_e(T_e)\frac{dT_e}{dt} = -G_{el}(T_e - T_l) + \alpha n(\epsilon, t) \tag{1.32}$$

$$C_l(T_l)\frac{dT_l}{dt} = G_{el}(T_e - T_l) + \beta n(\epsilon, t), \tag{1.33}$$

where $\alpha = 1/\tau_{th}$ (τ_{th} being the thermalization time) and β describes the heating rate of the thermalized electrons and phonons from the nonthermal electrons, respectively [10].

1.2.2 Spins dynamics

1.2.2.1 Three-temperature model

The two-temperature model does not consider the interactions with spins. Proposed by our group in 1996 [1], the three-temperature model considers that the specific heat of ferromagnetic metals is usually split into electronic, magnetic and lattice contributions. The proposed approach is then to describe ultrafast spin dynamics in an extension of the two-temperature model to a phenomenological model considering three baths: spins, electrons and lattice. That results in the addition of an equation related to the spin subsystem.

$$C_e(T_e)\frac{dT_e}{dt} = -G_{el}(T_e - T_l) - G_{es}(T_e - T_s) + P(t) \tag{1.34}$$

$$C_l(T_l)\frac{dT_l}{dt} = G_{el}(T_e - T_l) - G_{sl}(T_l - T_s) \tag{1.35}$$

$$C_s(T_s)\frac{dT_s}{dt} = G_{es}(T_e - T_s) - G_{sl}(T_l - T_s) \tag{1.36}$$

Typically one has $C_e(T_e) = \gamma T_e$, with $\gamma = 6 \cdot 10^3 J/m^3 K^2$, and $C_l(T_l)$ constant. $C_s(T_s)$ can be obtained from the total specific heat by subtracting the linear contribution coming from the lattice and the electrons [1].

A comparison between the estimated temperatures from experimental data and the calculated temperatures from the equations above in the case of a nickel film is shown in

figure 1.3.

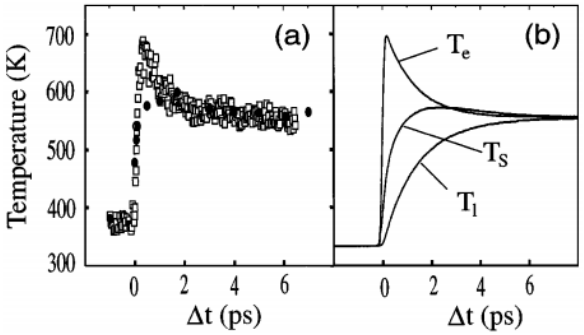

Figure 1.3: (a) Estimated experimental electronic and spin temperatures obtained in a nickel film of $22nm$ thickness. (b) Calculated spin, lattice and electronic temperatures. Figure from reference [1].

This approach is valid when the components of the magnetization follow adiabatically the changes of temperature. For shorter delays, the non-thermal electrons can also be included, as discussed in reference [10].

This model raises the question of how to describe the laser induced ultrafast magnetization dynamics before the complete thermalization of electrons. The difference of populations between spins up and spins down is not expected to evolve with the same rate as the electron relaxation, concept based on the Stoner excitations and the spin-orbit interaction.

The large energy acquired by the electrons after the laser excitation (above the Fermi level) allows to consider a Stoner model, that describes a modified distribution of electrons and spin populations in the d bands after excitation. The magnetization is then given as a function of spin polarized densities of state.

These excited populations of electrons are strongly coupled in a ferromagnetic metal. The consequence is that the population of spin down and spin up are different, even when they are induced by optical transitions (independently of the light polarization). As the energy associated to the spin-orbit interaction is typically of a few tens of meV, efficient spin flips are expected to be observed in the time scale of $\sim 100fs$, leading to demagnetization.

These arguments justify then the concept of different temperatures for electrons, spins and phonons.

1.2.2.2 Precession

The interaction with a short laser pulse can be seen as a perturbation to the effective magnetic field H_{eff} of the sample that takes into account the anisotropy field of the sample and the external magnetic field to which the sample is exposed. A collective reponse of magnetic moments can be then induced in the picosecond time scale, giving rise to precession of magnetization around the effective field. The magnetic moments are out of equilibrium and will realign along the new field direction through a precessional motion.

At constant temperature, this motion is described by the phenomenological Landau-Lifshits-Gilbert equation.

The ensemble of magnetic moments undergo a precessional motion if placed in a magnetic field. When no damping is considered, this motion is described by the torque equation. Being the angular moment $\overrightarrow{L}$ associated to the magnetic moment $\overrightarrow{m}$ given by

$$\overrightarrow{L} = \frac{\overrightarrow{m}}{\gamma}, \tag{1.37}$$

where $\gamma = g\frac{e}{2m_e}$ is the gyromagnetic ratio (g is the gyromagnetic splitting Landé factor; $g = 2$ for a free electron, $g = 2,10$ for Fe, $g = 2,18$ for Co and $g = 2,21$ for Ni [66]) and being the torque on the magnetic moment $\overrightarrow{m}$ given by

$$\overrightarrow{T} = \mu_0 \overrightarrow{m} \times \overrightarrow{H}, \tag{1.38}$$

where μ_0 is the permeability and $\overrightarrow{H}$ is the magnetic field, one can write the following motion equation.

$$\frac{d\overrightarrow{L}}{dt} = \frac{d\overrightarrow{m}}{dt}\frac{1}{\gamma} = \mu_0 \overrightarrow{m} \times \overrightarrow{H}, \tag{1.39}$$

Being the magnetization $\overrightarrow{M} = \frac{\overrightarrow{m}}{V}$ given as a function of the volume V of the ensemble of magnetic moments, one can write the equation of motion of the magnetization vector of this ensemble as

$$\frac{d\overrightarrow{M}}{dt} = \gamma\mu_0(\overrightarrow{M} \times \overrightarrow{H}), \tag{1.40}$$

being the frequency of this precessional motion given by $f_{prec} = \frac{1}{2\pi}\frac{e\mu_0 H}{m}$.

The Landau-Lifshits equation is based on this dynamical equation, but considers an effective field composed by the external applied field $\overrightarrow{H}_{ext}$, the anisotropy field $\overrightarrow{H}_{ani}$

(magneto-crystaline and shape anisotropy) and the demagnetization field $\overrightarrow{H}_0$ [67], as follows.

$$\overrightarrow{H}_{eff} = \overrightarrow{H}_{ext} + \overrightarrow{H}_{ani} + \overrightarrow{H}_0 \tag{1.41}$$

In real systems, the motion of the magnetization is often damped, possibly due to complex interactions of the electrons moment with the crystal lattice and its defects or impurities, with other electrons or phonons, etc [68]. So, a damping term was added to the equation, used to describe the precession of the magnetization in bulk materials, that is now written as follows.

$$\frac{d\overrightarrow{M}}{dt} = \gamma\mu_0(\overrightarrow{M} \times \overrightarrow{H}_{eff}) - \frac{\lambda}{M_S^2}[\overrightarrow{M} \times (\overrightarrow{M} \times \overrightarrow{H}_{eff})], \tag{1.42}$$

where λ is an ajustable parameter of the Landau-Lifshits damping and M_S is the magnetization at saturation.

Another phenomenological description of the magnetization precession, valid for nanoparticles, proved to be equivalent to the one proposed by Landau and Lifshits [69], was proposed by Gilbert in 1955 [70] [71]. This approach uses another damping term based on the damping constant $\alpha = \frac{\lambda}{\gamma M}$ and gave rise to the Landau-Lifshits-Gilbert equation, presented now.

$$\frac{d\overrightarrow{M}}{dt} = \gamma\mu_0(\overrightarrow{M} \times \overrightarrow{H}_{eff}) - \frac{\alpha}{M_S}\left(\overrightarrow{M} \times \frac{d\overrightarrow{M}}{dt}\right) \tag{1.43}$$

Bloch has developed in 1946 a description of the paramagnetic resonance in terms of the two phenomenological time constants T_1 and T_{2p}, the longitudinal and tranverse relaxation times (in the case of the Landau-Lifshits-Gilbert equation, one can say only one damping characteristic time is considered as the modulus of the magnetization is constant) [72]. This approach considers separetely the three components of the magnetization vector. This is the basis of the model proposed by Bloembergen in 1950 [73] that has applied Bloch's description to the ferromagnetic resonance. For an external field applied in the x direction and considering only the Zeeman contribution to the total magnetic field H_{eff}, the magnetization component M_x relaxes to the equilibrium position along the applied field with a rate proportional to its value and to M_S. The components M_y and M_z, tranverse to the external field vanish to zero with a characteristic time T_{2p}. The Bloch or Bloch-Bloembergen equations are given by

$$\frac{dM_x}{dt} = \gamma\mu_0(\overrightarrow{M} \times \overrightarrow{H}_{eff})_x - \frac{M_S - M_x}{T_1}, \tag{1.44}$$

$$\frac{dM_y}{dt} = \gamma\mu_0(\overrightarrow{M} \times \overrightarrow{H}_{eff})_y - \frac{M_y}{T_{2p}} \text{ and} \tag{1.45}$$

$$\frac{dM_z}{dt} = \gamma\mu_0(\overrightarrow{M} \times \overrightarrow{H}_{eff})_z - \frac{M_z}{T_{2p}}. \tag{1.46}$$

It is important to remind here that the tranverse relaxation time T_{2p} from the Bloch formalism is the relaxation time of the macrospins, which means that it represents the relaxation of the strongly coupled magnetic moments and can be seen as a relaxation time related to the lost of coherence between all spin states.

The Landau-Lifshits-Gilbert equation is well adapted to describe the magnetization dynamics induced by short magnetic field pulses, for example, because it does not consider a temperature modification during the precession of the magnetization. However, when using an optical excitation, the regime in nonequilibrium can not be described the same way, as the pulse peak power can lead to transient electronic temperatures beyond the Curie temperature. This gives rise to a nonconservation of the amplitude of the magnetization. In addition, the effective field around which the magnetization precesses, if one considers anysotropy, is also time dependent.

A phenomenological approach based on the Bloch equations and on the two-temperature model has then been developed by our group [74]. It considers the temperature dependance of the magnetization modulus and the magneto-crystalline anisotropy, as follows.

$$|\overrightarrow{M}\,(T_e(t))\,| = M_S\sqrt{1 - \left(\frac{(T_e(t))}{T_c}\right)^2} \text{ for } T_e \simeq T_c \tag{1.47}$$

$$|\overrightarrow{M}| = 0 \text{ for } T_e > T_c, \tag{1.48}$$

where T_e is the electronic temperature and T_c is the Curie temperature. The time dependent behavior of T_e is given by the two-temperature model (presented in section 1.2.1) and the initial direction of the magnetization is obtained by minimizing the total static energy of the system. The time dependence of the magneto-crystalline anisotropy can be described by the constant K_l and comes from the temperature dependance of the magnetization [69]. Let us emphasize that the regime of precession and relaxation of the magnetization modulus occurs on a sufficiently long time (after the electron-phonon relaxation) so that one can assume $T_e \simeq T_s$.

1.2.3 Magneto-optical Kerr and Faraday effects

As already mentioned, the Kerr effect represents a dependence of the refractive index of the material due to the high intensity field. The refractive index is then given by the linear susceptibility tensor $\chi^{(1)}$ and the nonlinear susceptibility tensor $\chi^{(3)}$. This phenomenon induces the change of the polarization of a laser beam that is transmitted or reflected by the material.

The Faraday effect [2] is the analogous of the Kerr effect in the transmission configuration, being the Kerr obtained with the reflected light. The magneto-optical Kerr and Faraday effects have their origin in the spin-orbit and in the exchange interactions and happen when the material is exposed to an external static magnetic field. The time resolved study of these effects allows obtaining the dynamics of the magnetization.

One may consider the propagation of a wave in a ferromagnetic medium deduced from the Maxwell's equation. Being the film excited by a monochromatic wave $\overrightarrow{E}(\overrightarrow{r},\omega)$ with frequency ω, its equation of propagation is given by

$$\overrightarrow{\nabla} \wedge \overrightarrow{\nabla} \wedge \overrightarrow{E}(\overrightarrow{r},\omega) = -\omega^2 \mu_0 \left\{ \varepsilon_0 \overrightarrow{E}(\overrightarrow{r},\omega) + \overrightarrow{P}(\overrightarrow{r},\omega) + \frac{i}{\omega} \overrightarrow{\nabla} \wedge \overrightarrow{M}(\overrightarrow{r},\omega) \right\} \tag{1.49}$$

where $\overrightarrow{P}(\overrightarrow{r},\omega)$ and $\overrightarrow{M}(\overrightarrow{r},\omega)$ are the optical and magneto-optical polarizations, that can be separated into linear an nonlinear contributions as follows [10].

$$\overrightarrow{P}(\overrightarrow{r},\omega) = \overrightarrow{P}^{L}(\overrightarrow{r},\omega) + \overrightarrow{P}^{NL}(\overrightarrow{r},\omega) \tag{1.50}$$

$$\overrightarrow{M}(\overrightarrow{r},\omega) = \overrightarrow{M}^{L}(\overrightarrow{r},\omega) + \overrightarrow{M}^{NL}(\overrightarrow{r},\omega) \tag{1.51}$$

In the following, we consider only the linear effects with respect to the magnetic field. Considering that only the first and third order effects are non negligible, we have

$$P_i^1(\omega) = \sum_j \chi_{ij}^{(1)}(\omega) E_j(\omega) \tag{1.52}$$

$$P_i^3(\omega) = \sum_{jkl} \wp \chi_{ijkl}^{(3)}(\omega;\omega_j,\omega_k,\omega_l) E_j(\omega_j) E_k(\omega_k) E_l(\omega_l) \tag{1.53}$$

$$M_i^1(\omega) = \sum_{j\nu} \chi_{ij\nu}^{(1)MO}(\omega) E_j(\omega) H_\nu \tag{1.54}$$

$$M_i^3(\omega) = \sum_{jkl\nu} \wp \chi_{ijkl\nu}^{(3)MO}(\omega;\omega_j,\omega_k,\omega_l) E_j(\omega_j) E_k(\omega_k) E_l(\omega_l) H_\nu \tag{1.55}$$

where $\omega = \omega_1 + \omega_2 + \omega_3$, i, j, k, l are the x, y, z components of the electric field, ν are the components of the magnetic field and $\wp$ indicates the permutation of the fields.

In pump and probe experiments, the magnetization of the material is usually found by analyzing the polarization of the probe field. Using appropriate boundary conditions, it is possible to determine the changes of amplitude and phase of each component of the probe field $\overrightarrow{E_{Si}}(\omega)(i = x, y, z)$, transmitted or reflected by the sample.

In magnetic materials, the linear susceptibility tensor $\chi^{(1)}$ is at the origin of the linear magneto-optical Kerr and Faraday effects. The nonlinear suceptibility tensor $\chi^{(3)}$ is responsible for the nonlinear magneto-optical effects.

Linear dielectric tensor ε

The linear dielectric tensor is given as a function of the susceptibility tensor as follows.

$$\varepsilon_{ij}^{(1)MO} = 1 + \chi_{ij}^{(1)MO} \tag{1.56}$$

In a macroscopic approach, the linear dielectric tensor of a material is written as follows.

$$\varepsilon(\omega) = \begin{pmatrix} \varepsilon_{xx} & \varepsilon_{xy} & \varepsilon_{xz} \\ \varepsilon_{yx} & \varepsilon_{yy} & \varepsilon_{yz} \\ \varepsilon_{zx} & \varepsilon_{zy} & \varepsilon_{zz} \end{pmatrix} \tag{1.57}$$

If the medium is isotropic, only the diagonal elements are not zero. In the presence of a magnetic field, the nondiagonal parts of the dielectric tensor are different from zero.

The simplest description of the magneto-optical effects can be made via the Voigt model [75]. It allows to establish a relation between the magneto-optical quantities, such as the Kerr or Faraday rotation and ellipticity angles, and the optical and magnetic properties of the material. This model is an extension of the Drude model in the presence of a Lorentz force $-e(v \wedge \overrightarrow{B}_0 + \overrightarrow{E})$, being $\overrightarrow{B}_0$ an uniform magnetic field. The collective motion of the electrons is damped via the friction force $-m\gamma d\overrightarrow{r}/dt$. Solving the equation of motion of electrons for $\overrightarrow{B}_0$ applied in the z direction gives access to the nondiagonal terms of the dielectric tensor, as follows.

$$\varepsilon_{xy}(\omega) = \frac{\omega_p^2 \Omega \omega}{(\omega^2 + i\omega\gamma)^2 - \Omega^2\omega^2}, \tag{1.58}$$

where $\omega_p^2 = \frac{Ne^2}{m_e \varepsilon_0}$ is the plasma frequency and $\Omega = \frac{eB_0}{m_e}$ is the cyclotron resonance frequency, being m_e the electron mass.

Time evolution of the linear dielectric tensor ε

In the case of the polar Kerr effect (magnetization perpendicular to the film plane), the complex rotation of the polarization can then be written as a function of the Kerr rotation θ_K and Kerr elipticity η_K as follows [76].

$$\Phi_K = \theta_K - i\eta_K = \frac{-i\varepsilon_{xy}^{(1)MO}}{\left(\varepsilon_{xx}^{(1)MO} - 1\right)\sqrt{\varepsilon_{xx}^{(1)MO}}}, \tag{1.59}$$

Similarly, the Faraday rotation θ_F and Faraday elipticity η_F are given by

$$\Phi_F = \theta_F - i\eta_F = i\frac{\omega d}{2c}\frac{\varepsilon_{xy}^{(1)MO}}{\sqrt{\varepsilon_{xx}^{(1)MO}}}. \tag{1.60}$$

The measurement of the quantities θ_K, η_K, θ_F and η_F allows obtaining the elements of the linear magneto-optical dielectric tensor and, consequently, of the linear magneto-optical susceptibility tensor, for a complete description in terms of the linear magneto-optical polarization.

In this scope, the linear magneto-optical effect in a cubic magnetic medium in the polar configuration can be described by the first order dielectric tensor

$$\varepsilon^{(1)} = \tilde{\varepsilon}_{xx}\begin{pmatrix} 1 & i\tilde{Q} & 0 \\ -i\tilde{Q} & 1 & 0 \\ 0 & 0 & 1 \end{pmatrix}, \tag{1.61}$$

where $\tilde{\varepsilon}_{xx} = \varepsilon_{xx}\prime + i\varepsilon_{xx}\prime\prime$ is the dielectric function and $\tilde{Q} = -i\tilde{\varepsilon}_{xy}/\tilde{\varepsilon}_{xx} = q\prime + iq\prime\prime$ is proportional to the ratio of the nondiagonal and the diagonal terms of $\varepsilon^{(1)}$. As shown before in this section, Φ_F and Φ_K also depend on $\varepsilon^{(1)}$; so do the transmission and the reflection.

In the experiments performed in reference [42], the time evolution of the complex time-dependent nondiagonal tensor elements $\Delta\tilde{\varepsilon}_{xy}\prime/\tilde{\varepsilon}_{xy}\prime$ and $\Delta\tilde{\varepsilon}_{xy}\prime\prime/\tilde{\varepsilon}_{xy}\prime\prime$ was extracted from the Faraday rotation and ellipticity, while the time evolution of the complex time-dependent diagonal tensor elements $\Delta\tilde{\varepsilon}_{xx}\prime/\tilde{\varepsilon}_{xx}\prime$ and $\Delta\tilde{\varepsilon}_{xx}\prime\prime/\tilde{\varepsilon}_{xx}\prime\prime$ was obtained from the dynamics of the reflectivity and transmission (being the linear magneto-optical response usually described by $\tilde{\varepsilon}_{xy} = \tilde{\alpha}M$).

These four quantitites allow retrieving the real and imaginary parts of $\tilde{Q}$ ($\Delta q_{xy}\prime/q_{xy}\prime$ and $\Delta q_{xy}\prime\prime/q_{xy}\prime\prime$).

Time-resolved Faraday effect

To understand the evolution of the optical and magneto-optical polarization, one may consider a ferromagnetic thin film in a static magnetic field H_0 perpendicular to the film. This last one is excited by a circularly polarized pump pulse $\overrightarrow{E}_p(t)e^{i\omega t}$ and investigated by a linearly polarized probe pulse $\overrightarrow{E}_s(t-\tau)e^{i\omega(t-\tau)}$, delayed by τ. In the limit of the delta function, the optical and magneto-optical polarizations are given by

$$\overrightarrow{P}(\overrightarrow{r},t-\tau) = R^{(1)}(\overrightarrow{r},t) \otimes \overrightarrow{E}_s + R^{(3)}(\overrightarrow{r},t) \otimes \overrightarrow{E}_s \overrightarrow{E}_p^* \overrightarrow{E}_s \text{ and} \tag{1.62}$$

$$\overrightarrow{M}(\overrightarrow{r},t-\tau) = R^{(1)MO}(\overrightarrow{r},t) \otimes \overrightarrow{E}_s \overrightarrow{H_0} + R^{(3)MO}(\overrightarrow{r},t) \otimes \overrightarrow{E}_s \overrightarrow{E}_p^* \overrightarrow{E}_s \overrightarrow{H_0}, \tag{1.63}$$

where R and R^{MO} are the optical and magneto-optical tensors.

In the Faraday configuration, the probe pulse experiences a rotation $\theta_F(\tau)$ and an ellipticity $\eta_F(\tau)$ given by

$$\theta_F(\tau) = \theta_F^{(1)MO} + \theta_F^{(3)}(\tau) + \theta_F^{(3)MO}(\tau) \tag{1.64}$$

$$\eta_F(\tau) = \eta_F^{(1)MO} + \eta_F^{(3)}(\tau) + \eta_F^{(3)MO}(\tau) \tag{1.65}$$

where $\theta_F^{(1)MO}$ and $\eta_F^{(1)MO}$ are the static linear rotation and ellipticity of the probe beam associated to the magnetization, $\theta_F^{(3)}(\tau)$ and $\eta_F^{(3)}(\tau)$ are the optical rotation and ellipticity induced by the pump and $\theta_F^{(3)MO}(\tau)$ and $\eta_F^{(3)MO}(\tau)$ are the dynamical magneto-optical rotation and ellipticity induced by the pump beam. These two last terms contain the information about the magnetization dynamics and can not be analyzed only in terms of pure magnetic effects. The corresponding time dependant nonlinear response $R^{(3)MO}$ contains the dynamics of the charges and spins populations and all the incoherent processes like the thermalization of electron, the electron-phonon relaxation and the heat diffusion.

1.2.4 Magneto-optical four-wave mixing

The experimental configuration and the description of the FWM in a two-level system have been presented in section 1.1.4. The MO-FWM configuration is an extension of the

FWM where an external magnetic field is used for revealing the spins dynamics. The basic concept is that the measurement of the FWM emission when the material is under an external field (perpendicular to the sample plane) reveals optical and magneto-optical components, as discussed before for the Faraday effect. If one measures the emission for the two directions of the external field, it is possible, by differenciation, to isolate the pure magneto-optical signal.

As seen previously for the FWM configuration, one must consider two relaxation times when analysing the response of a medium after a laser pulse excitation: the populations relaxation time T_1, responsible for describing the relaxation of the excited states in this medium, and the coherences relaxation time T_2, responsible for describing the loss of quantum coherence of these levels. Generally speaking, in metals they involve electron-electron elastic scattering that lead to a redistribution of electrons in k-space.

The two-beam FWM configuration has been used in the study of semiconductors to investigate the third order nonlinear susceptibility [77] and the dephasing time T_2 [78]. The spin coherence of excitons can also be measured with the three-beam FWM configuration [79].

The response of the medium studied with the MO-FWM can be purely optical or magneto-optical, so it is intuitive to think about two types of coherences relaxation times. The T_{2e}, called electronic coherence time, considers only the Coulomb interaction. It describes the electrons dynamics and can be measured in the presence or not of an external magnetic field. The T_{2em}, called electromagnetic coherence time, comes from the spin-orbit interactions and gives access to the spins dynamics. It requires the presence of an external magnetic field. Both of them can be obtained from a MO-FWM configuration and comparing them is one of the goals of this thesis.

1.3 Propagation effects

1.3.1 Group velocity dispersion

A large spectrum pulse propagating in a medium suffers a phase distortion and consequently an increase of the pulse duration because the frequencies do not see the same refractive index (it increases when the wavelength decreases, for a normal dispersive medium). The frequency spectrum does not change but the spectral components suffer a temporal drift. This phenomenon is called group velocity dispersion and is responsible for making the pulse longer.

A description of a gaussian pulse, with duration $\Delta\tau$ centered at ω_0 can be made as follows.

$$E(t) = A_t exp\left[-\frac{ln2}{2}\left(\frac{2t}{\Delta t}\right)^2\right] exp\left\{-i\left[\omega_0 t - \theta(t)\right]\right\}, \tag{1.66}$$

where A_t is the amplitude of the pulse and $\theta(t)$ determines the temporal relationship among the frequency components contained in the bandwidth of the pulse.

To determine the duration of a pulse after propagating through a dispersive material in the time domain, it is necessary to solve a convolution integral, very often, numerically. In the frequency domain, the convolution becomes a product. The Fourier transform to the frequency domain of the field $E(t)$ gives

$$E(\omega) = A_\omega exp\left\{-\frac{ln2}{2}\left[\frac{2(\omega-\omega_0)}{\Delta\omega}\right]^2\right\} exp\left[-i\phi_{pulse}\left(\omega-\omega_0\right)\right], \tag{1.67}$$

where A_ω is the amplitude of the pulse and $\phi(\omega)$ is the spectral phase, that has the same function of $\theta(t)$, but in the spectral domain.

The propagation through the material adds a spectral phase $\phi(\omega) = k(\omega)x$ to the pulse, being $k(\omega)$ the propagation constant and x the length of the medium. It is common to express the spectral phase using a Taylor expansion around the carrier frequency of the pulse as follows.

$$\phi(\omega) = \phi(\omega_0) + \frac{d\phi}{d\omega}(\omega_0)(\omega-\omega_0) + \frac{1}{2}\frac{d^2\phi}{d\omega^2}(\omega_0)(\omega-\omega_0)^2 + \frac{1}{6}\frac{d^3\phi}{d\omega^3}(\omega_0)(\omega-\omega_0)^3 + ... \tag{1.68}$$

Knowing that $v_g = d\omega/dk$ is the group velocity and that the group delay is given by the derivative of the phase with respect to ω, the first term adds a constant to the phase and the second one, proportional to $1/v_g$ adds a delay to the pulse. These terms do not affect the pulse shape. The third term is named group delay dispersion (GDD) and is proportional to $\frac{d}{d\omega}\left(\frac{1}{v_g}\right)$. It is responsible for introducing the frequency dependent delay of the different spectral components of the pulse and if considered per unit length, gives rise to the group velocity dispersion (GVD). The fourth term is called third order dispersion and applies a quadratic phase to the pulse.

Stopping the series expansion in the third term and considering an output beam being described by

$$E_{out}(\omega) = E_{in}(\omega)R(\omega)exp\left[-i\phi_{material}(\omega-\omega_0)\right], \tag{1.69}$$

where $R(\omega)$ is an amplitude scalling factor which for a linear transparent medium can be approximated by 1 and $\phi_{material}(\omega - \omega_0)$ is the spectral phase added by the material, one can then write

$$E_{out}(\omega) = A_\omega exp\left\{-\frac{ln2}{2}\left[\frac{2(\omega-\omega_0}{\Delta\omega}\right]^2\right\} exp\left[-i(\phi_{2,pulse}+\phi_{2,material})\frac{(\omega-\omega_0)^2}{2}\right]. \quad (1.70)$$

The transformation back to the time domain gives

$$E_{out}(\omega) = A'_t exp\left\{\frac{4(ln2)t^2}{2[\Delta t^2 + i4(ln2)\phi_2]}\right\} \quad (1.71)$$

where ϕ_2 is the sum of the group delay dispersion of the material and the group delay of the pulse. To obtain the output pulse duration Δt_{out}, one must consider the intensity $I_{out}(t)$, by squaring the eletric field in equation 1.71. With that, one obtains

$$\Delta t_{out} = \frac{\sqrt{\Delta t^4 + 16(ln2)^2\phi_2^2}}{\Delta t}. \quad (1.72)$$

Replacing Δt with the spectral bandwidth so the group delay dispersion can be expressed in terms of observable quantities, the group delay dispersion can be written as

$$\phi_2 = \frac{1}{4ln2}\sqrt{\left(\frac{c_B\Delta t_{out}\lambda^2}{c\Delta\lambda}\right)^2 - \left(\frac{c_B\lambda^2}{c\Delta\lambda}\right)^4}, \quad (1.73)$$

where c_B is a function of the pulse profile. This is the method to calculate the dispersion introduced by a material through which a gaussian pulse propagates.

Effects like the group delay dispersion and the self-phase modulation co-exist in the laser systems.

1.3.1.1 Effects of dispersion on temporal field and phase profiles

To show that the spectral phase plays an important role when obtaining the temporal intensity (and consequently, the temporal width and pulse duration) and the temporal phase, we have simulated the field temporal profile $E(t)$ and the phase temporal profile $\phi(t)$ considering $\phi(\omega)$. This work was led by this thesis director, Dr. Jean-Yves Bigot.

With the spectral intensity $S(\omega) = |\tilde{E}(\omega)|^2$ ($\tilde{E}(\omega) = \sqrt{S(\omega)}e^{i\phi(\omega)}$) it is possible to obtain the temporal intensity $S(t) = |E(t)|^2$ ($\tilde{E}(t) = \sqrt{S(t)}e^{i\phi(t)}$) via the Fourier transform, defined as follows.

$$S(t) = \frac{1}{\sqrt{2\pi}} \int_{-\infty}^{+\infty} S(\omega) e^{i\omega t} d\omega \tag{1.74}$$

The spectral intensity profile considered in these simulation was measured at the output of the Rainbow oscillator (to be presented in section 3.5.3), used in the measurements of the few-cycle two-beam MO-FWM configuration and is shown in figure 1.4.

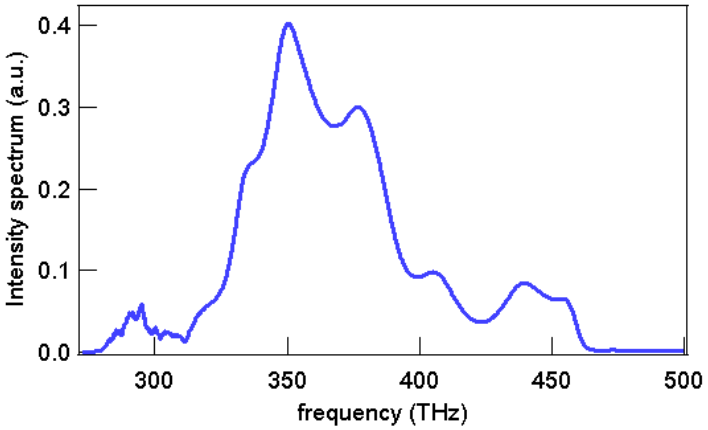

Figure 1.4: Spectral intensity of the Rainbow oscillator used in the simulations.

In the simulations, we have considered different spectral phases, composed by second and third order chirp, to feed the Fourier transforms allowing to obtain $E(t)$ and $\phi(t)$. The spectral phase profile equation and the obtained temporal field and phase profiles are shown in the figures 1.5 and 1.6.

With that, we show that the effect of the second and third order components of the spectral phase can play an important role on the pulse duration that can be obtained with the same spectral intensity.

Considering zero spectral phase allows obtaining the transform limited pulse for this spectrum, as if the pulse was perfectly compensated, and its temporal phase, as shown in figure 1.7.

Figure 1.7 shows that even when the spectral phase is zero, the temporal phase is different from zero. It also sets a limit in the pulse duration that can be obtained around $\sim 7,3fs$ for this spectral intensity. In addition, in the time interval where the temporal profile exists, the temporal phase is linear.

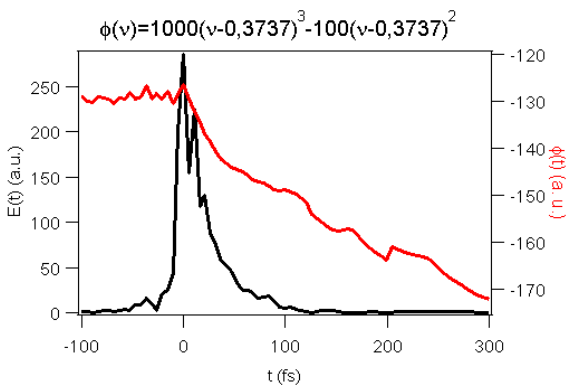

Figure 1.5: Temporal profile $E(t)$ and temporal phase $\phi(t)$ retrieved from the spectral intensity $S(\omega)$ shown in figure 1.4 considering second and third order chirp (spectral phase given by $\phi(\nu) = 1000(\nu - 0,3737)^3 - 100(\nu - 0,3737)^2$. The FWHM is $\sim 32fs$.

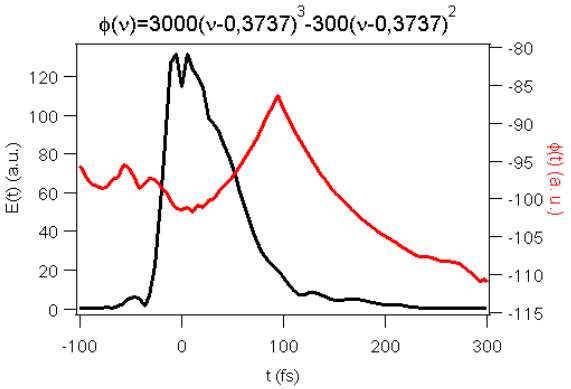

Figure 1.6: Temporal profile $E(t)$ and temporal phase $\phi(t)$ retrieved from the spectral intensity $S(\omega)$ shown in figure 1.4 considering second and third order chirp (spectral phase given by $\phi(\nu) = 3000(\nu - 0,3737)^3 - 300(\nu - 0,3737)^2$. The FWHM is $\sim 80fs$.

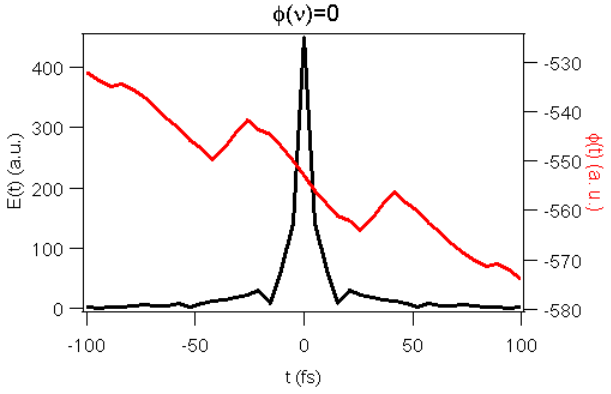

Figure 1.7: Temporal profile $E(t)$ and temporal phase $\phi(t)$ retrieved from the spectral intensity $S(\omega)$ shown in figure 1.4 considering no spectral phase. The FWHM is $\sim 10,4fs$.

1.3.2 Magneto-optical four-wave mixing signals with no phase effect - convolution

The time-resolved FWM and MO-FWM signals can be studied by the simple approach of a convolution of the Gaussian pulse of duration d and spectral phase equal to zero, represented by $G(t)$, and the exponential decay characteristic of the inhomogeneous broadening, presented in section 1.1.4, represented here by the product between the Heaviside function and an exponential ($H(t)exp(-4t/T_2)$), as follows.

$$f(t) = \int_{-\infty}^{\infty} B(t')G(t-t')dt' = \int_{-\infty}^{\infty} H(t')e^{-\frac{4t'}{T_2}} e^{-\frac{(t-t')^2}{d^2}} dt' \tag{1.75}$$

This convolution leads to the product of an exponential and the complementary error function.

$$f(t) = \frac{2d}{\sqrt{2}} exp\left[-\frac{4}{T_2}\left(t - \frac{d^2}{T_2}\right)\right] erfc\left[-\frac{1}{d}\left(t - \frac{2d^2}{T_2}\right)\right] \tag{1.76}$$

With this equation, it is possible to study the evolution of the expected signals in time as a function of the pulse duration d and as a function of the dephasing time T_2. We remind here that this analysis is not particularly restricted to the study of spins dynamics. It will be helpfull when analysing the dynamics of the MO-FWM signals in the transparency spectral region of the garnet films.

Fixing a pulse duration and varying the time T_2, gives the curves shown in figure 1.8 for positive times.

The effect of a longer T_2 in this case of a fixed pulse duration is shown in the exponential decay in positive times. The decay is more visible for higher T_2 and the center of the curve evolves with T_2 as well.

Analysing the same situation but now with a $10fs$ pulse allows one to see that the gaussian pulse dominates the response. A simulation of different T_2 for $d = 10fs$ can be seen in figure 1.9.

Fixing the coherence time and varying the pulse duration, as done in figure 1.10 in logarithmic scale for $T_2 = 2fs$, allows seeing the dependance with the pulse duration.

The logarithmic scale makes it is possible to see that the longer the pulse duration, the less visible the exponential decay is on the positive times.

To better see this dependence, one can look at the delay of the maximum of the signal as a function of T_2 and d. Figure 1.11 shows the dependance of the position of the signals centers as a function of the pulse duration for different dephasing times.

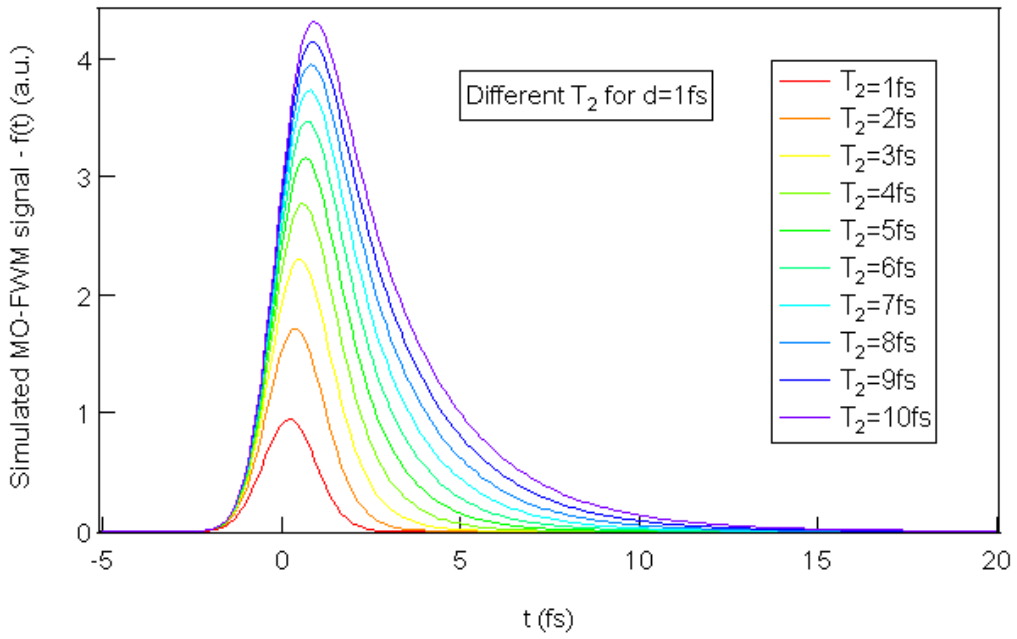

Figure 1.8: Simulation of the results of equation 1.76 for $d = 1fs$ and $1fs \leq T_2 \leq 10fs$. The coherence time T_2 shifts the center of the signals and changes its decay.

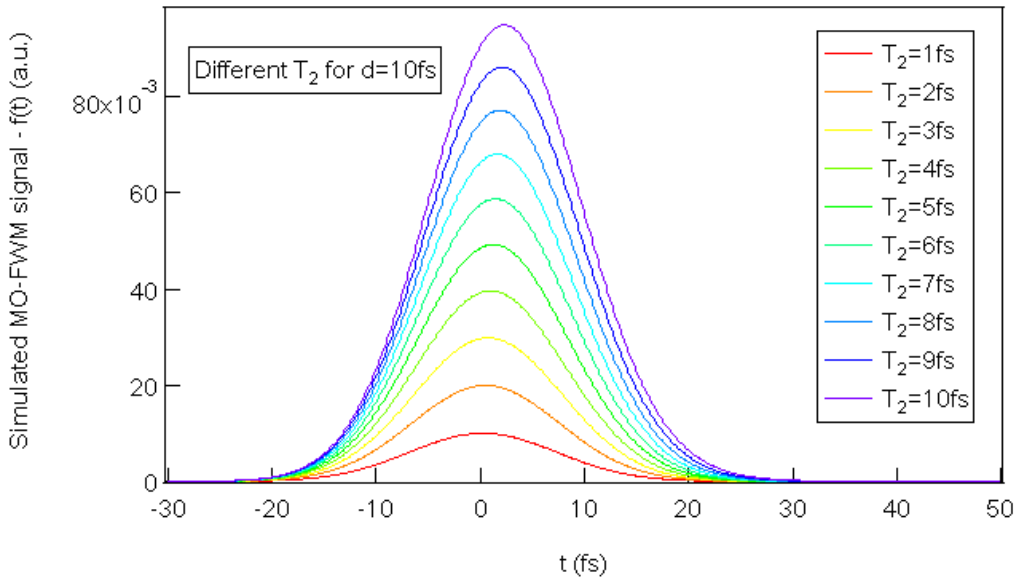

Figure 1.9: Simulation of the results of equation 1.76 for $d = 10fs$ and $1fs \leq T_2 \leq 10fs$. The long pulse duration (compared to the coherence time) dominates the response.

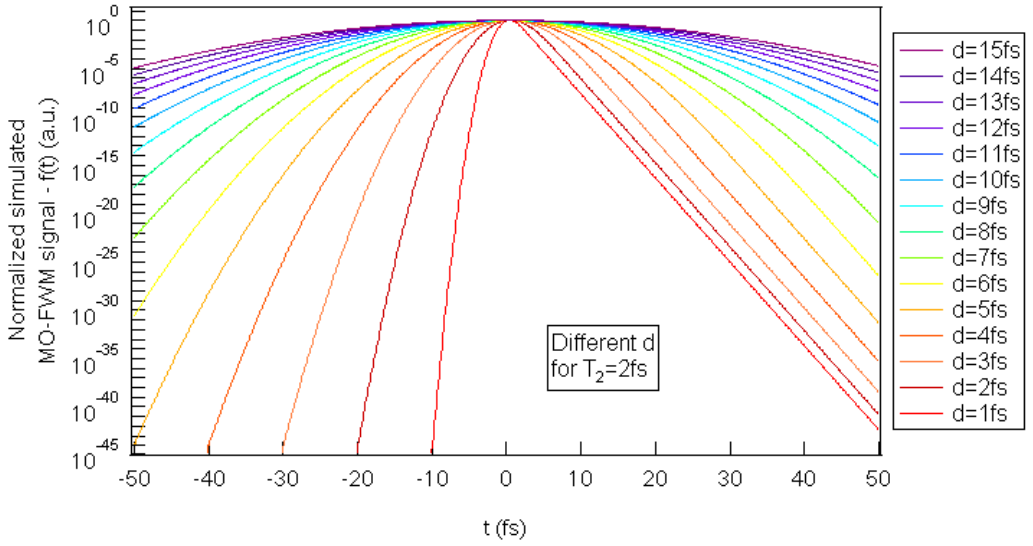

Figure 1.10: Simulation of the results of equation 1.76 for $T_2 = 2fs$ and $1fs \leq d \leq 15fs$. Long pulse durations do not allow to solve the coherence time.

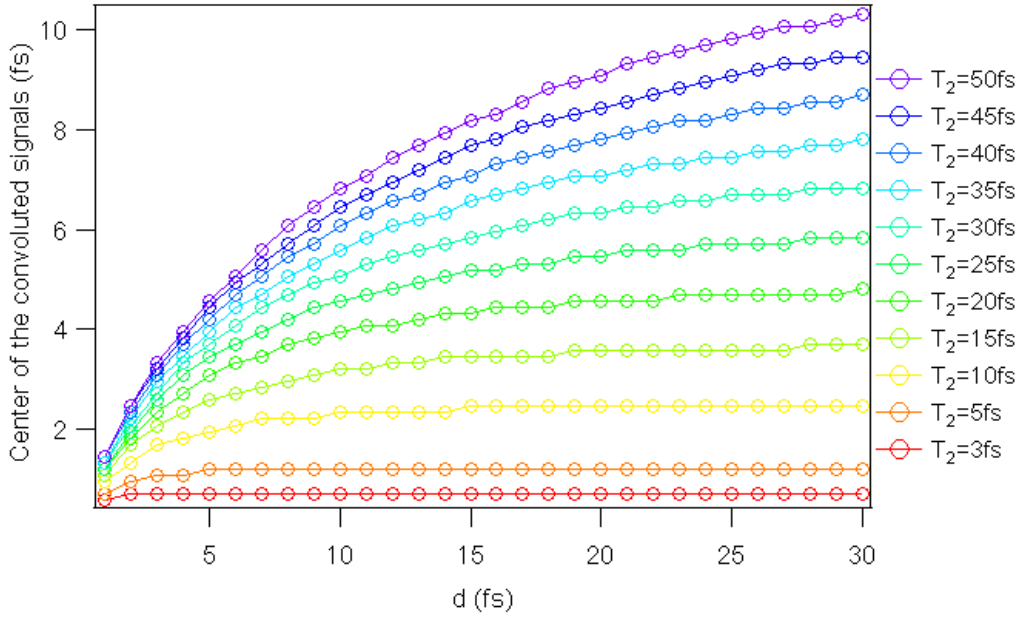

Figure 1.11: Delay of the center of the simulated results of equation 1.76 as a function of d for $1fs \leq d \leq 30fs$ and $T_2 = 3$, 5, 10, 15, 20, 25, 30, 35, 40, 45 and $50fs$.

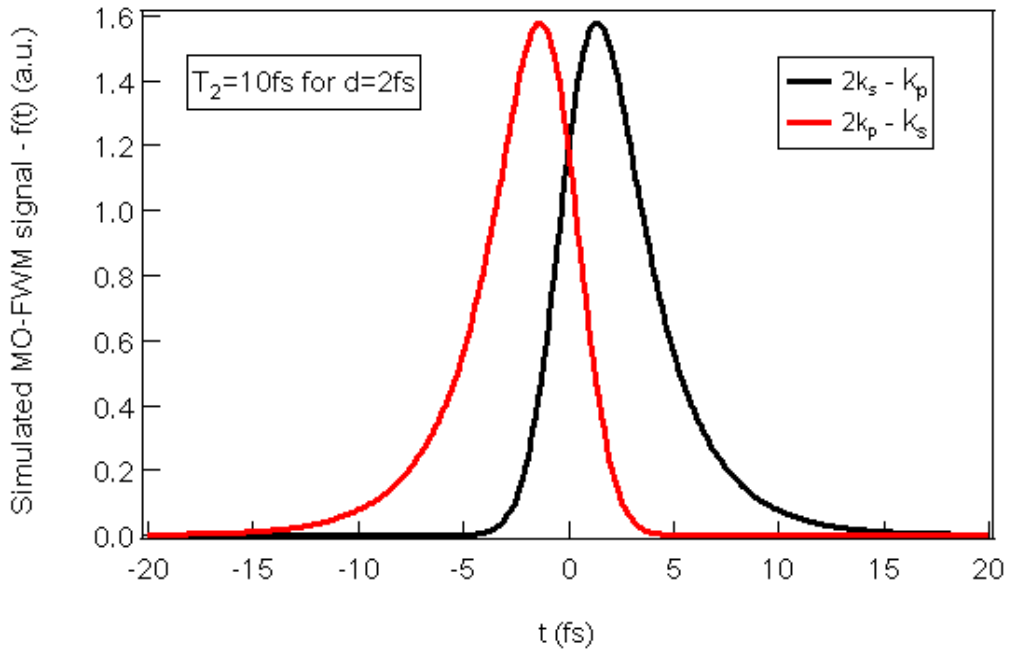

Figure 1.12: Simulation of the results of equation 1.76 for $d = 2fs$ and $T_2 = 10fs$

Figure 1.11 makes clear that measuring the same T_2 with different pulse durations results in different shifts of the center of the signal. For very short T_2, measurements with pulses of different durations will provide the same delay. However, for T_2 sufficiently long compared to d, one can solve T_2.

As to be shown later in chapter 4, in our experiment, one must also look at the results obtained from equation 1.76 with a reversed time axis, because the MO-FWM signals are symmetric in time for the two directions $2\vec{k}_p - \vec{k}_s$ and $2\vec{k}_s - \vec{k}_p$. For a given pulse duration and a given dephasing time, the signals expected for both directions of the MO-FWM can be simulated.

With a sufficiently short pulse duration measuring a relatively long dephasing time, it is possible to well see the asymmetry caused by the exponential decays in both directions of time, as shown in figure 1.12. This asymmetry shows that the pulse duration solves the dephasing time. The more asymmetric the curves are, the shorter the pulse duration is when compared to T_2.

1.3.3 Magneto-optical four-wave mixing signals with spectral phase different from zero - two-level system

We have shown in the previous section the influence of the duration of a gaussian transform limited pulse and the influence of the coherence time T_2 in the expected MO-FWM signal, interpreted as a convolution of a the gaussian pulse and an exponential decay. However, sub-$10fs$ pulses are generated through nonlinear processes that often affects the spectral phase. Here we present the influence of the pulse chirp on the temporal shape and on the resulting FWM dynamical signal. The model used is based on a two-level system with homogeneous broadening and on the pulses used in the few-cycle two-beam MO-FWM configuration, that will be more explored in section 3.5.3.

Let us emphasize that for a material with a large number of transitions, as it is the case for garnets, one should consider the specific levels structure. Such considerations do not alter the present description since the experimens are performed at $800nm$, i.e. far from resonance (clearly apparent in the non resonant magneto-optical response shown in figure 3.5, to be more explored in section 3.1.4).Therefore, we can always assume an effective T_2 time that characterizes all resonant levels.

In a first part of the analysis, we have used the spectrum measured at the output of the Rainbow oscillator, already shown in section 1.3.1.1 in figure 1.4, and the spectral phase from reference [80], measured in a system similar to ours. This phase was recoverered from fundamental modulation frequency-resolved optical gating traces(FM-FROG), to be more explored in section 3.4. The FM-FROG consists on the phase retrieval based on the modulation at the fundamental frequency. Figure 1.13 shows the spectral and the temporal phases used in the simulations.

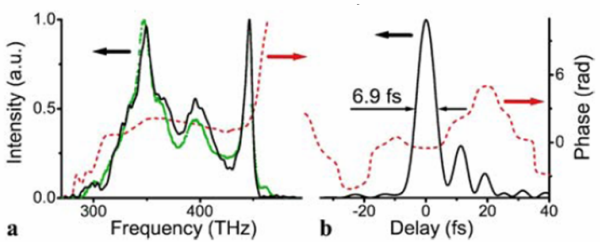

Figure 1.13: FM-FROG routine results from reference [80]. *a*) retrieved spectral intensity (black solid line) and spectral phase (dashed line) and measured spectrum (green data points). *b*) retrieved temporal pulse profile (solid line) and temporal phase (dashed line).

With the spectral intensity $S(\omega)$ measured and the spectral phase $\phi(\omega)$ from figure 1.13, it is possible to obtain the temporal phase $\phi(t)$, shown in figure 1.14.

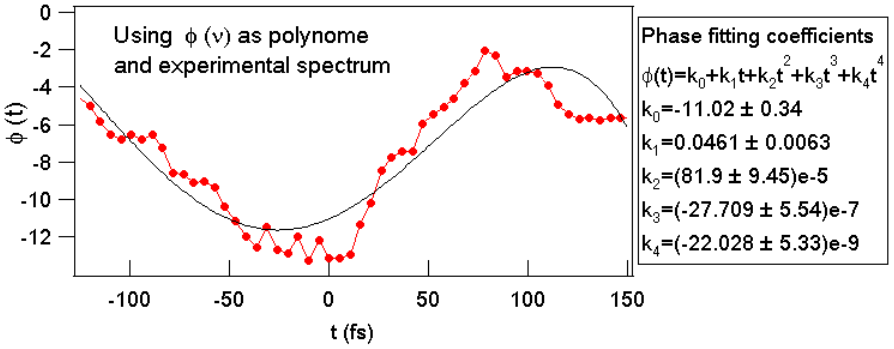

Figure 1.14: Temporal phase $\phi(t)$ retrieved from the spectral intensity $S(\omega)$ shown in figure 1.4 considering the spectral phase $\phi(\omega)$ shown in figure 1.13 and its polynomial fit.

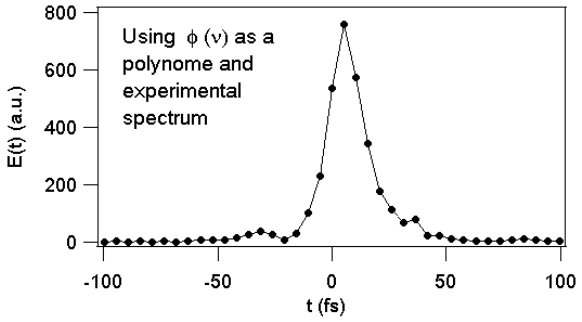

Figure 1.15: Field temporal profile $E(t)$ retrieved from the spectral intensity $S(\omega)$ shown in figure 1.4 considering the spectral phase $\phi(\omega)$ shown in figure 1.13 using the Hanning function. The temporal width is $\sim 21fs$.

The polynomial fit shown in figure 1.14 reveals second and third order dispersion mixed in the temporal phase.

Using the Hanning function to cut the extreme parts of the spectrum shown in figure 1.4 (given by $f(n) = \sum_p \frac{1}{2}\left[1 - cos\left(\frac{2n}{N-1}\right)\right]$) and considering the phase in figure 1.13, we obtained the temporal pulse profile shown in figure 1.15.

It is important to define the width of the temporal and spectral profiles, Δt and $\Delta\omega$, as their full width at half maximum (FWHM) and not their bandwidths $\sigma_\omega = \sqrt{\langle\omega^2\rangle - \langle\omega\rangle^2}$ and $\sigma_t = \sqrt{\langle t^2\rangle - \langle t\rangle^2}$, respectively, being $\sigma_\omega\sigma_t \geq \frac{1}{2}$ (equal for gaussian pulses) while $\Delta t\Delta\omega = 8ln2$. However, Δt does not represent the pulse duration in intensity, as it is a result of the spectral profile of the field. To obtain the real pulse duration in intensity one must divide Δt by $\sqrt{2}$.

One of the goals of these simulations on the phase is to check the behavior of the MO-FWM signal generated with pulses with phase different from zero. For that we have

considered the density matrix formalism for a two-level system. As mentioned in section 1.1.4 in the case of an excitation by $\delta-$function pulses, the homogeneous broadening gives rise to a signal that decays exponentially with $T_2/2$ and the inhomogeneous broadening gives rise to a signal that decays exponentially with $T_2/4$.

If one considers an hyperbolic secant pulse with temporal phase zero and duration of $2fs$, it is possible to simulate the FWM signal in the case of the homogeneous broadening for different coherence times, as shown in figure 1.16.

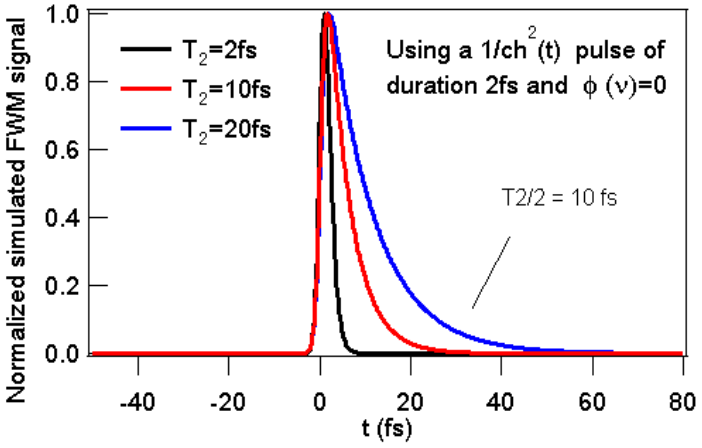

Figure 1.16: Simulated FWM signals obtained considering a two-level system, hyperbolic secant pulses of $2fs$ of duration with zero temporal phase and homogeneous broadening. Signals are presented for $T_2 = 2,\ 10$ and $20fs$.

The curves in figure 1.16 confirm the results shown in section 1.3.2 (where gaussian pulses and the inhomogeneous broadening were considered). The longer the considered coherence time is, the more important are the exponential decay and the shift of the center of the signal, parameter of interest for allowing to estimate T_2. This evolution can be seen in figure 1.21, to be presented ahead.

For the same coherence time T_2, we can measure different shifts of the center of the signal with respect to the zero delay for different pulse durations, what confirms that one must consider the pulse duration when estimating T_2 from the temporal shift of the signals of FWM emitted in the two directions in the two-beam configuration.

We have also simulated the same signals using the experimental pulses, which means we have considered the spectrum used in the measurements presented in section 4.2.1 shown in figure 1.4 (with zero spectral phase). These results are shown in figures 1.17 and 1.18.

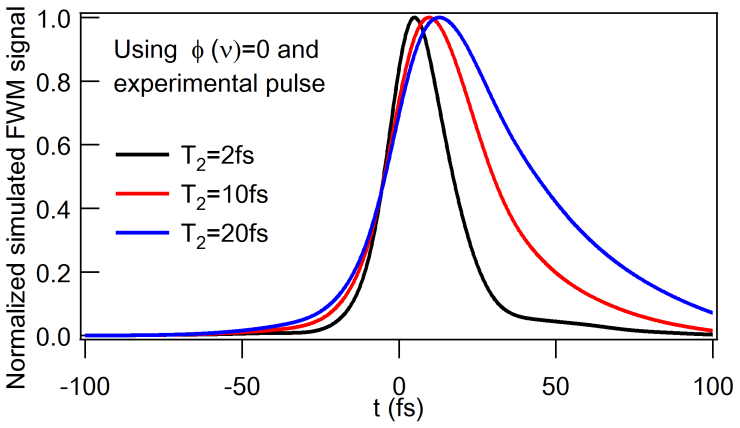

Figure 1.17: Simulated FWM signals obtained considering a two-level system, the experimental pulses with zero spectral phase and homogeneous broadening. Signals are presented for $T_2 = 2,\ 10$ and $20fs$.

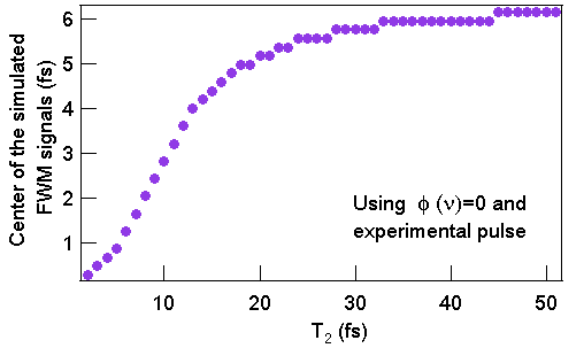

Figure 1.18: Center of the simulated FWM signals obtained considering a two-level system, the experimental pulses with zero spectral phase and homogeneous broadening as a funtion of T_2.

Once again it is possible to see in figure 1.17 that the coherence time is responsible for shifting the zero of the FWM signal even if no spectral chirp is considered. The evolution of the center of the FWM signal is shown in figure 1.18.

When second and third order spectral chirp are considered (the spectral phase being $\phi(\nu) = 10^3(\nu - 0,3737)^3 - 10^2(\nu - 0,3737)^2$) the FWM signal behavior changes. Figure 1.19 shows the temporal phase and the temporal profile used to simulate the signals shown in figure 1.20.

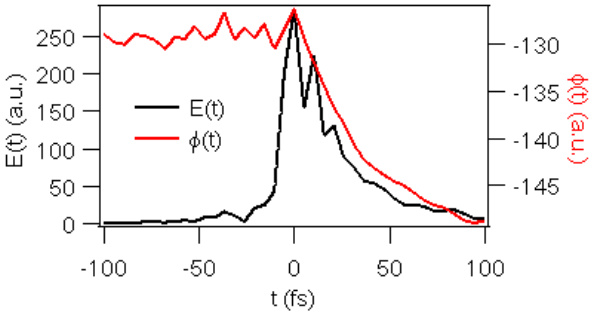

Figure 1.19: Temporal phase and temporal profile obtained from the experimental pulse (spectrum shown in figure 1.4) used in the simulations considering second and third order chirp.

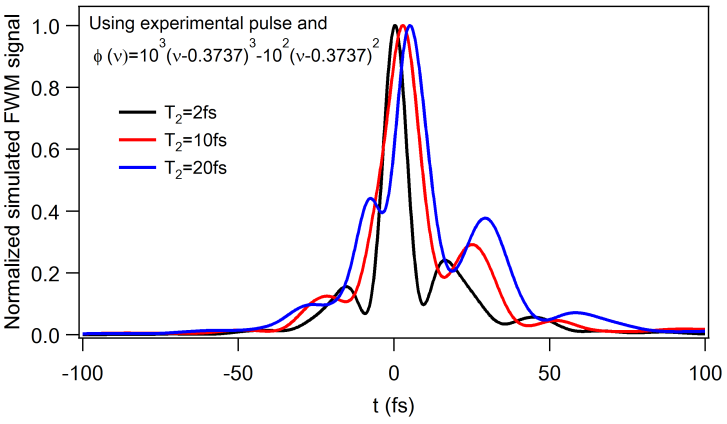

Figure 1.20: Simulated FWM signals obtained considering a two-level system, the experimental pulses with second and third order spectral chirp and homogeneous broadening for $T_2 = 2$, 10 and $20fs$.

An important spectral chirp is responsible for creating oscillations in the FWM signal, that change with the coherence time T_2. The centers follow the behavior shown before (more shifted for more important T_2) but do not seem to have the same evolution as the one presented in figure 1.17 where no phase is considered.

To well understand how this behavior influences the estimation of the coherence time, we show here the maximum of the FWM signals, which means, its center, as a function of T_2 for the different methods considered so far: FWM in a two-level system considering hyperbolic secant pulses with no spectral phase and with spectral phase different from zero, FWM in a two-level system considering the experimental pulses with no spectral phase and with spectral phase different from zero and the convolution of a gaussian pulse

with an exponential, as shown in section 1.3.2, considering in this case the inhomogeneous broadening. The curves are shown in figure 1.21.

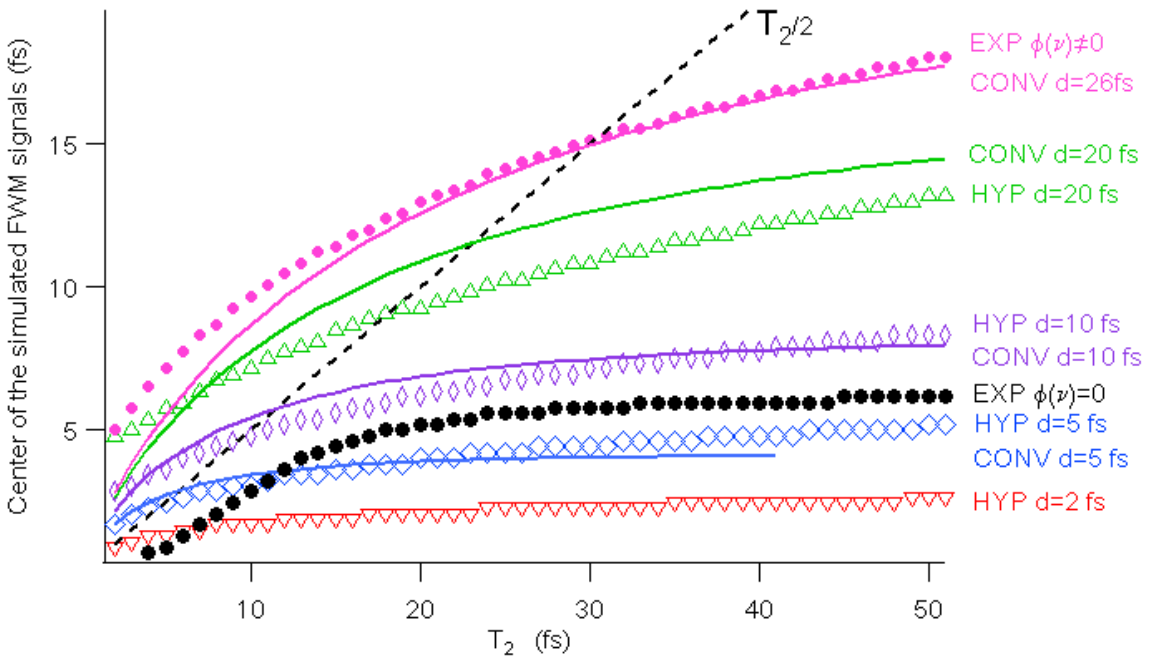

Figure 1.21: Center of the simulated FWM signals as a function of the coherence time for the different methods considered. Lines represent the center of the curve given by the convolution of a gaussian pulse and an exponential for diferent pulse durations d and are named $CONV$. Filled circles represent the center of the FWM signals simulated using the experimental pulse with spectral phases $\phi(\nu) = 0$ and $\phi(\nu) = 10^3(\nu - 0,3737)^3 - 10^2(\nu - 0,3737)^2$ and are named EXP. Empty circles represent the the center of the FWM signals simulated using an hyperbolic secant pulse and $\phi(\nu) = 0$ and are named HYP.

Figure 1.21 shows that, for the same coherence time T_2, one can obtain different shifts between the maximum of the FWM signal and the zero (and, consequently, between the maximum of the FWM signals generated in the two complementary directions described in section 1.1.4). The shift between the centers always allows estimating the coherence time, however, one must be very attentive to the type of pulse and phase used. The curves in black and in pink show clearly that the same spectrum with no spectral phase and with an important second and third order chirp can provide very different shifts of the maximum of the FWM signal. It is important then to well know the phase of the pulse so the estimation is trustful.

It is important to remind here that these simulations were done considering no magnetic effect and that one can extend this analysis to the magneto-optical case, being the conclusions on the behavior of the shift similar.

1.3.4 Estimation of the phase of the experimental pulse - interferometric autocorrelation

As shown in the previous section, a characterization of the spectral phase of the pulse used to measure the temporal shift between the signals emitted in the two directions of the MO-FWM is fundamental to well estimate the coherence time.

The pulse used in these measurements was characterized using an interferometric autocorrelator (IAC, to be more explored in section 3.4). We have then used the spectrum of these pulses, shown in figure 1.4, to simulated an IAC trace with different phases. The results are shown in figures 1.22 and 1.23.

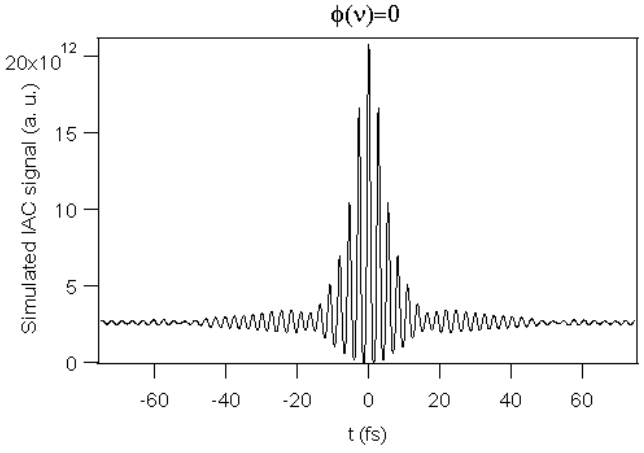

Figure 1.22: Simulated IAC trace obtained using the experimental spectrum from figure 1.4 considering no spectral phase.

One can see that an important spectral phase is responsible for increasing the side wings (second order chirp) and for making the offset not constant (third order chirp).

Figure 1.24 shows the experimental IAC trace and the simulated IAC considering no spectral phase for comparison.

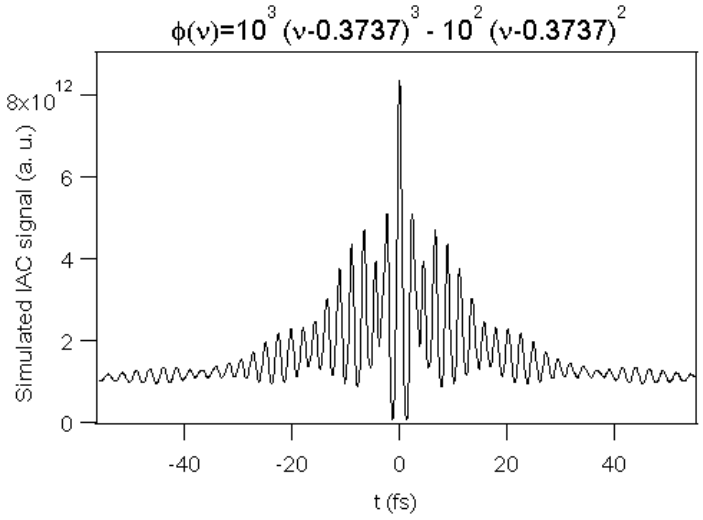

Figure 1.23: Simulated IAC trace obtained using the experimental spectrum from figure 1.4 considering second and third order chirp.

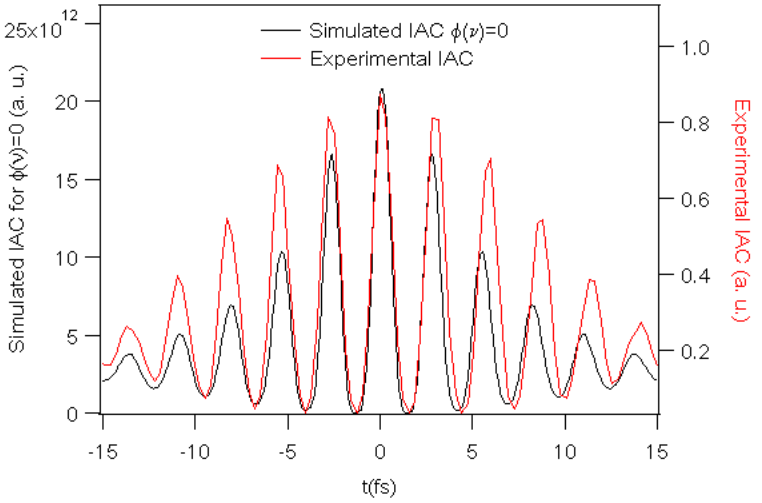

Figure 1.24: Simulated IAC trace obtained using the experimental spectrum from figure 1.4 considering no spectral phase and the experimental IAC trace.

The simulated and experimental traces present similarities what leads to the conclusion that their phases must be close. From this analysis, we can say that the spectral phase of the pulse used in the two-beam configuration MO-FWM measurements is comparable to zero, not being then important for the estimations of the coherence time.

1.4 Conclusions

In this chapter, we have presented the important nonlinear optical and magneto-optical effects that will be the basis of the study of the coherent magneto-optical response of a garnet film. We have presented the second harmonic generation, that will serve as a basis for the ultrashort pulse characterization of the experimental pulse, the Kerr and Faraday effects in the optical and magneto-optical cases and the FWM in the optical and magneto-optical configurations as well. We have shown the directions of emission of the FWM as well as the notion of populations time T_1 and coherent relaxation time T_2 that are considered in the description of the dynamics of one electron in a two-level system.

We have described the electrons and spins dynamics via the two and the three-temperature model, respectively, and we have shown how the precession of the magnetization allows studying the spins population dynamics. We aim at studying the coherent contribution to this dynamics by using the MO-FWM configuration.

As this coherent contribution is expected to be in the sub-$10fs$ range, we have shown that the ultrashort pulse spectral phase can play an important role in the generation of the MO-FWM signals. The same coherence time can give rise to different shifts between the signals emitted in the two directions of the FWM when pulses with different spectral phases are used.

The simulated FWM signals were obtained considering a simplified approach of a two-level system with homogeneous broadening with dipolar interaction and no magnetic effect. The next chapter will be then dedicated to a formal description of the magneto-optical response via an eight-level system model.

Chapter 2

Modelling the time resolved magneto-optical response with the spin-orbit interaction: preceeding studies

This chapter presents the basis and the development of a model to describe the magneto-optical response of one electron in an eight-level system.

We start setting the concept of coherence considered here to well situate our work.

We present then the spin-orbit eight-level model developed by Hélène Vonesch in her PhD thesis to explain the magneto-optical response in the scope of a pump and probe experiment, where the polarization of the field emitted by the material is studied.

Considering a hydrogen-like system, we discuss the relativistic interaction hamiltonian of Dirac and the Foldy-Wouthuysen tranformation, that allow separating the equations of the two particles.

Using the Liouville equation, we describe the evolution of the density matrix and show the evolution of coherences and populations in an eight-level system in the simple case of dipolar interaction to explain the method used.

The different terms contained in the magneto-optical response are presented and after the microscopic description in terms of the density matrix, the link to the macroscopic approach is made via the polarization to first and third order. Based on the assumption that the radiated field equals the polarization of the material, we calculate the intensity of the emitted field in the directions of detection.

2.1 Definitions of coherence

Many different concepts of coherence are now considered in the publications. We set here the most used ones to well situate ours.

2.1.1 Laser coherence

A light field is called coherent when there is a well-defined phase relationship between the electric field values at different locations and different times. Spatial coherence is the essential pre-requisite to have strong directional laser beams [81].

Here, one finds a first definition of coherence time, to be called laser coherence time, that quantifies the time over which the laser coherence is lost.

2.1.2 Relation between ground and excited states - density matrix formalism

The Liouville space descriptions are commonly used in the description of nonlinear optics of few-level systems [82].

We consider a quantum system that is a superposition of pure states $|\Psi_k(t)\rangle$. The probability of finding the system in the state $|\Psi_k(t)\rangle$ being P_k (positive), we define the density operator, also called density matrix, as

$$\rho(t) = \sum_k P_k |\Psi_k(t)\rangle\langle\Psi_k(t)|, \tag{2.1}$$

being the density matrix elements given, on an arbitrary basis set, by

$$\rho_{nm} = \sum_k P_k \langle n|\Psi_k\rangle\langle\Psi_k|m\rangle. \tag{2.2}$$

The diagonal elements ρ_{nn} of the density matrix are positive and can be viewed as the probability of the system to be found in the state $|n\rangle$ by detection through an analyser that rejects states orthogonal to $|n\rangle$. They are called populations. The nondiagonal elements ρ_{nm} (with $n \neq m$) are generally complex numbers and may contain a phase, they are called coherences.

The evolution of the density operator is given by the Liouville equation, as detailed further in section 2.2.1.2.

2.1.3 Coherence of the dipoles

The coherent excitation of a material by an ultrashort laser pulse creates dipoles that oscilate in phase with the laser field. In other words, due to the dipolar interaction, a well defined relation between the phase of the laser and the phase of the dipoles exists. While this phase is conserved, the system is in a coherent regime. The coherent oscilation of the elementary excitations gives rise to a macroscopic polarization in the medium. Since the system is not isolated, one has to take into account the environnement (another origin of the decoherence). The lifetime T_1 of the excited state is half of the dephasing time T_2 in the case of an isolated atom. For condensed matter systems, $T_1 \ggg T_2$ as the dephasing is due to the interaction with a complex environment such as phonons, crystallinity, etc.

2.1.4 Coherence of the macrospins

One may consider all magnetic moments of all spins as a giant magnetic moment as they are strongly coupled to each other. This is called the macrospin. The so-called coherence time of the macrospin T_{2p}, commonly found in the description of precession (as in section 1.2.2.2), describes the loss of phase between the spins. This pure dephasing can be different than the one of the charges. Generally it is due to the interactions between the magnons and the phonons.

2.1.5 Conclusion

We have reviewed the concept of coherence to define the notion of coherence that will be considered throughout this thesis. It refers to the phenomena happening while the system is still in phase with the laser field excitation.

2.2 Modeling of the coherent magneto-optical response

In this section, we extend the formalism of the two-level system already described in section 1.1.4 to the case of a multilevel system. The work developed by Hélène Vonesch in her PhD thesis [83] defended in 2011 is reviewed, as it will form the basis of the interpretation of our magneto-optical measurements. She has used the Liouville formalism to write the coherent magneto-optical response of an eight-level hydrogen-like system to a short laser pulse excitation. This model takes into account the fundamental relativistic quantum dynamics of the spins [84] and the slowly varying envelope pulse approximation.

2.2.1 Dynamics in hydrogen-like systems

The hydrogen atom is the simplest system that can be used to model the response of a system. Using a relativistic approach via the Foldy-Wouthuysen transformation of the Dirac equation, it is possible then to study the interaction hamiltonian of Dirac, that considers the spin-orbit interaction, to explain the coherent coupling as initially proposed by our group [4].

We present, in a first step, how to obtain the hamiltonian used in the model and the method used to obtain the evolution of coherences and populations, taking as an example the case of one electron and considering dipolar interaction.

2.2.1.1 The hamiltonian - Foldy-Wouthuysen transformation

The Dirac hamiltonian for an electron under a vector potential $\overrightarrow{A}$ and electric potential U is written as

$$H = c\overrightarrow{\alpha} \cdot (\overrightarrow{p} - q\overrightarrow{A}) + mc^2\beta + qU, \tag{2.3}$$

where $\overrightarrow{\alpha}$ and β are two matrices of dimension 4, written as follows.

$$\overrightarrow{\alpha} = \begin{pmatrix} 0 & \overrightarrow{\sigma} \\ \overrightarrow{\sigma} & 0 \end{pmatrix} \text{ and } \beta = \begin{pmatrix} 1 & 0 \\ 0 & -1 \end{pmatrix} \tag{2.4}$$

At high energies, the Dirac's equation has two coupled solutions corresponding to the electron and to the positron that disappear at low energies in the nonrelativistic approximation. In this context, the Foldy-Wouthuysen transformation allows the separation of the equations of the two particles keeping the relativistic concept contained in the Dirac's equation. It is via this transformation that the relativistic contributions to the ultrafast magneto-optical dynamics play a role.

Considering the temporal dependence of the external field to the second order in $\frac{1}{m}$ (an approximation to fifth order can be obtained in reference [85]) and neglecting the contributions of the temporal derivative of $\overrightarrow{E}$, we have the following hamiltonian [86].

$$\begin{aligned} H =& mc^2 + \frac{1}{2m}(\overrightarrow{p} - q\overrightarrow{A})^2 + qU - \frac{q\hbar^2}{8m^2c^2}\overrightarrow{\nabla} \cdot \overrightarrow{E} - \frac{q}{m}\overrightarrow{S} \cdot \overrightarrow{B} \\ & - \frac{q}{4m^2c^2}\overrightarrow{S} \cdot \left[2\overrightarrow{E} \wedge \overrightarrow{p} + i\hbar\overrightarrow{\nabla} \wedge \overrightarrow{E} - 2q\overrightarrow{E} \wedge \overrightarrow{A}\right] \end{aligned} \tag{2.5}$$

Knowing that $\overrightarrow{E}_i$ is the ionic field, U_i is the scalar ionic potential, $\overrightarrow{B}_M$ is the static magnetic field applied, $\overrightarrow{A}_M$ is the applied static vector potential, $\overrightarrow{E}_L$ is the laser electric

field, $\overrightarrow{B}_L$ is the laser magnetic field, U_L is the laser scalar potential and $\overrightarrow{A}_L$ is the laser vector potential, the hamiltonian described in equation 2.5 is divided in two parts: H_0 is the hamiltonian not perturbed by the laser interaction and H_{int} is the system-laser interaction hamiltonian.

$$\begin{aligned} H_0 =& mc^2 + \frac{1}{2m}(\overrightarrow{p} - q\overrightarrow{A}_M)^2 + qU_i(\overrightarrow{r}) - \frac{q}{m}\overrightarrow{S}\cdot\overrightarrow{B}_M \\ & - \frac{q}{2m^2c^2}\overrightarrow{S}\cdot[\overrightarrow{E}_i \wedge (\overrightarrow{p} - q\overrightarrow{A}_M)] - \frac{q\hbar^2}{8m^2c^2}\overrightarrow{\nabla}\cdot\overrightarrow{E}_i \end{aligned} \tag{2.6}$$

$$\begin{aligned} H_{int} =& -\frac{q}{m}\overrightarrow{\Pi}\cdot\overrightarrow{A}_L - \frac{q}{2m^2c^2}[(\overrightarrow{p} - q\overrightarrow{A}_M)\wedge\overrightarrow{S}]\cdot\overrightarrow{E}_L \\ & - \frac{q}{m}\overrightarrow{S}\cdot\overrightarrow{B}_L - \frac{iq\hbar}{4m^2c^2}\overrightarrow{S}\cdot(\overrightarrow{\nabla}\wedge\overrightarrow{E}_L) \end{aligned} \tag{2.7}$$

where $\overrightarrow{\Pi} = \overrightarrow{p} - q\overrightarrow{A}_M + \frac{q}{2mc^2}\overrightarrow{S}\wedge\overrightarrow{E}_i$ is the generalized momentum, which contains the contributions of the orbital and spin momenta.

Given that the electric field is not homogeneous, other physical phenomena must be considered, in particular the electric dipolar interaction, the magnetic dipolar interaction and the electric quadrupolar interaction.

2.2.1.2 Method to model an eight-level system

The method to obtain the evolution of coherences and populations is presented here to the case of a system where H_0 is the nonperturbed hamiltonian and $-\overrightarrow{V}\cdot\overrightarrow{E}_{laser}$ is the interaction with the laser field. It consists in studying the evolution of the density matrix in this system.

In the case of this simple example, using the quantum Liouville equation and the density matrix formalism, allows writing

$$i\frac{d\rho}{dt} = \frac{1}{\hbar}\left[H_0 - \overrightarrow{V}\cdot\overrightarrow{E}_{laser}, \rho\right]. \tag{2.8}$$

Considering that the thermic bath induces mechanisms of relaxation of the population and of the coherences [87], the equation becomes then

$$i\frac{d\rho}{dt} = \frac{1}{\hbar}\left[H_0 - \overrightarrow{V}\cdot\overrightarrow{E}_{laser}, \rho\right] + i\frac{d\rho}{dt}|_{relaxation}. \tag{2.9}$$

For a multilevel system $|m\rangle$, the relaxation terms take the following form.

$$i\frac{\delta\rho}{\delta t}|_{relaxation} = \begin{cases} -\frac{i}{T_{nm}}(\rho_{nm} - \rho_{nm}^{(0)}), & \text{if } n \neq m \text{ or} \\ -\frac{i}{T_1}(\rho_{nn} - \rho_{nn}^{(0)}), & \text{if } n = m, \end{cases} \tag{2.10}$$

being $\rho_{nm}^{(0)}$ the density matrix element in the equilibrium, T_{nm} the coherence relaxation time and T_1 the population lifetime.

Using the perturbation method by developing ρ in the order of perturbation of $\overrightarrow{V} \cdot \overrightarrow{E}_{laser}$, we obtain a new form of the equation of evolution. It is possible then to obtain the temporal evolution of the density matrix, given by

$$\rho_{nm}^{(N>0)}(t) = \frac{i}{\hbar} e^{-i\omega_{nm}t - \frac{t}{T_{nm}}} \Theta(t) \otimes \left\{ E_i(t) \sum_l \left[v_{nl}^i \rho_{lm}^{(N-1)} - \rho_{nl}^{(N-1)} v_{lm}^i \right] \right\}, \tag{2.11}$$

where $\omega_{nm} = \dfrac{E_n - E_m}{\hbar}$ and v^i is the projection of $\overrightarrow{V}$ in the direction $\overrightarrow{e}_i$ and $\Theta(t)$ is the Heaviside function.

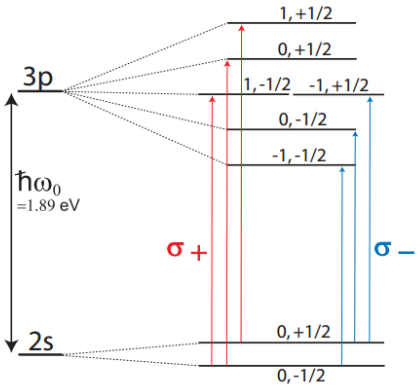

Figure 2.1: Considered transitions in the hydrogen-like atom. For each level, the orbital momentum l_z and the spin momentum s_z are indicated. $\sigma_\pm$ stands for a circularly polarized field. Figure from reference [84].

Applying this method to an eight-level system, as the one shown in figure 2.1, considering a lineraly polarized gaussian pulse and defining $\Delta n_{nm} = \rho_{nm} - \rho_{mm}$ as the population difference, $E = 3, 4, 5, 6, 7$ as the index representing the excited levels, $F = 1, 2$ as the index representing the two fundamental states and the slowly varying envelope for $n \geq 3$ e $m \leq 2$ as $\tilde{\rho}(t) = \rho_{nm}(t)e^{i\omega_L t}$, we have the evolution of coherences are given by

If $n \in E$ and $m \in F$:

$$\tilde{\rho}_{nm}(t) = \frac{i}{2\hbar} e^{i(\omega_L - \omega_{nm})t - \frac{t}{T_{nm}}} \Theta(t) \otimes \left\{ \sum_{l \leq 2} v_{nl}\rho_{lm}\epsilon - \sum_{l \geq 3} \rho_{nl} v_{lm}\epsilon \right\} \tag{2.12}$$

If $(n, m) \in E^2$:

$$\rho_{nm}(t) = \frac{i}{2\hbar} e^{-i\omega_{nm}t - \frac{t}{T_{nm}}} \Theta(t) \otimes \left\{ \sum_{l \leq 2} v_{nl}\tilde{\rho}_{lm}\epsilon - \tilde{\rho}_{nl} v_{lm}\epsilon^* \right\} \tag{2.13}$$

If $(n, m) \in F^2$ (i.e. $n = 2$ and $m = 1$):

$$\rho_{21}(t) = \frac{i}{2\hbar} e^{-i\omega_{21}t - \frac{t}{T_{nm}}} \Theta(t) \otimes \left\{ \sum_{l \geq 3} v_{2l}\tilde{\rho}_{l1}\epsilon^* - \tilde{\rho}_{2l}\epsilon v_{l1} \right\} \tag{2.14}$$

and the evolution of population differences given by

If $n \in E$ and $m \in F$:

$$\Delta n_{nm}(t) = \frac{i}{2\hbar} e^{-\frac{t}{T_1}} \Theta(t) \otimes \left\{ \sum_{l \leq 2} v_{nl}\tilde{\rho}_{ln}\epsilon - \tilde{\rho}_{ln} v_{nl}\epsilon^* - \left[\sum_{l \geq 3} v_{ml}\tilde{\rho}_{lm}\epsilon^* - \tilde{\rho}_{ml} v_{lm}\epsilon \right] \right\} \tag{2.15}$$

If $(n, m) \in E^2$:

$$\Delta n_{nm}(t) = \frac{i}{2\hbar} e^{-i\frac{t}{T_1}} \Theta(t) \otimes \left\{ \sum_{l \leq 2} v_{nl}\tilde{\rho}_{ln}\epsilon - \tilde{\rho}_{nl} v_{ln}\epsilon^* + v_{ml}\tilde{\rho}_{lm}\epsilon^* - \tilde{\rho}_{ml} v_{lm}\epsilon \right\} \tag{2.16}$$

If $(n, m) \in F^2$ (i.e. $n = 2$ and $m = 1$:

$$\Delta n_{21}(t) = \frac{i}{2\hbar} e^{-\frac{t}{T_{nm}}} \Theta(t) \otimes \left\{ \sum_{l \geq 3} v_{2l}\tilde{\rho}_{l2}\epsilon^* - \tilde{\rho}_{1l}\epsilon v_{l1} - v_{1l}\tilde{\rho}_{l1}\epsilon^* - \tilde{\rho}_{1l}\epsilon v_{l1} \right\}. \tag{2.17}$$

Starting from the Dirac hamiltonian and considering the Foldy-Wouthuysen transformation, we have obtained a reduced relativistic hamiltonian of an electron. We have then showed how to use the Liouville equation to obtain the evolution of the density matrix elements constituted of eight energy levels, consistent with the multiplicity of the hydrogen atom in the visible spectrum. To apply this model to obtain the magneto-optical response of a medium, one must use the hamiltonian of equations 2.6 and 2.7. The results of this study will now be further detailed.

2.2.2 Interpretation of the different terms in the pump and probe signal

To well understand how the coherences and populations dynamics are present in the response of a discrete-level system to an optical excitation, one must study the different terms present in this response.

The nonlinear interaction of the atoms with the pump and probe beams gives rise to a radiated field. Considering a system that has a third order response, the third order polarization is written as a function of the susceptibility tensor as follows. This is a special case of equation 1.2.

$$P^{(3)} = \sum \varepsilon_0 \chi^{(3)} \left(\omega_s; \omega_i, \omega_j, \omega_k\right) E_i(\omega_i) E_j^*(\omega_j) E_k(\omega_k) \tag{2.18}$$

A perturbative treatment in the time domain with a dipolar interaction involving the total field $E_p + E_s$ has been developed to understand the charges dynamics in a two-level system [88]. The resolution of the Liouville equation at third order of perturbation in the field gives rise to time ordered integrals with several permutations of the pump and probe fields along the probe direction. Considering $t_1 \leq t_2 \leq t_3$, three important terms have to be considered for the pump and probe signal in the direction $\overrightarrow{k}_s$, where $\overrightarrow{k}_s$ is the wave vector of the probe field. These three terms involve the following sequence of fields:

- Pump polarization coupling (PPC): $E_p^*(t_1)E_s(t_2)E_p(t_3)$,
- Pump-perturbed free induction decay (PP-FID): $E_s(t_1)E_p^*(t_2)E_p(t_3)$,
- Population terms: $E_p(t_1)E_p^*(t_2)E_s(t_3)$ and $E_p^*(t_1)E_p(t_2)E_s(t_3)$.

The pump polarization coupling term is present only when the three fields coincide in time. Its temporal shape is therefore a direct convolution of these three fields. It contains no information on the system relaxation (nor T_2 nor T_1). The pump-perturbed free induction decay term differs from the first one in the sense that the polarization of the probe perturbs the one of the pump. It rises with the time T_2 and it is present when the probe precedes the pump. The population terms describe the changes of the population induced by the pump, that are still present when the probe arrives. They decay with the lifetime T_1 and are maximal for positive delays.

2.2.3 Pump and probe measurement

The matrix density allows one to go from a microscopic approach, described so far as the model of one electron in an eight-level system via its hamiltonian, to the macroscopic approach, described by the polarization of the material. The first and third order polarizations can be found from the dipolar moment of the system, $\overrightarrow{D}$ as mentioned in section 1.1.4.

$$\overrightarrow{P}^{(1)}(t) = Tr[\rho^{(1)}(t)\overrightarrow{D}] \text{ and } \overrightarrow{P}^{(3)}(t,\tau) = Tr[\rho^{(3)}(t,\tau)\overrightarrow{D}]. \tag{2.19}$$

Being the linearly polarized laser field $\overrightarrow{E}_{laser}$ written as

$$\overrightarrow{E}_{laser} = \frac{1}{2}\left[\epsilon(t,\tau)e^{-i\omega_L t+ik_L t} + \epsilon^*(t,\tau)e^{i\omega_L t-ik_L t}\right]\overrightarrow{e}_x, \tag{2.20}$$

where $\epsilon(t,\tau)$ is a Gaussian centered on the pump and probe delay τ or 0 in the case of the probe or pump field, k_L is the laser field wave vector and ω_L is its frequency. Assuming that one does not consider the effects of interface between the material and vacumm (or air), one can write that $E^{(n)} \equiv P^{(n)}$. Else, one should consider the conservation laws of the electromagnetic field at such surface.

Faraday analysis

In a pump and probe experiment, the polarization of the field emitted by the material in the direction of the probe field is studied. The emitted field is the sum of the first and third order fields. Neglecting the quadratic term in $\overrightarrow{E}^{(3)}$, the intensity measured is then

$$\begin{aligned} I(\tau) &= \int_{-\infty}^{+\infty} |\overrightarrow{E}^{(1)}(t) + \overrightarrow{E}^{(3)}(t,\tau)|^2 dt \\ &\simeq \int_{-\infty}^{+\infty} |\overrightarrow{E}^{(1)}(t)|^2 dt + 2\int_{-\infty}^{+\infty} \Re[\overrightarrow{E}^{(1)}(t)\cdot\overrightarrow{E}^{*(3)}(t,\tau)]dt. \end{aligned} \tag{2.21}$$

Considering the polarization bridge configuration, that consists in using waveplates and a polarizing cube to separate the two components of the beam polarization in two arms x and y (to be more detailed in section 3.5.2.3), to analyse the polarization of the initially linearly polarized probe beam, one may define the magneto-optical rotation induced by the material as follows.

$$\frac{\Delta\Theta(\tau)}{\Theta} = \frac{\Delta\Theta_{+B_M}(\tau) - \Delta\Theta_{-B_M}(\tau)}{\Theta_{+B_M} - \Theta_{-B_M}} \text{ where } \Delta\Theta_{\pm B_M}(\tau) = [I_x - I_y]_{\pm B_M}, \tag{2.22}$$

being $I_{x,(y)} = 2\int_{-\infty}^{+\infty} \Re[\overrightarrow{E}^{(1)}_{x,(y)}(t) \cdot \overrightarrow{E}^{*(3)}_{x,(y)}(t,\tau)]dt$ the differential measurement obtained by the difference between the signals when the pump is present or not (mechanical chopping scope) and $+B_M$ and $-B_M$ the opposite directions of the external magnetic field.

Magneto-optical four-wave mixing analysis

The field emitted in the MO-FWM directions, in the two or three-beam configurations, is different from the one emitted in the probe direction because it does not contain the linear field. It corresponds to the quadratic term in $E^{(3)}$. The intensity in the detectors, in the case of the study of a homogeneous system, will then be given by

$$I(\tau) = \int_{-\infty}^{+\infty} |\overrightarrow{E}^{(3)}(t,\tau)|^2 dt, \text{ for the two-beam configuration and} \tag{2.23}$$

$$I(\tau,T) = \int_{-\infty}^{+\infty} |\overrightarrow{E}^{(3)}(t,\tau,T)|^2 dt, \text{ for the three-beam configuration.} \tag{2.24}$$

Dynamics of spins and orbital moments

The study of the magnetic effects via the dynamics of the orbital moment and the spin moment is also possible with this model. The projection of the spin and orbital moments dynamics in the $\overrightarrow{e}_z$ direction are given as a function of the trace of the operators and the second order density matrix elements as follows.

$$\langle S_z^{(2)} \rangle(t,\tau) = Tr\left[\rho^{(2)}(t,\tau) S_z\right] \tag{2.25}$$

$$\langle L_z^{(2)} \rangle(t,\tau) = Tr\left[\rho^{(2)}(t,\tau) L_z\right] \tag{2.26}$$

2.3 Results of the simulations

To model the magneto-optical response of a medium, one must consider in equation 2.8 the hamiltonian given by 2.6 and 2.7. With that, it is possible to extend the optical approach presented in section 2.2.2 to the magneto-optical configuration in order to find the dynamics of coherences and populations in the pump and probe signals.

Figure 2.2 shows the dynamics of the differential magneto-optical rotation given by equation 2.22 calculated for each of the terms presented in section 2.2.2 using the hamil-

tonian given by 2.7. In the simulation, we considered a gaussian pulse of width $10fs$, a probe field ten times less intense than the pump field, $T_1 = 100fs$ and $T_2 = 10fs$ and the external magnetic field of magnitude $1T$.

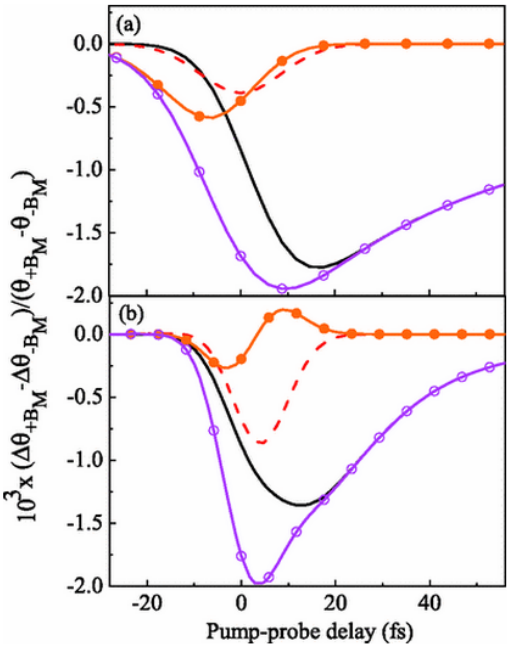

Figure 2.2: Magneto-optical rotation for the population (black straight line), PPC (red dashed line), PP-FID (orange closed circles) and total (purple open circles) signals. (a) On resonance ($\hbar\omega_L = \hbar\omega_0 = 1,89eV$) and (b) off resonance ($\hbar\omega_L = 1,51eV$). Figure from reference [84].

From the part *b* of figure 2.2, it is clear that for an off resonance excitation ($\hbar\omega_L < \hbar\omega_0$) the coherent contribution to the total signal is larger as compared to the resonant case.

Figure 2.3 shows the dynamics of the projection of the spin and orbital moments in the $\overrightarrow{e}_z$ direction for the three time-ordered terms presented in section 2.2.2.

These results motivate the experiments on and off resonance, being the off resonance configuration more interesting to study the coherent effects present in the magneto-optical response. Let us emphasize that the off-resonance excitation is ideal when the spectrum of the pulse does not overlap the energy levels, broadened by their intrinsic linewidth ($\sim 1/T_2$). It also shows that the dynamics of the spin and orbital angular moments are not the same and that both participate in the coherent response. The time ordering of the pulses has a great importance to distinguish the coherence and the population components.

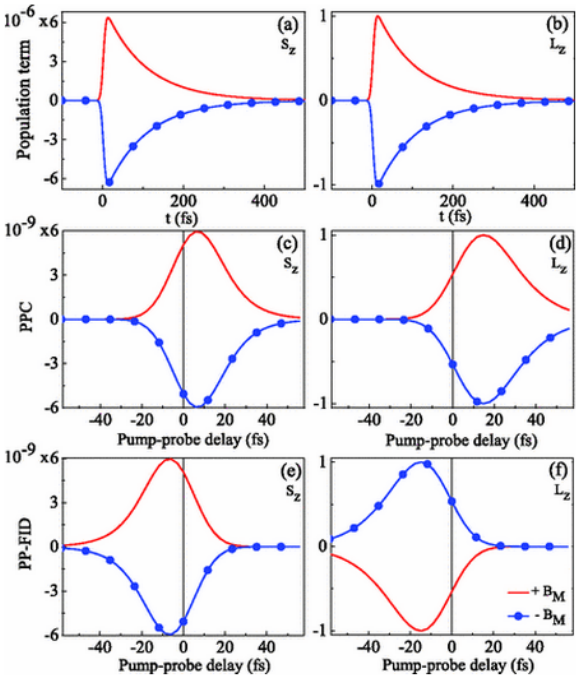

Figure 2.3: Spin and orbital moments dynamics for the pump and probe sequences for $+B_M$ (red straight line) and for $-B_M$ (blue closed circle). (a) $Tr[\rho^{(2)}S_z(t)$ and (b) $Tr[\rho^{(2)}L_z(t)]$ for the population term. (c) $Re\int dtTr[\rho^{(2)}S_z(t,\tau)]$ and (d) $Re\int dtTr[\rho^{(2)}L_z(t,\tau)]$ for the PPC term. (e) and (f) are the same quantities as (c) and (d) but for the PP-FID. Figure from reference [84].

2.4 Conclusions

We have shown in this chapter that the magneto-optical response can be modelled considering an eight-level system and the relativistic correction of the hamiltonian. This model shows that the dynamics of the coherences and populations are connected to the dynamics of the spins and orbital momenta due to the time ordering of the interacting fields.

The interaction hamiltonian to be used in the model was obtained considering the Foldy-Wouthuysen transformation. We have used the example of dipolar interaction to show how to obtain analytical solution for the evolution of the coherences and populations with the interaction hamiltonian. Using this method we have simulated the dynamics of the coupled spins and orbital momenta and the corresponding Faraday rotation.

This simplified approach can then be used to interpret and validate the MO-FWM mixing signals measured with the experimental techniques to be described in the following chapter.

Chapter 3

Experimental approach

In this chapter we will present the experimental techniques that allowed us to study the magneto-optical response of a garnet sample.

In a first part, we introduce the garnet as the material of interest of this study for its important magneto-optical properties. The most important properties of different types of garnets are then presented followed by the description of the elaboration and characterization of the garnet sample used in this study.

We will then, in a second part, present a general description of the experimental apparatus used in the measurements of the dynamical properties of this sample. We present the generation of ultrashort laser pulses and how it is done in the femtosecond oscillator based on a titanium-doped sapphire crystal. A part of the results presented in this thesis was obtained using nonamplified pulses delivered by an oscillator of this type. As other results were obtained using amplified pulses, we describe how the pulses generated by an oscilator can be amplified using the method of chirped pulse amplification.

As in the case sub-$10fs$ pulses, the dispersion can be of great importance, we present how to pre-compensate the dispersion induced by the experimental set-up using a prism compressor or chirped mirrors in order to obtain the optimal pulse duration. The pulse characterization is also studied and examples are shown.

Having presented how the pulses are generated, how the dispersion is controled and how their characterization is made, we describe the systems, set-ups and detection configurations used in the different experiments of this thesis.

3.1 Garnet sample

3.1.1 Garnets found in nature

The garnet, named from the latin word *granatus* for its ressemblance with the pomegranate seed color when found in nature, is a crystal of general formula $X_3Z_2(TO_4)_3$, where X, Z and T are different cations. In nature, when the cation T is Si^{4+}, they are found in many colors and their light transmission properties can vary a lot.

Figure 3.1: Examples of garnets found in nature.

3.1.2 Synthetic garnets

Synthetic garnets have been produced to replace the gems of the natural ones for a long time. The yttrium aluminium garnet (YAG), $Y_3Al_2(AlO_4)_3$, famous for its high refractive index, was manufactured as a diamond substitute in the 1970s. A garnet crystal can accept several rare-earth ions in substitution, each one playing a different role in modifying its properties.

Iron garnets have been manufactured since the 1950s. They present general formula $X_3Fe_2(FeO_4)_3$, where X is a trivalent cation. This composition can be seen as $\{X^{3+}\}_3[Fe^{3+}]_2(Fe^{3+})_3O_{12}$, where {} represents the dodecahedral site, with one trivalent cation surrounded by eight ions O^{-2}, [] represents the octahedral site, with one cation Fe^{3+} surrounded by six ions O^{-2} and () represents the tetrahedral site with one cation Fe^{3+} surrounded by four ions O^{-2}.

The three iron atoms in the tetrahedral site are aligned in a ferromagnetic way, as well as the two iron atoms in the octahedral site. However, the two sublattices are aligned in an antiferromagnetic way. Iron garnets have high Curie temperature due to the strong

superexchange interaction between the two sites, defined generally as the strong antiferromagnetic coupling between two neighbour cations through a nonmagnetic anion.

The different number of octahedral and tetrahedral sites in the garnet lattice causes a noncompensation of the magnetic moments of the two sublattices, as shown in figure 3.2. The resulting $5\mu_B$ gives rise then to a sponteneous magnetization. All oxigen atoms are identical and bonded to one tetrahedron and one octahedron (and to two other dodecahedral sites). Because of its high volume, the dodecahedral site can contain any rare-earth ion.

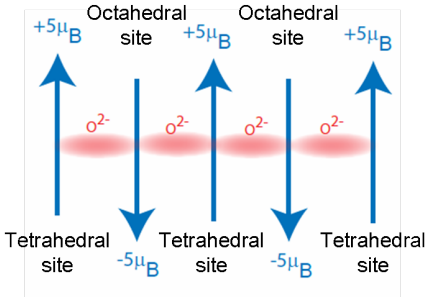

Figure 3.2: Antiparallel structure of magnetic moments in garnets.

The level structure of garnets can be rather complex. Figure 3.3 presents the molecular-orbital energy diagram proposed for the $Bi_3Fe_5O_{12}$ garnet in reference [89].

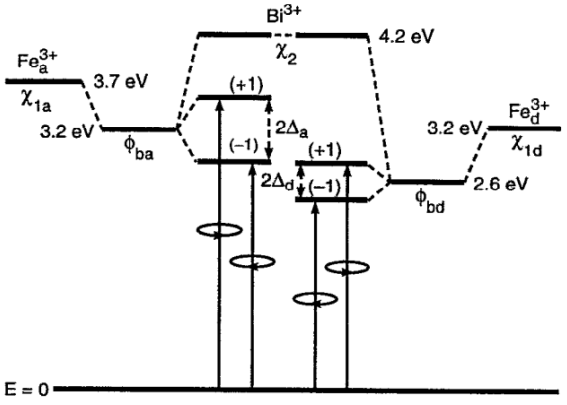

Figure 3.3: Molecular-orbital energy level diagram of $Bi_3Fe_5O_{12}$. The circles $+1$ and -1 show how to achieve these levels from the ground state with circularly polarized light with right or left orientation, respectively. d stands for octahedral and a for tetrahedral. Figure from reference [89].

An example of substitution in the dodecahedral site is the yttrium iron garnet (YIG),

$Y_3Fe_2(FeO_4)_3$, known as the model system of the magnetic iron garnets. By replacing yttrium with bismuth, for example, as it will be presented in the next section, a magnetic garnet with different physical properties can be created.

Another example is the gadolinium gallium garnet, called GGG ($Gd_3Ga_2(GaO_4)_3$), which is synthesized to be used as a substrate for liquid-phase epitaxy of magnetic garnet films for magneto-optical applications. It is transparent from $0,38\mu m$ to $6\mu m$ and its refractive index, that varies linearly with temperature between 18 and $140°C$, is 1.96 at $800nm$. Optical properties of the GGG are given in more details in reference [7].

3.1.3 Magnetic characterization of garnets

A generic approach widely used in the litterature to explain the transitions responsible for the magneto-optical effects in garnets considers two classes of magneto-optical interactions: the paramagnetic case with a Zeeman-splitted ground state g, and the diamagnetic case with an excited state a splitted by 2Δ due to spin-orbit coupling, as shown in figure 3.4 [90].

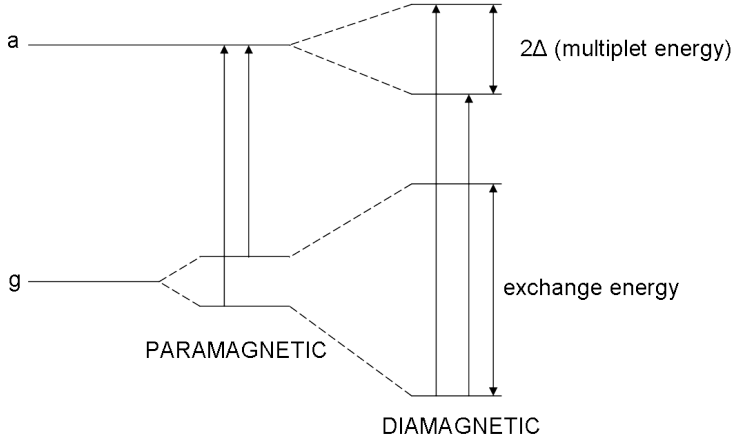

Figure 3.4: Spectral transitions for paramagnetic and diamagnetic cases that arises from ferrimagnetism.

The study of ferrimagnetic garnets, for example, is based on the diamagnetic transitions. Each one of the ions Fe^{3+} presents a diamagnetic diagram of transitions like shown in figure 3.4. However, many synthetic garnets often have several resonances within the ultraviolet and visible region [91] leading to a richer absorption spectrum.

The Faraday rotation has been studied as a function of the excitation energy in gadolinium iron garnets (GdIG) [92]. It was shown that the behavior of the Fe^{3+} sublattices are close to the ones in pure YIG and that the contribution from the octahedral site is dom-

inant, depending on the photon energy. Gd^{3+} contributes little to the electric dipole rotation. These variations are more likely to be the result of a charge transfer process involving a $Fe^{3+} - O^{2-} - Gd^{3+}$ combination.

Gallium substitution reduces the optical absorption and magneto-optical effects, because it replaces the active iron ion at the tetrahedral and octahedral sites [93], while bismuth substitution on garnets is known for increasing the refractive index and the absorption [94].

The enhancement of the spin-orbit coupling with bismuth content was proposed as the origin of this large magneto-optical effect after studies on the off-diagonal dielectric tensor elements of bismuth-substituted iron garnets [91]. A study of bismuth iron films with different stoichiometries showed that the bismuth concentration affects the magneto-optical response of the tetrahedral iron sublattice while the iron concentration affects the response of the octahedral sublatice [95].

In bismuth-substituted magnetic garnets, of general formula $Y_{3-x}Bi_xFe_5O_{12}$, the three diamagnetic type Fe^{3+} transitions are influenced by the covalent interactions with Bi^{3+} ions, responsible for the large splitting of the degenerated states of Fe^{3+} of the two sites of the garnet structure [89]. The $Fe^{3+} - O^{2-} - Bi^{3+}$ bond linkages rule the perturbation of the multiplet splitting of the excited band of Fe^{3+} lattices caused by Bi^{3+}.

In completely bismuth substituted iron garnets (BIG), of formula $Bi_3Fe_5O_{12}$, the spin-orbit coupling due to Bi in the Fe 3d conduction bands was found to be of great importance in the large magneto-optical effect observed (more than in the O 2p and Fe 3d valence bands) [96].

In bismuth substituted ferrite garnets, a model based on two optical diamagnetic transitions, being one tetrahedral and one octahedral shows excellent agreement with the experimental data in the visible range [97].

Another model proposing the superposition of two hysteresis loops corresponding to the two sublattices of BIG has been introduced in reference [98]. They propose also a third diamagnetic transition with the same sign of the tetrahedral transition to be added to the model of Dionne and Allen [90] [89] to explain the Faraday rotation and ellipticity beyond $3,5eV$ of photon energy.

3.1.4 Elaboration and characterization of the garnet studied in this work

We have chosen to analyse a ferrimagnetic garnet, doped with bismuth, of formula $(GdTmPrBi)_3(FeGa)_5O_{12}$ made by liquid phase epitaxy [6], that consists in dipping the turning substract in a saturated solution containing the oxides of the different components to be deposited and the solvent, usually PbO and B_2O_3. The growing requires a well

controlled temperature between 700 and $1000°C$ and happens on both sides of the substract that acts like the seed for the crystal growth. The $7\mu m$ thick film has a strong uniaxial magnetic anisotropy perpendicular to its plane and was deposited on both sides of a $500\mu m$ GGG substrate. Its magnetization at saturation is $\sim 800A/m$ or $\sim 10G$.

The Bi is responsible for increasing the magneto-optical effects, as discussed before, Pr, for changing the anisotropy, Tm, for compensating the lattice parameter mismatch with the substrate and for bringing the compensation temperature under the ambient temperature and Gd, for changing the magnetic properties of the sample (being the anti-ferromagnetic interactions between the iron ions of the octahedral and tetrahedral sites still more important) [5]. The important Faraday rotation in the $(GdTmPrBi)_3(FeGa)_5O_{12}$ garnet is due to the ions Fe^{3+} and Bi^{3+}. The Bi^{3+} splits the orbitals of Fe^{3+}; the orbitals $6p$ from Bi^{3+}, $2p$ from O^{2-} and $3d$ from Fe^{3+} overlap and this leads to the energy sppliting of 2Δ [91].

In litterature, magneto-optical data are generally classified in Kerr effect ellipsometry measurements of the off-diagonal complex elements of the dielectric tensor (for energies from 2 to $5eV$) and in static Faraday rotation measurements (below $2eV$). Reference [91] shows both analysis. In figure 3.5, we present the static Faraday rotation and the extinction ratio obtained for the two directions of the magnetic field ($350mT$), applied perpendicularly to the sample.

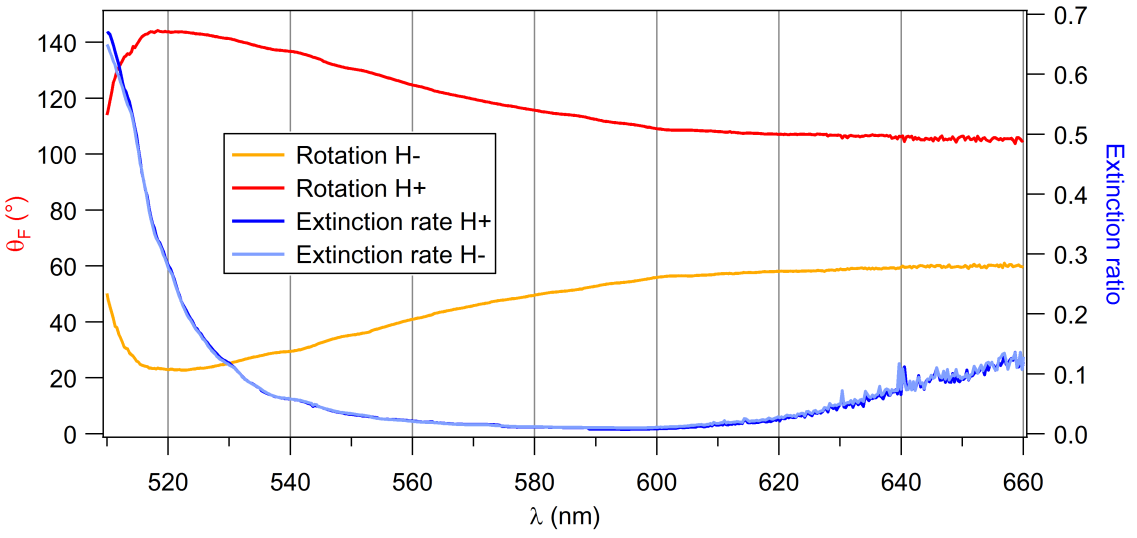

Figure 3.5: Static Faraday rotation and extinction ratio for two directions of the perpendicular external magnetic field as a function of the wavelength.

One observes a large magneto-optical resonance at $575nm$. The results presented in this thesis were obtained with ultrashort pulses with spectrum centered at $800nm$, range where the coherent magneto-optical response of the garnet is resonant.

Reference [99] describes the elaboration of a garnet of formula $Bi_1Gd_{1,4}Tm_{0,4}Pr_{0,2}Fe_{4,5}Ga_{0,5}O_{12}$ deposited on $(GdCa)_3(GaMgZr)_5O_{12}$ that differs in concentration and substrate from the garnet studied in this thesis. In reference [99], the substrate was chosen for having the lattice constant close to the one from the magnetic material to be deposited. It is a garnet of the type $Gd_2Bi_1Fe_5O_{12}$ where a part of the Gd was replaced with Tm and Pr. The presence of Bi induces an important increase of the Faraday rotation ($17500°/cm$, measured at $632,8nm$) and the presence of Tm reduces the compensation temperature to under the room temperature ($213K$, where the magnetization goes to zero [5]). The anisotropy constant decreases with higher concentrations of Pr.

3.2 Femtosecond pulse generation

3.2.1 Lasing

The lasing phenomenon can be represented by a four-level system model, shown in figure 3.6. The pump photon at $532nm$ is absorbed by the material (semiconductors, crystals, dyes, fibers or gases) inducing population inversion from E_1 to E_2 levels. The electrons relax in a nonradiative way to E_3 and the stimulated emission at $800nm$ occurs between E_3 and E_4 levels.

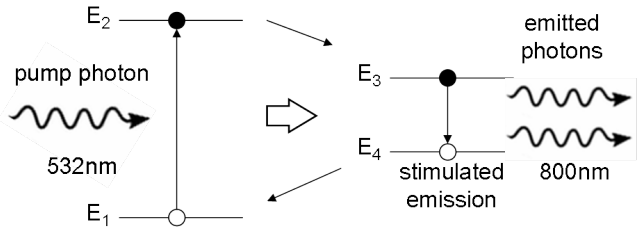

Figure 3.6: Four-level system description of stimulated emission.

3.2.2 Mode-locking

Continuous laser sources are characterized by their monochromaticity. On the other hand, an important property of the sources that generate ultrashort pulses is their wide spectrum. The time-frequency relation defines the relation between the pulse of duration Δt and spectral bandwidth $\Delta\omega$. This way, the frequency and the temporal widths, Δt and $\Delta\nu$,

respectively, are connected by Fourier transform, as follows.

$$\Delta t.\Delta\nu \geqslant K, \tag{3.1}$$

being K a constant related to the temporal profile of the pulse ($K = 0,441$ to a Gaussian; $K = 0,315$ to a hyperbolic secant). The equality case in relation 3.1 describes then the shortest possible duration at a given spectral width and pulse shape.

However, having a large spectrum, which means, finding a gain medium with a broad gain bandwidth, is not the only condition for having short pulses from a laser cavity. It is still necessary to have a way of synchronising all the longitudinal modes contributing to the laser electric field $E(t)$ emitted that can be described by

$$E(t) = \sum_{j=1}^{N} exp\left\{i\left[\left(\omega_0 + j\delta\omega\right)t + \phi_j\right]\right\}, \tag{3.2}$$

where ω_0 is the central frequency, $\delta\omega = \frac{2\pi c}{2L}$ is the free-running frequency interval in a cavity of length L, N is the number of modes and ϕ_j is the phase of the oscillation j.

In free-running lasers, the phases of the equally spaced cavity modes can be a set of random numbers, the output intensity is then continuous, as shown on the left on figure 3.7. An infinite series of identical bursts of incoherent light contribute to a noisy behavior of the cavity continuous mode. Forcing the modes to have equal phase, a procedure called mode-locking [100] [101], implies that all these waves add constructively, resulting in equally spaced very intense short bursts of light, as shown on the right on figure 3.7. The ratio between the cavity length and the pulse duration gives the number of modes oscillating in phase. Considering a one meter long cavity emitting $100fs$ pulses the number of modes can get up to 100.000.

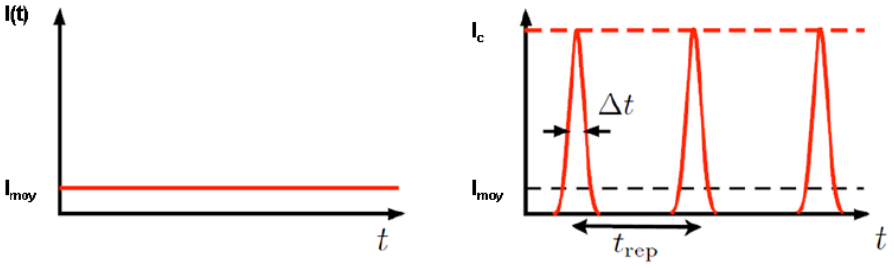

Figure 3.7: Temporal intensity of a continuous laser (left) and a pulsed one (right).

In this scope, there are active and passive mode-locking lasers, that use, respectively an external and an internal modulation. Active mode-locking lasers are based on active

modulation of the intracavity losses or the round-trip phase change via an acousto-optic modulator. If the modulation is synchronized with the cavity round trips, ultrashort laser pulses can be obtained. Intracavity losses contribute to pulse duration broadening. The resulting pulse duration is then achieved in most cases by a balance between this pulse broadening and the pulse shortening, both induced in the cavity. On the other hand, passive mode-locked lasers are based on a saturable absorber inside the laser resonator, responsible for modulating the cavity losses by absorption. This type of mode-locking allows the generation of much shorter pulses because the saturable absorber can modulate the losses much faster than an electronic modulator.

In the passive mode-locked lasers class, we find the Kerr-lens mode-locking laser (KLM) [102], based on the Kerr effect. In the most typical case of a gaussian spatial distribution, with higher intensity in the center of the beam, an index gradient is created in the medium and it acts as a convergent lens. Placing an aperture inside the laser cavity allows to select the high peak power contribution to the spatial distribution reponsible for the Kerr effect and then to achieve the so called self-mode-locking.

3.2.3 Titanium-doped sapphire crystal

The titanium-doped sapphire crystal ($Ti^{3+} : Al_2O_3$, to be called here Ti:sapphire) presents a broad gain bandwidth [103] and, thanks to that, is widely used as a gain medium for solid state lasers, being a great option to replace dye lasers. Discovered by Moulton in 1982 [104] and explored in the later years [105], this material can have more than 50% of overwall power conversion efficiency [106]. It was used for the first time in a self-mode-locked laser in the 1990s [107] when a pulse duration of $60fs$ was obtained.

In 1992, the Kerr lens mode-locking [102] [108] draw the community's attention in the quest for oscillators capable of delivering pulses of shorter duration. The studies led to the development of important techniques still used nowadays as the use of prims and chirped mirrors inside the cavity of femtosecond lasers [109][110].

In the 1990s, the evolution towards shorter pulses continued [111] [112]. In 1999, pulses of less than $6fs$ duration generated with a Ti:sapphire laser had already been reported [113] [114].

Presenting a rhomboedric hexagonal crystal structure, the Ti:sapphire crystal has a very wide emission spectrum when pumped in the $500nm$ range (from $680nm$ to $1100nm$) as shown in figure 3.8. The sapphire matrix allows an exceptional bandwidth thanks to the splitting of the Ti^{3+} ion levels and to the strong electron-phonon coupling. In addition, this type of crystal presents a great thermal conductivity, $k_c = 34W/mK$, what allows temperature dissipation even with high power.

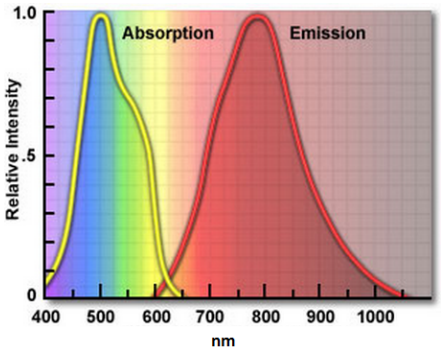

Figure 3.8: Emission and absorption spectra of a Ti:sapphire crystal. Figure from reference [115].

This crystal is then the appropriate choice of gain medium in femtosecond oscillators as well as in amplifying systems.

3.2.4 Amplification

The Ti:sapphire oscillator allows one to have a large bandwidth but not very important energy, pulse energy is in the nJ range. When higher peak power is necessary, several stages of amplification can be used. Some of the results presented in this thesis were obtained using a regenerative amplifying cavity at $5kHz$ repetition rate. This technique of amplification will now be presented in the scope of the chirped pulse amplification.

3.2.4.1 Chirped pulse amplification

The chirped pulse amplification (CPA) is a technique invented in the 1980s by Mourou [116]. It allows amplifying pulses to very high intensities avoiding optical damage of the gain medium due to high peak power of the pulse. In short duration pulses, as seeked here, the peak power can be responsible for nonlinear pulse distortions as self-focusing effects.

The concept of the technique is to temporally strech and chirp the femtosecond oscillator pulse, increase its energy and then recompress it, as shown in figure 3.9.

3.2.4.2 Stretcher and compressor

To stretch and compress the pulse, one usually uses gratings in pairs with a folding mirror at the end. The orientation of the gratings can give rise to stretching or compression.

In the stretcher, represented in figure 3.10, the high frequency components of the spectrum (here represented by the blue lines) follow a longer optical path than the low

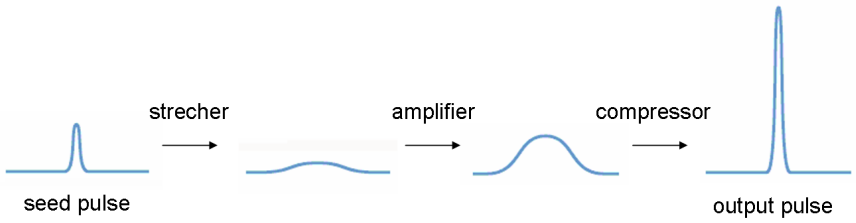

Figure 3.9: Evolution of temporal pulse shape in a chirped pulse amplification.

frequency components (here represented by the red lines), which means it induces positive chirp. Usually, a pulse of a few tens of femtoseconds is stretched up to the 100ps range.

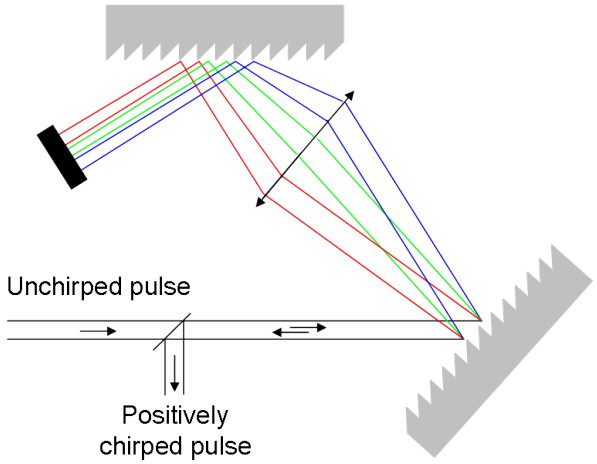

Figure 3.10: Principle of operation of a diffraction gratings stretcher.

The streching is usually done in the Offner all reflective geometry [117] which have proven to be aberration free. This not only prevents from any damage but also minimizes nonlinear optical effects during amplification.

In the compressor configuration, represented in figure 3.11, a negative chirp is induced to recover the initial pulse duration.

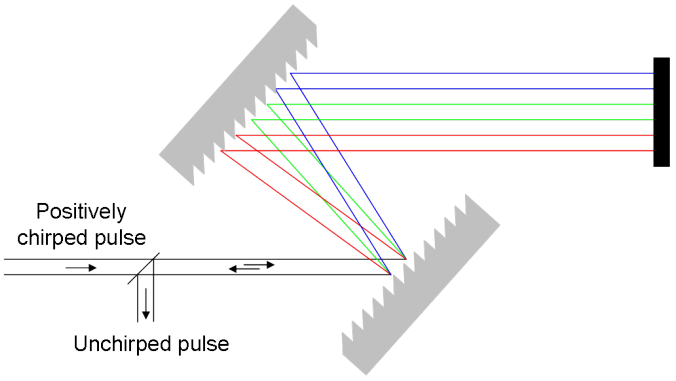

Figure 3.11: Principle of operation of a diffraction gratings compressor.

3.2.4.3 Regenerative cavity

An efficient amplification requires several passes in the gain medium. For that, a cavity is the most indicated configuration for amplifying systems.

The regenerative cavity is based on the energy storage in a gain medium, generally a Ti:sapphire crystal, placed in a closed cavity and pumped at $532nm$. The gain in the cavity can reach up to the 10^6 factor. The repetition rate is determined by the pump laser pulse (duration in the ns range) that needs to be synchronized with the oscilator pulse, here called seed.

In a regenerative cavity [118], the gain medium is placed in a resonator surrounded by two polarizers and two Pockels cells, responsible for controling the input and output times of the pulses. After the seed pulse is coupled into the resonator, the first Pockels cell is switched to rotate the polarization of the seed pulse (depending on the alignement of the Pockels cell, it can act as a quarter or half-waveplate) and it Q-switches the resonator. The pulse circulates in the closed cavity and is continuously amplified. After a certain number of round trips, determined by the energy storage time of the cavity, the gain does not compensate the energy losses, resulting in a gain decrease. A voltage is then applied to the second Pockels cell so the amplified pulse is coupled out of the resonator by reflection on the second polarizer. The delay of the second Pockels cell is chosen so the extraction is performed at maximum gain. A scheme of the functioning of the regenerative amplifier can be seen in figure 3.12.

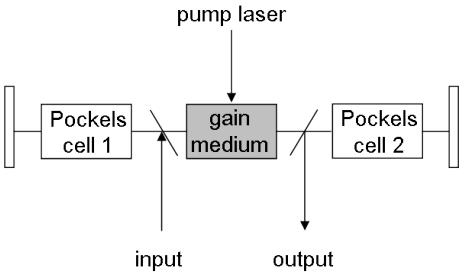

Figure 3.12: Schematic set-up of a regenerative amplifier.

3.3 Dispersion compensation

Even if the amplified pulse has an optimal duration at the output of the CPA system due to the gratings compressor, pre-compensation of dispersion induced by different optical elements in the pump and probe set-up and by air can be necessary as the second and third order dispersion can be of great importance in the MO-FWM signals (shown in section 1.3.3). This is the case for the very large bandwidth pulses used in a part of the experiments of this thesis.

For that, one can use different compression schemes, as the prisms and the chirped mirrors, to be explored ahead.

3.3.1 Prisms

This type of optical elements adds, mostly but not only, second order negative phase to the pulse. Dispersion through the prisms deviates spatially more the blue than the red components of the light. With that, in the second prism, the red propagates through more glass than the blue. The second passage in the prisms (done using a folding mirror after the second prism) doubles this effect and recombines the previously spatially dispersed beam, as shown in figure 3.13.

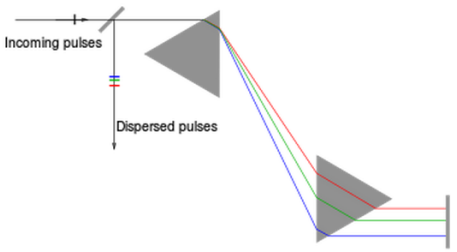

Figure 3.13: Scheme of a prism compressor.

This type of compression offers a very important feature that is the possibility of spectrum selection (by placing a selective slit after the first passage in the prisms). This allows better compression in case of large spectrum bandwidth by cutting extreme parts of the spectrum that are difficult to compensate due to nonlinear processes of spectral broadening.

Keeping the prisms at their minimum deviation angle and Brewster's angle at each surface (ideally, the prism is cut so they are the same) and keeping the entrance face of the second prism parallel to the exit face of the first prism allow one to have negative dispersion.

The group velocity dispersion constant is given by [119]

$$D = -L^{-1}\frac{dT}{d\lambda} = \frac{\lambda}{cL}\frac{d^2P}{d\lambda^2}, \tag{3.3}$$

where L is the physical lenght of the path, $P(\lambda)$ is the optical path and T is the time taken by the light pulse to propagates through the path P.

To obtain $d^2P/d\lambda^2$, one must consider a ray propagating at an angle β near the apices of the prisms, as shown in figure 3.14.

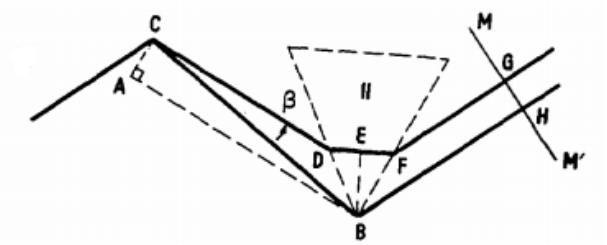

Figure 3.14: Angle of propagation through a prims compressor. Point C is the apex of the first prism. Figure from reference [120].

The total optical path is then given by $P = 2Lcos(\beta)$.

Derivating that with respect to λ and considering a prism with index n, it is possible to obtain that [120]

$$\frac{d^2P}{d\lambda^2} = 4L\left\{\left[\frac{d^2n}{d\lambda^2} + \left(2n - \frac{1}{n^3}\right)\left(\frac{dn}{d\lambda}\right)^2\right] sen\beta - 2\left(\frac{dn}{d\lambda}\right)^2 cos\beta\right\}. \tag{3.4}$$

As β is of the order of the angular deviation of the ray bundle, $sin\beta \ll cos\beta$. Using the same principle, it is also possible to obtain the group delay dispersion [121], given by

$$GDD_{prism} \approx \frac{\lambda^3}{2\pi c^2}\left\{-4L\left[2\left(\frac{dn}{d\lambda}\right)^2\right] + 4\left(\frac{dn^2}{d\lambda^2}\right)\left(2D_{\frac{1}{2}}\right)\right\}, \tag{3.5}$$

where the first term is always negative and depends on the prism separation and the second term is always positive and depends on the pathlength through the prisms. This way it is possible, by controlling the prisms separation and the quantity of glass crossed by the beam, to control the dispersion introduced by them.

The values of the first and second derivate of the refractive index with respect to the wavelength are intrinsic to each material and each wavelength and can be obtained from the Cauchy relations as follows

$$n(\lambda) = A + \frac{B}{\lambda^2} + \frac{C}{\lambda^4}, \tag{3.6}$$

where A, B and C are tabulated and can be found in reference [122], for example.

3.3.2 Chirped mirrors

First explored in 1994 [109], the chirped mirror, a type of dieletric mirror, is manufactured so that each wavelength penetrates to a different extent into the mirror multilayer structure and, thus, experiences a different group delay, as shown in figure 3.15.

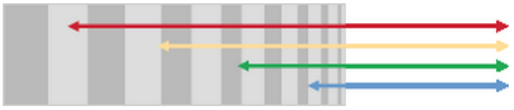

Figure 3.15: Principle of operation of a chirped mirror.

In the case of few cycles pulses, these mirrors have to compensate finely the dispersion over hundreds of nanometers. In reference [109], the $TiO_2 - SiO_2$ multilayer mirror has a nominal GDD of $-45fs^2$ at $800nm$, as the ones used in the experiments of this thesis. They were used combined with a pair of glass wedges, to control the compensation.

3.4 Ultrashort pulses characterization

Measuring ultrashort dynamics requires knowing the characteristics of the used pulses, like their temporal amplitude and phase profiles, which can be done using correlation techniques based on the nonlinear interaction of two pulses with a medium. When the nonlinear

medium transient response is much shorter than the pulse duration, this technique can be used for pulse characterization. A useful technique is the interferometric autocorrelation. We have used an interferometric commercial autocorrelator named Femtometer that functions with a $25\mu m$ BBO crystal and performs fringe-resolved autocorrelation (FRAC) measurements [123].

Femtometer is a Michelson interferometer based autocorrelator, where a beam is split in two. Each of these beams travels different paths, being one of these paths variable with a piezo actuator. They are then colinearly recombined in a nonlinear crystal where the second harmonic generation takes place. The outcoming beam presents an interferometric structure that depends on the relative delay between the two pulses. This beam is then measured in a photo multiplier and the duration of the pulse is estimated in real time by counting the number of fringes. The duration of a single fringe is estimated thanks to a first measurement of the spectrum.

The field that arrives in the photo multiplier contains then three components: the two incident fields and the sum frequency of both fields. The signal in the photomultiplier is given by

$$S(\tau) \propto \int |E_2(t,\tau)|^2 dt \propto \int |E(t) + E(t-\tau)|^4 dt, \tag{3.7}$$

where $E_2(t,\tau)$ is the second harmonic field and $E(t)$ and $E(t-\tau)$ are the two incoming beams.

The reconstruction of the interferogram trace allows the recovery of the spectral phase, as well. Among other methods that also give access to the spectral phase are the Frequency-Resolved Optical Gating (FROG) [124] and the Spectral Phase Interferometry for Direct Electric-Field Reconstruction (SPIDER) [125]. One major advantage of these complete methods is that they immediately reveal what kind of distortion causes the temporal broadening of the pulse.

The FROG technique uses any instanteneous nonlinear effect and is based on the spectral characterization of the signal generated as a function of the delay between the two pulses interacting in the nonlinear medium, with no need of a reference pulse. Using the appropriate phase retrieval concepts, it allows obtaining the phase and the intensity of the pulse.

The SPIDER technique, a self-referencing technique that is a version of the spectral shear interferometry [126], is based on the spectral interferogram of two replicas of the pulse to be characterized shifted in frequency. The optical spectrum of the sum frequency signal reveals then the temporally resolved group delay.

While FROG requires a sophisticated iterative algorithm for retrieving the spectral

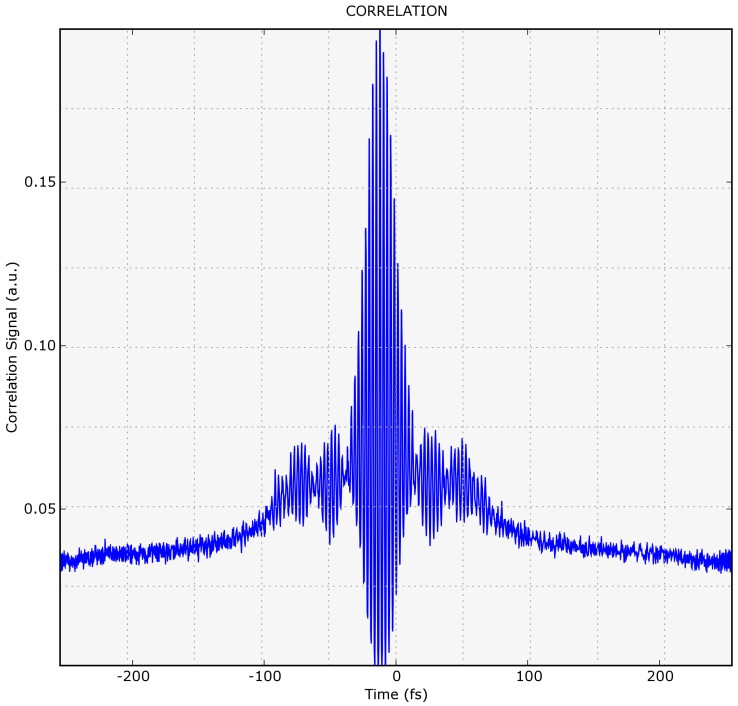

Figure 3.16: Example of FRAC trace of a negatively chirped pulse obtained with a spectrum centered at $810nm$ with FWHM of $110nm$. The duration is $18fs$.

phase, SPIDER has a simple one. However, the FROG algorithm delivers aditional consistency checks. FROG is more convenient for long pulses since SPIDER requires a spectrometer with high resolution and an optical element with a huge amount of chromatic dispersion.

A comparison study of different characterization techniques can be found in reference [80].

The FRAC trace shows if the pulse is chirped or not, but does not quantify it (to do it, one must rebuilt the trace in an iterative algorithm with an initial guess of the spectral phase). If the pulse is chirped, which means, if it presents second and third order dispersion, the interferometric autocorrelation trace presents wings, as shown in figure 3.16. The trace of the same pulse with some of the negative dispersion compensated by glass is shown in figure 3.17.

3.5 Magneto-optical four-wave mixing configurations

We have so far described the general aspects of femtosecond pulse generation, amplification, dispersion control and ultrashort pulses characterization. Using these concepts we

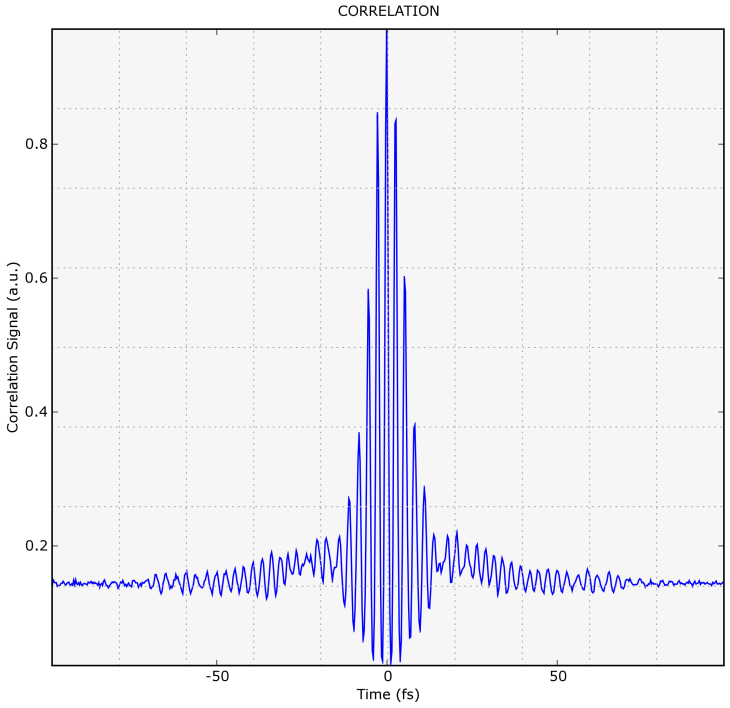

Figure 3.17: Example of FRAC trace of a chirped pulse obtained with a spectrum centered at $810nm$ with FWHM of $110nm$. The duration is $6fs$. This trace was obtained by adding $8mm$ of fused silica to the beam used to generate the trace shown in figure 3.16.

present now the laser systems and the set-ups used to measure the MO-FWM and Faraday signals. For each configuration, we present the laser system, the set-up and the analysis technique used (polarization bridge or crossed polarizers).

In all configurations, in order to recover the variation of the polarization, we have used lock-in amplifiers and a mechanical chopper in the pump beam. The lock-in is responsible for measuring the variation of the signal at the chopping frequency ($217Hz$). The intensity of signal (transmission T or reflection R) is defined as a function of the intensity of the signal in the presence of the pump and probe beams $I_{SP}(t)$ (when the chopper does not block the beam) and the intensity of the signal in absence of the pump I_S (when the chopper blocks the beam), as follows.

$$I(t) = \frac{\Delta I_{ps}(t)}{\Delta s(t)} = \frac{I_{ps}(t) - I_s(t)}{I_s(t)},\ I = T, R \tag{3.8}$$

Let us emphasize that a photoelastic modulation instead of a slower mechanical modulation could have been used. However, the scattering of light in the detectors appeared to be a major drawback.

3.5.1 Two-beam configuration

3.5.1.1 Laser system

For the first part of the results presented in this thesis, we have used a Ti:sapphire laser system (oscillator and amplification gain medium), with $5kHz$ of repetition rate that delivers pulses with $120fs$ duration and central wavelength at $794nm$.

The commercial Spectra Physics oscillator of the system is a Ti:sapphire one, named Tsunami, pumped by a continuous laser named Millenia, based on a $NdYVO_4$ crystal. Millenia's output is at $532nm$ and $5W$. This output pumps the Ti:sapphire crystal on Tsunami, that is responsible for delivering pulses at $800nm$ with $80fs$ duration at $82MHz$ of repetition rate with an average power of $600mW$. The energy per pulse is then $7,3nJ$ and the full width at half maximum (FWHM) is $40nm$.

As said in section 3.2.4, higher energies per pulse mean more important effects. For that, a CPA system is then used. The commercial Spectra Physics regenerative amplifier named Spitfire, which gain medium is also a Ti:sapphire crystal, is pumped by another pulsed laser named Evolution X, from Coherent. Evolution X is a neodymium-doped yttrium lithium fluoride (Nd:YLF) laser based on the $LiYF_4$ crystal that delivers $200ns$ pulses at $5KHz$ and $527nm$ with a power of $11,5W$.

After being stretched, amplified and recompressed, as explained in section 3.2.4, the

system delivers pulses that have now $0,2mJ$ per pulse and $120fs$ of duration. Its schematic set-up is shown in figure 3.18.

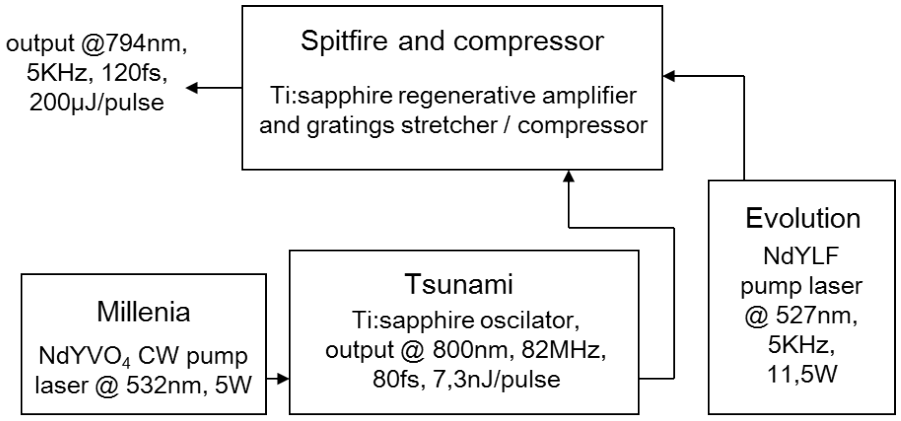

Figure 3.18: Scheme of the system used in the two-beam configuration.

3.5.1.2 Set-up

We have used the pulses described above in a classical pump and probe experiment. The pump pulse was delayed with the help of a stepper motor and the pump beam was modulated by a mechanical chopper that fed a lock-in amplifier for the detection. The schematic set-up for the focalization of the two beams propagating along $\overrightarrow{k}_s$ and $\overrightarrow{k}_p$ and detection is shown in figure 3.19. An external static magnetic field H_{ext} is applied. The Faraday signal is detected in the direction $\overrightarrow{k}_s$ and the MO-FWM in the direction $2\overrightarrow{k}_p - \overrightarrow{k}_s$.

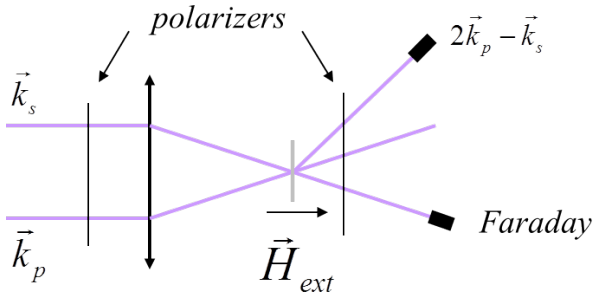

Figure 3.19: Experimental configuration for the two-beam MO-FWM experiments.

The polarization analysis is performed via the crossed polarizers technique, to be describe in the following section.

3.5.1.3 Analysis - crossed polarizers

The crossed polarizers technique is based on the polarization analysis of the probe beam before and after crossing the sample. It consists in placing a linear polarizer before the sample, in order to well define the probe polarization axis, and in rotating of an angle α (with respect to the crossed orientation) a second polarizer after the sample, called analyzer, in order to scan the polarization state of the emerging beam [127]. This technique allows obtaining the rotation and ellipticity of a signal simultaneously.

Static case

The expression for the intensity of the signal that reaches the photodiode after crossing the two polarizers and the sample, for two opposite directions of the external magnetic field $H_{ext\pm}$ is given, for small α, by [127]

$$I_{\pm} = I_0 \left[\alpha^2 - 2\alpha\left(\theta_0 \pm \theta_M\right) + \left(\theta_0^2 + \eta_0^2 + \theta_M^2 + \eta_M^2\right) \pm 2\left(\theta_0\theta_M + \eta_0\eta_M\right)\right], \tag{3.9}$$

where I_0 is the intensity measured with the analyzer parallel to the polarizer, θ_0 and η_0 are the nonmagnetic rotation and ellipticity induced by the sample and θ_M and η_M are the magneto-optical rotation and ellipticity. From that, one is able to define the quantity R, given by

$$R = \frac{I_{+M} - I_{-M}}{4I_0} = -\alpha\theta_M + \theta_0\theta_M + \eta_0\eta_M. \tag{3.10}$$

Varying α for the measurements (as a function of the pump and probe delay or in the static case) for two opposite external field directions and fitting the resulting curves allows obtaining θ_M and η_M.

Dynamic case

The analyzed intensity as a function of α gives two parabolas for the two external field directions. In the dynamic case, each delay presents a pair of parabolas and their evolution is obtained with all the delays. Equation 3.10 is then written as

$$R(\tau) = \frac{I_{+M}(\tau) - I_{-M}(\tau)}{4I_0(\tau)} = -\alpha\theta_M(\tau) + \theta_0\theta_M(\tau) + \eta_0\eta_M(\tau). \tag{3.11}$$

With that, one sees that R has a linear behavior with respect to α for a fixed pump and probe delay. All the lines for all the delays cross the abscissa $R = 0$ at the same point only if the variations in the rotation and in the ellipticity are identical.

3.5.2 Three-beam configuration

3.5.2.1 Laser system

The three-beam configuration experiments were performed using shorter pulses than the ones used in the two-beam configuration. The system that delivers such pulses is similar to the system presented in section 3.5.1.1. A Spectra Physics oscillator named Tsunami based on a Ti:sapphire crystal, pumped by a continuous laser named Millenia ($532nm$ and $5W$, described earlier) delivers pulses centered at $800nm$ with a bandwidth of $40nm$ at a repetition rate of $82MHz$ and $5,9nJ$ per pulse. This pulse is then amplified in a commercial Spectra Physics regenerative cavity, named Spitfire (also described earlier), pumped now by a pulsed laser named Empower. After compression, the output pulse has $47fs$ and is centered at $800nm$ with a repetition rate of $5KHz$ and $0,36mJ$ energy per pulse.

3.5.2.2 Set-up

The three-beam configuration considers three incident beams propagating along k_a, k_b and k_c directions, and two different delays, τ (between pulses a and c) and T (between pulses b and c), as shown in figure 3.20.

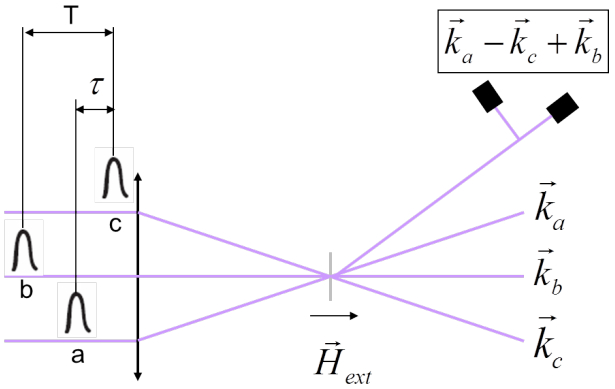

Figure 3.20: Experimental configuration for the three-beam MO-FWM experiments.

An external magnetic field perpendicular to the sample plane is applied. The signals generated in the directions $k_a - k_c + k_b$ were detected with the help of a polarization bridge, to be presented in the next section.

3.5.2.3 Analysis method - polarization bridge

The polarization bridge method consists in separating the two tranverse components of the incident electric field after it has been projected on a referential frame turned by 45° with respect to the incident referential frame (one of the axis being the direction of polarization of the incident beam) and detecting separately both polarization components. In practice, one detects the difference between these two components, synchronously with the modulated pump beam (or with one of the three beams in the three-beam MO-FWM configuration).

Let us describe further this measurement procedure. The probe beam polarization is well defined before the sample with a polarizer and the analysis of the probe beam after the sample is done with the help of a waveplate, that is responsible for retarding one of the components of the polarization of a given delay in π [81], a polarizing cube and two photodiodes. The polarizing cube, as well as the Wollaston prism, separates the tranverse components of the field. It reflects one component of the polarization at the interface of two orthogonal prisms cemented together at their base and transmits the other. The angle between reflected and transmitted beams is 90°, while for the Wollaston prism, the angle is defined by the apex angle of both prisms at the interface and can vary from a few minutes to 45°.

In order to increase the sensitivity of the device, one must use a waveplate to prepare the polarization of the beam before analysis. For example, a polarizing cube analysis with an incident linearly horizontaly polarized beam will provide low sensitivity of the variation of the beam polarization. The photodiode in one of the arms of the bridge will receive almost all the signal and the other, a projection of the small variation. The used method is then to turn the polarization to an axis that will allow the equilibrium of the two arms. This is done with the help of a half-waveplate, aligned with one of its birefringent axis making an angle of $22,5°$ with respect to the plane of polarization so that the incident polarization is rotated of 45°. In the case of a horizontal incident polarization, this 45° rotation will provide equilibrated signals in both photodiodes. A small variation of the rotation can then be precisely measured as the difference between both arms.

To measure the ellipticity of the polarization, one must add a quarter-waveplate to the configuration describe above. This plate is placed with an angle 0° with respect to its axis. The combination of the half and quarter-waveplates and a polarizing or Wollaston cube allows obtaining the ellipticity.

The static case description of how to obtain rotation and ellipticity from the signal measured in these two configurations is made in appendix A. The dynamic case is described hereafter.

Dynamic case - Faraday configuration

To understand how the rotation and the ellipticity of a field evolve in time in a pump and probe experiment, the static field definition established in equation A.1 (in appendix A) is not complete. One must describe the time dependent field, as presented in section 2.2.3.

Once more, it is possible to use the Jones formalism to study the magneto-optical response of the medium in terms of the rotation and ellipticity of the field.

As defined in equation 2.21, the intensity of the emitted field in the probe direction is the sum of the first and third order fields. In the Jones formalism, one can write

$$\overrightarrow{E}^{(1)}(t) = \begin{pmatrix} E_x^{(1)}(t) \\ E_y^{(1)}(t) \end{pmatrix} \text{ and } \overrightarrow{E}^{(3)}(t,\tau) = \begin{pmatrix} E_x^{(3)}(t,\tau) \\ E_y^{(3)}(t,\tau) \end{pmatrix} \tag{3.12}$$

while, being α the rotation and ε the ellipticity, one has [83]:

$$\overrightarrow{E} = \begin{pmatrix} cos(\alpha)cos(\varepsilon) - isin(\alpha)sin(\varepsilon) \\ sin(\alpha)cos(\varepsilon) + icos(\alpha)sin(\varepsilon) \end{pmatrix}. \tag{3.13}$$

With that, considering that the emitted field $\overrightarrow{E}^{(1)}(t)$ has ellipticity $\varepsilon_S(t)$ and is rotated of an angle $\alpha_S(t)$ and that the emitted field $\overrightarrow{E}^{(3)}(t,\tau)$ has ellipticity $\varepsilon(t,\tau)$ and is rotated of an angle $\alpha(t,\tau)$, one can write

$$\overrightarrow{E}^{(1)}(t) = \begin{pmatrix} E_x^{(1)}(t) \\ E_y^{(1)}(t) \end{pmatrix} = E^{(1)}(t) \begin{pmatrix} cos[\alpha_S(t)]cos[\varepsilon_S(t)] - isin[\alpha_S(t)]sin[\varepsilon_S(t)] \\ sin[\alpha_S(t)]cos[\varepsilon_S(t)] + icos[\alpha_S(t)]sin[\varepsilon_S(t)] \end{pmatrix} \tag{3.14}$$

$$\overrightarrow{E}^{(3)}(t,\tau) = \begin{pmatrix} E_x^{(3)}(t,\tau) \\ E_y^{(3)}(t,\tau) \end{pmatrix} = E^{(3)}(t,\tau) \begin{pmatrix} cos[\alpha(t,\tau)]cos[\varepsilon(t,\tau)] - isin[\alpha(t,\tau)]sin[\varepsilon(t,\tau)] \\ sin[\alpha_(t,\tau)]cos[\varepsilon(t,\tau)] + icos[\alpha(t,\tau)]sin[\varepsilon(t,\tau)] \end{pmatrix}. \tag{3.15}$$

As shown before, to obtain the rotation and the ellipticity from a pump and probe measurement using a polarization bridge, one must use at first, a half-waveplate and then a combination of the same half-waveplate with a quarter wave plate, respectively. With the Jones matrix of the half-waveplate, one finds the emitted fields $\overrightarrow{E}^{(1)\prime}$ and $\overrightarrow{E}^{(3)\prime}$ to obtain the rotation, as follows.

$$\overrightarrow{E}^{(1)\prime}(t) = \begin{pmatrix} E_x^{(1)\prime}(t) \\ E_y^{(1)\prime}(t) \end{pmatrix} = M\left(\pi, \frac{\pi}{8}\right) \begin{pmatrix} E_x^{(1)}(t) \\ E_y^{(1)}(t) \end{pmatrix} \tag{3.16}$$

$$\overrightarrow{E}^{(3)\prime}(t,\tau) = \begin{pmatrix} E_x^{(3)\prime}(t,\tau) \\ E_y^{(3)\prime}(t,\tau) \end{pmatrix} = M\left(\pi, \frac{\pi}{8}\right) \begin{pmatrix} E_x^{(3)}(t,\tau) \\ E_y^{(3)}(t,\tau) \end{pmatrix} \tag{3.17}$$

With the product of the Jones matrices of the half-waveplate and quarter-waveplate, one finds the emitted fields $\overrightarrow{E}^{(1)\prime\prime}$ and $\overrightarrow{E}^{(3)\prime\prime}$ to obtain the ellipticity.

$$\overrightarrow{E}^{(1)\prime\prime}(t) = \begin{pmatrix} E_x^{(1)\prime\prime}(t) \\ E_y^{(1)\prime\prime}(t) \end{pmatrix} = M\left(\pi, \frac{\pi}{8}\right) M\left(\frac{\pi}{2}, 0\right) \begin{pmatrix} E_x^{(1)}(t) \\ E_y^{(1)}(t) \end{pmatrix} \tag{3.18}$$

$$\overrightarrow{E}^{(3)\prime\prime}(t,\tau) = \begin{pmatrix} E_x^{(3)\prime\prime}(t,\tau) \\ E_y^{(3)\prime\prime}(t,\tau) \end{pmatrix} = M\left(\pi, \frac{\pi}{8}\right) M\left(\frac{\pi}{2}, 0\right) \begin{pmatrix} E_x^{(3)}(t,\tau) \\ E_y^{(3)}(t,\tau) \end{pmatrix} \tag{3.19}$$

As for equations A.9 and A.16, it is possible to write an expression for the magneto-optical signal measured in the Faraday configuration in the direction of the probe beam as follows. H_{ext} was replaced by H for simplicity.

$$\begin{aligned} S_{MO}^{ROT}(\tau) &= \left[S_{H+}^{ROT}(\tau) - S_{H-}^{ROT}(\tau)\right] / S_{MO}^{ROT} \\ &= \left[\Delta I'_{H+}(\tau) - \Delta I'_{H-}(\tau)\right] / S_{MO}^{ROT} \\ &= \left\{[I'_x(\tau) - I'_y(\tau)]_{H+} - [I'_x(\tau) - I'_y(\tau)]_{H-}\right\} / S_{MO}^{ROT} \end{aligned} \tag{3.20}$$

$$\begin{aligned} S_{MO}^{ELL}(\tau) &= \left[S_{H+}^{ELL}(\tau) - S_{H-}^{ELL}(\tau)\right] / S_{MO}^{ELL} \\ &= \left[\Delta I''_{H+}(\tau) - \Delta I''_{H-}(\tau)\right] / S_{MO}^{ELL} \\ &= \left\{[I''_x(\tau) - I''_y(\tau)]_{H+} - [I''_x(\tau) - I''_y(\tau)]_{H-}\right\} / S_{MO}^{ELL} \end{aligned} \tag{3.21}$$

where the static rotation S_{MO}^{ROT} and the static ellipticity S_{MO}^{ELL} are given by

$$S_{MO}^{ROT} = S_{H+}^{ROT} - S_{H-}^{ROT} = \Delta I'_{H+} - \Delta I'_{H-} = (I'_x - I'_y)_{H+} - (I'_x - I'_y)_{H-} \text{ and} \tag{3.22}$$

$$S_{MO}^{ELL} = S_{H+}^{ELL} - S_{H-}^{ELL} = \Delta I''_{H+} - \Delta I''_{H-} = (I''_x - I''_y)_{H+} - (I''_x - I''_y)_{H-}, \tag{3.23}$$

obtained in the appendix A. The intensities are given by equation 2.21.

Dynamic case - Magneto-optical four-wave mixing configuration

The field emitted in the FWM directions does not contain the linear electric field. This means its intensity is obtained as shown in equations 2.23 and 2.24.

In this case, the signal does not exist when one of the beams is blocked, which avoids the normalization via a static value as shown in equations 3.20 and 3.21. However, we can still use the same principle of extraction of the magnetic field dependend signal to obtain the MO-FWM signal, as follows

$$\begin{aligned} S_{MO}^{ROT;FWM}(\tau) &= \left[S_{H+}^{ROT;FWM}(\tau) - S_{H-}^{ROT;FWM}(\tau)\right] \\ &= \left[\Delta I_{H+}^{\prime FWM}(\tau) - \Delta I_{H-}^{\prime FWM}(\tau)\right] \\ &= \left\{[I_x^{\prime FWM}(\tau) - I_y^{\prime FWM}(\tau)]_{H+} - [I_x^{\prime FWM}(\tau) - I_y^{\prime FWM}(\tau)]_{H-}\right\} \end{aligned} \quad (3.24)$$

$$\begin{aligned} S_{MO}^{ELL;FWM}(\tau) &= \left[S_{H+}^{ELL;FWM}(\tau) - S_{H-}^{ELL;FWM}(\tau)\right] \\ &= \left[\Delta I_{H+}^{\prime\prime FWM}(\tau) - \Delta I_{H-}^{\prime\prime FWM}(\tau)\right] \\ &= \left\{[I_x^{\prime\prime FWM}(\tau) - I_y^{\prime\prime FWM}(\tau)]_{H+} - [I_x^{\prime\prime FWM}(\tau) - I_y^{\prime\prime FWM}(\tau)]_{H-}\right\} \end{aligned} \quad (3.25)$$

These equations are valid in the two-beam configuration. In the three-beam configuration, there are two cases: when the delay T is fixed, the signals are given by equations 3.24 and 3.25; when the delay τ is fixed, the signals are given by analogous equations that are T dependent.

3.5.3 Few-cycle pulses two-beam configuration

3.5.3.1 Laser system

To optimize the pulse duration and perform new experiments, we have developped a new set-up based on a commercial Femtolaser Ti:sapphire oscillator named Rainbow and on the control of the temporal pulse characteristics. In the oscillator, the thin crystal is highly doped and the mode-locking is done by an external element that perturbes once an internal element, one of the cavity mirrors. This way it is not necessary to use a modulator, nor an absorber.

It delivers $10fs$ pulses at $80MHz$ repetition rate centered aound $800nm$ with FWHM of $110nm$ what gives a $2,8nJ$ energy per pulse ($230mW$ at the output) pumped by a diode pumped Coherent Verdi laser at $5,45W$ ($532nm$).

The intra-cavity mirrors are chirped multi-layer dielectric ones designed to control the

group delay dispersion and to allow the self-phase modulation in the Ti:sapphire crystal. This effect is responsible, at high crystal doping rates, of such a large bandwidth emission. A picture with the path of the beam inside the cavity in figure 3.21.

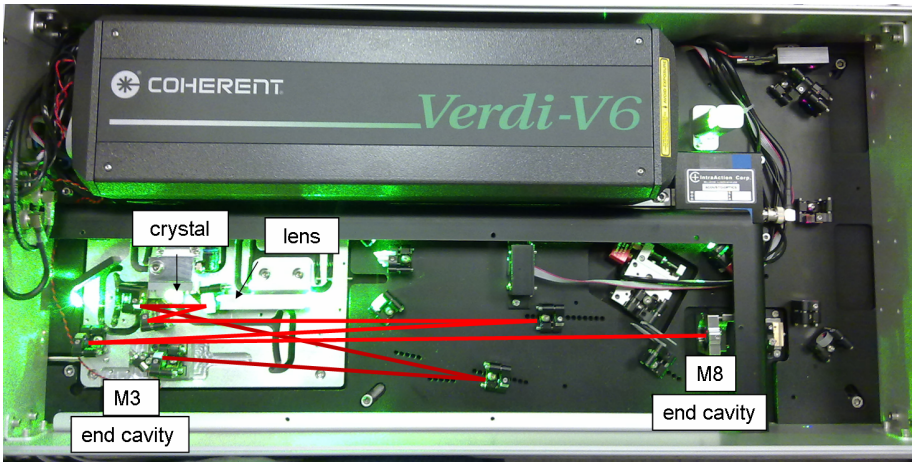

Figure 3.21: Scheme of the Rainbow oscillator.

The output spectrum and output correlation trace of Rainbow are shown in figure 3.22.

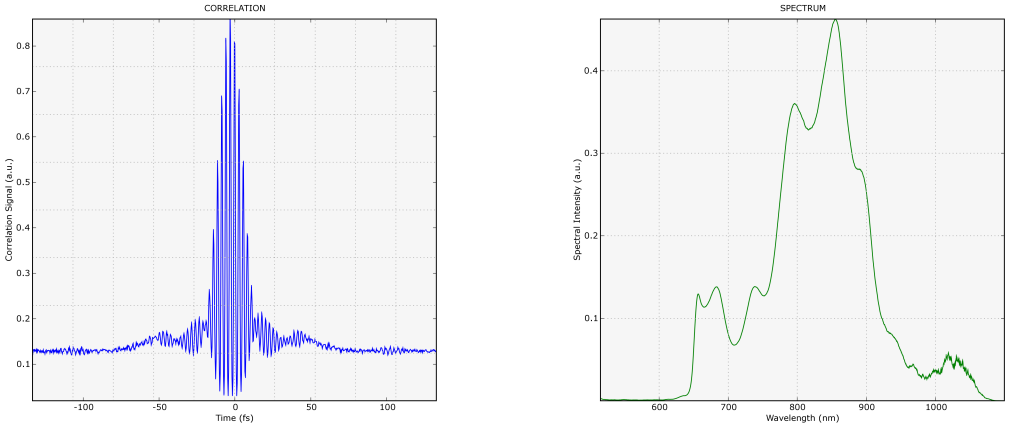

Figure 3.22: Output correlation trace (left) and spectrum (right) of Rainbow pulses. The pulse is $10,4fs$ long and the spectrum, centered at $826nm$, presents FWHM of $129nm$ and FTL of $4,6fs$. The correlation trace on the left shows wings, what indicates chirp. In this case, the chirp was arranged to be negative at the output of the oscillator to start the pre-compensation of the set-up dispersion.

3.5.3.2 Set-up

We have used the pulses delivered by the Rainbow oscillator in a degenerated (at $800nm$) pump and probe experiment. A static magnetic field H_{ext} is applied perpendicular to the sample. The Faraday and MO-FWM analysis (in the direction $2\overrightarrow{k}_p - \overrightarrow{k}_s$ and $2\overrightarrow{k}_s - \overrightarrow{k}_p$) was made via the polarization bridge technique. The general set-up used is presented in figure 3.23.

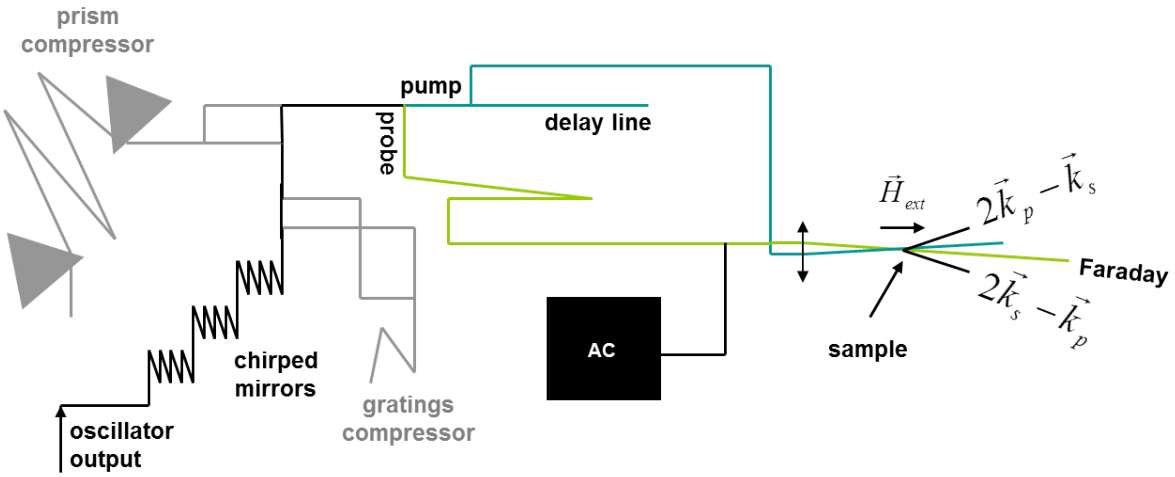

Figure 3.23: Set-up used for the two-beam few-cycle MO-FWM experiments.

The great chalenge in setting up an experiment in such ultrashort time scales is keeping the pulse duration through the set-up. Dispersion in reflective optics and propagation in air and glass must be considered. As we present ahead, the careful choice of optics and the pre-compensation of dispersion are necessary as well as the techniques to keep the short temporal resolution of acquisition.

Large bandwidth response - beam splitter

The reflectance of the beam splitters used in the set-up are adapted to the large bandwidth of our source. However, their effects on the beams spectra are still visible. Figure 3.24 shows the reflectance curve of the beam splitter used to separate the pump and the probe beams and 3.25 shows their spectra, used to do the measurements showed in section 4.2.1 and measured just before the sample. This last one shows as well the ratio between the spectra that is of same shape of the reflectance curve of the beam splitter and emphasizes the sensitivity of the spectrum even to adapted optics.

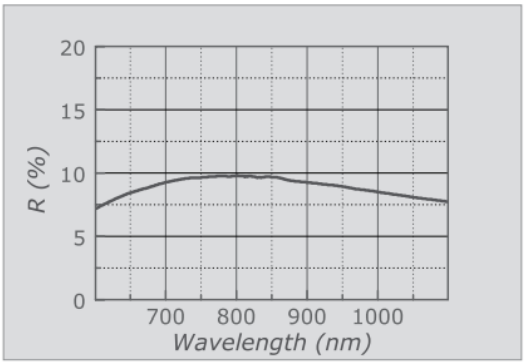

Figure 3.24: Reflectance curve of the beam splitter $OA078$ from Femtooptics (curve from the catalog version of 2014).

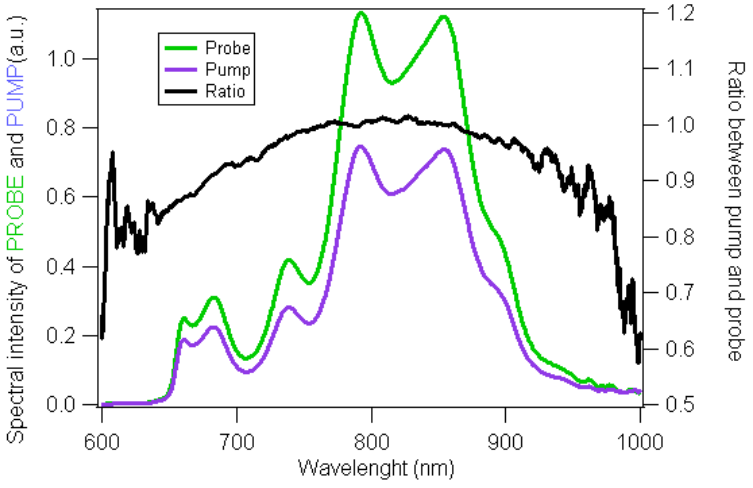

Figure 3.25: Pump and probe spectra and the ratio between them.

This change in the spectrum amplitude of pump and probe shows the importance of minimizing the quantity of reflective optics in the beam path.

Dispersion control - adapted optics

Every milimeter of glass crossed by the beam can also bring undesired effects on the spectral phase of the pulses. The beam splitters described here are only $1mm$ thick to minimize this dispersion in the glass substrate. We have also chosen to use low GDD over large bandwidth mirrors ($< 5fs^2$). The lens that focuses both beams in the sample was carefully chosen for being thin and for not presenting a great change in the glass thickness in its surface. A beam with a given diameter crossing a lens with variable thickness can present variable dispersion along its diameter and therefore chromatic aberration.

Compression - prisms and chirped mirrors

Minimizing the dispersive elements is not always possible like for the lens and the beam-splitters. To pre-compensate these elements and make sure the pulse duration is optimal at the sample, we have tried to use a prims compressor, described in sections 3.3.1. The use of fused silica prisms is important to allow the selection of spectrum. However, the large spectrum delivered by the Rainbow oscillator derails the good prediction of the dispersion introduced by the prisms, as the wavelength distribution is important. With that, a difficult experimental compromise between the compression and third order dispersion brought by the prisms has to be found. Another important compromise, imposed by the size of the prism face, is that the distance between prisms must not be very large considering that the beam shows a spatial dispersion and may be cut by the second prism. This fact limits the distance between prisms. These limitations motivated the use of Femtooptics chirped mirrors that compensate $45fs^2$ per bounce (we have used 12 bounces) and are adapted to a bandwidth from $620nm$ to $920nm$.

Another compression stage that could have been helpful is the diffraction gratings compressor, that unfortunately presented a great power loss. Each grating we tried to use showed a maximum of 60% efficiency. Considering two bounces on each, there was an important power loss of more than 85% that ruled out its use. This loss was probably due to the blazing angle of the gratings, not designed for the $800nm$ range.

Time resolution in the acquisition - stepper motor angle and beam splitters

The features described so far allowed us to have short pulses with low dispersion effects

at the place of the sample to generate the effects we are interested in. It is then of extreme importance to have the good time resolution to measure these phenomena. The stepper motors that are usually found in pump and probe experiments present minimum step of $0,1\mu m$, what gives a time step of $0,6fs$. As the pulse duration is in the $10fs$ range and the signals produced by its interaction with the garnet are expected to be in this time range, the signals generated would not be well sampled with the regular use of such a motor. The stepper motor was then placed at an angle with respect to the incident beam, this way, the step along the beam direction is shorter.

The angle of the motor implies the use of a zero degree mirror on it, instead of a retroreflector mirror, as usual. This way, the beam is not deviated with the motor movement. In this configuration, it is then necessary to use a second beam splitter, in addition to the one used to separate the pump and probe beams, in order to recover the pump beam from the delay line, as it propagates along the input beam. This is done using a 50% beam splitter, what causes power loss. The use of this configuration affects then the choice of the pump and probe separation beam splitter. It was chosen in order to have the pump and probe beams with approximatively the same power, when the pump is chopped, to optimize the MO-FWM signals. The areas of the set-up with the beam splitters and the zero degree mirror and with the zero stepper motor are ilustrated in figures 3.26 and 3.27.

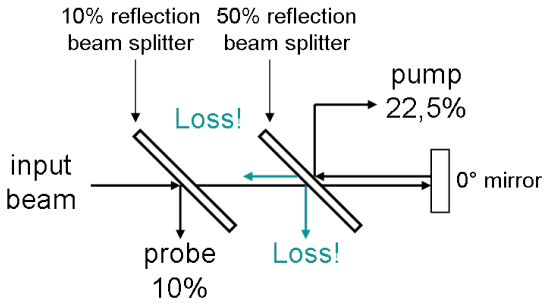

Figure 3.26: Scheme of the delay line - zero degree mirror and 10% and 50% beam splitters used.

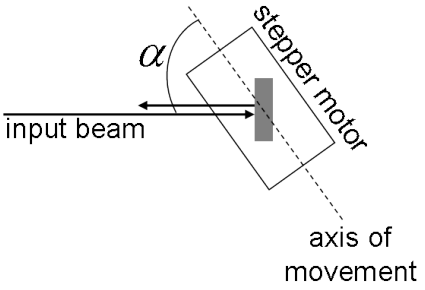

Figure 3.27: Scheme of the angle α used between the axis of movement of the stepper motor and the input and output beam axis.

Having an angle α for the stepper motor means having a new time scale to be calibrated. As the pump and probe beams have the same wavelength, fringes generated in the sample signal, an artefact of the experiment, were first used to calibrate the new stretched time scale and then minimized with the help of a piezo motor placed to tap the last mirror in the pump path (the effect of the piezo motor is shown in figure 3.28). Knowing that for light centered at $800nm$ the optical cycle should be $2,6fs$, one finds α and the factor to

calibrate the new scale using the fringes measured as if the pump and probe experiment was an interferometer.

This factor was usually found to be between 5 and 6 for different configurations (α between 78° and 80°), what allowed us to have time resolution of the order of 200 attoseconds for the data acquisition.

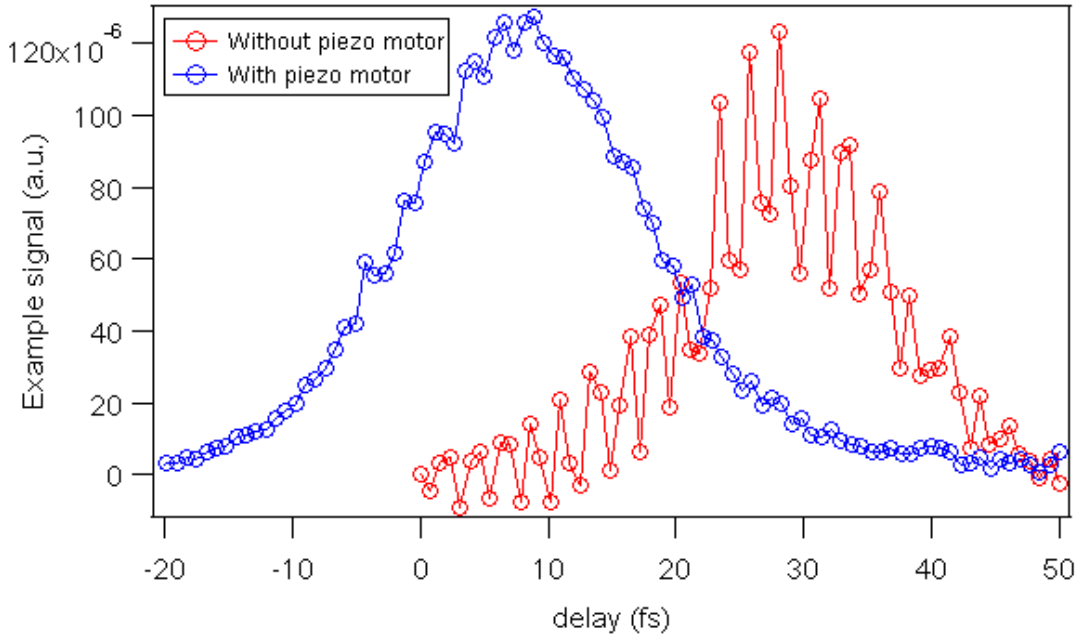

Figure 3.28: Example signal obtained before and after the use of the piezo motor to eliminate fringes. The zero of the signal is slightly shifted and the level of signal is changed, both due to new overlap conditions.

Pump and probe experiment

With short pulses having a controlled and compensated GVD and enough time resolution for measurements, it is possible to measure very short phenomena. Detecting both directions of the MO-FWM provides access to the coherence time, if there is enough time resolution, via the shift between the centers of these two signals. This shift is expected to be of the order of few fs what, with the time resolution achieved, is perfectly measurable. The schematic set-up for the focalization and detection of these signals is shown in figure 3.29.

The MO-FWM detection can be difficult considering it is a background free very low

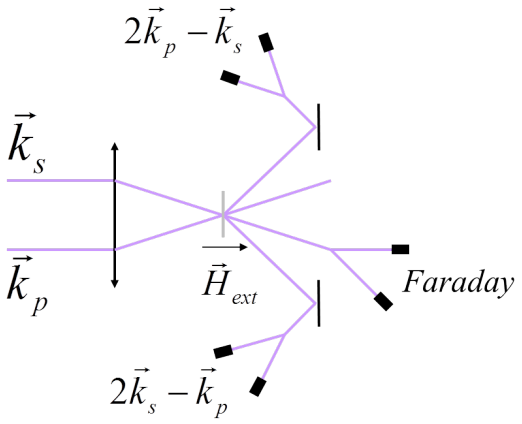

Figure 3.29: Experimental configuration for the two-beam few-cycle MO-FWM experiments.

signal. The weakest diffusion or scattering propagating in the same direction as the MO-FWM signal can make a huge offset, preventing us from seeing the right signal with the correct sensitivity. For that, many covers aim at isolating the MO-FWM signals from these spurious parasites. With a help from irises as well, it is possible to minimize the offset effect.

Zero drift correction

Due to the long time scanning, a drift of the absolute zero delay between the pulses focused on the sample is present in all signals, which means that the center of each scan is different from the previous one. This drift comes from the room humidity evolution, as shown in figures 3.30, 3.31 and 3.32, and must be corrected before the data analysis to avoid inducing errors in the estimation of the coherence time.

The different data in the graphs represent the four sets of scans of equal duration acquired in the same day, from $9am$ to $11pm$. They show $A - B$ signals, being A and B the signals measured in the two arms of the polarization bridge, and the humidity acquired at the same time. ROT stands for the rotation measurements made using a half-waveplate and ELLIP stands for the ellipticity measurements, made using the combination of a half-wave plate and a quarter-waveplate, as explained in section 3.5.2.3.

The correction is made on each series of data separately, for each direction of the external magnetic field and for the rotation and the ellipticity. On each one, the order of the series of scans is respected taking as a reference the two scans that are closest, which means, the last scan from the first series, with external field at $H_{ext} = 0°$, and the first scan of the second series, with the field at $H_{ext} = 180°$. The other scans are then shifted

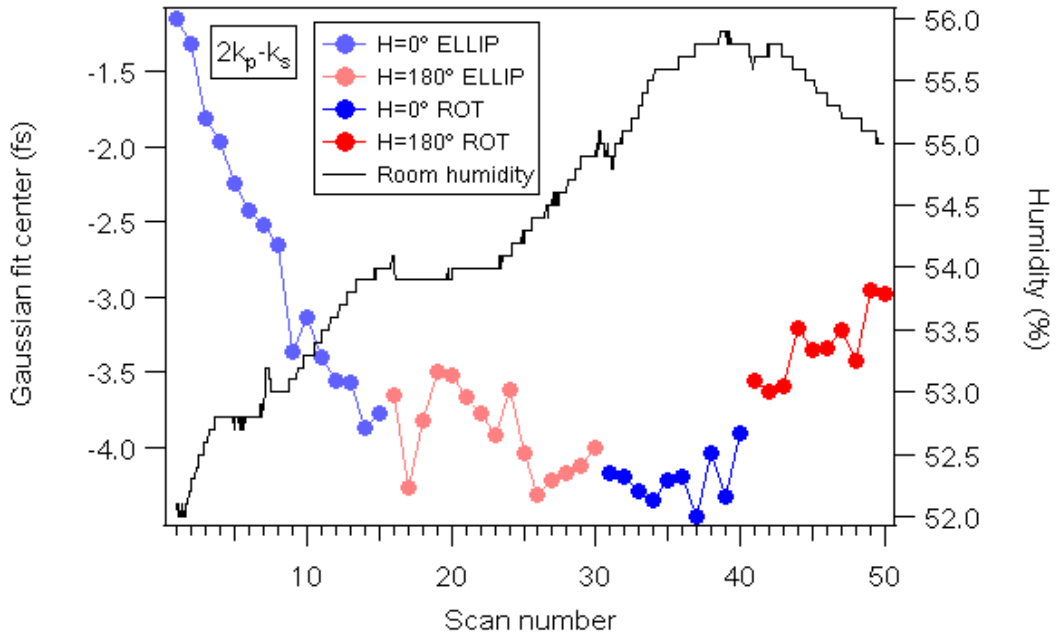

Figure 3.30: Variation of room humidity and variation of the centers of the gaussian fits made to the different scans of different sets of measurements in the direction $2\overrightarrow{k}_p - \overrightarrow{k}_s$.

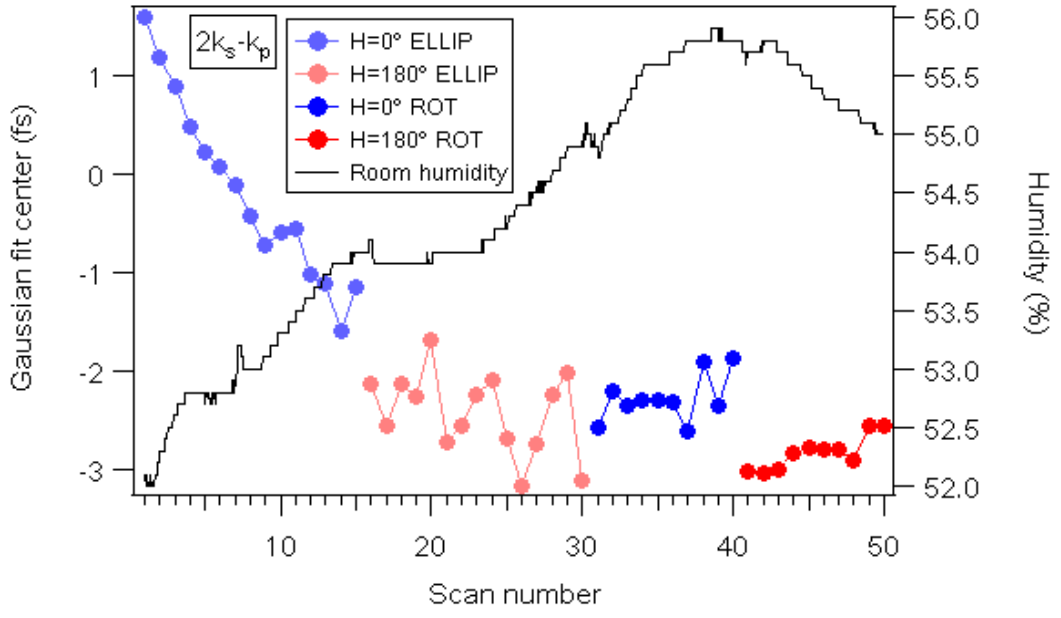

Figure 3.31: Variation of room humidity and variation of the centers of the gaussian fits made to the different scans of different sets of measurements in the direction $2\overrightarrow{k}_s - \overrightarrow{k}_p$.

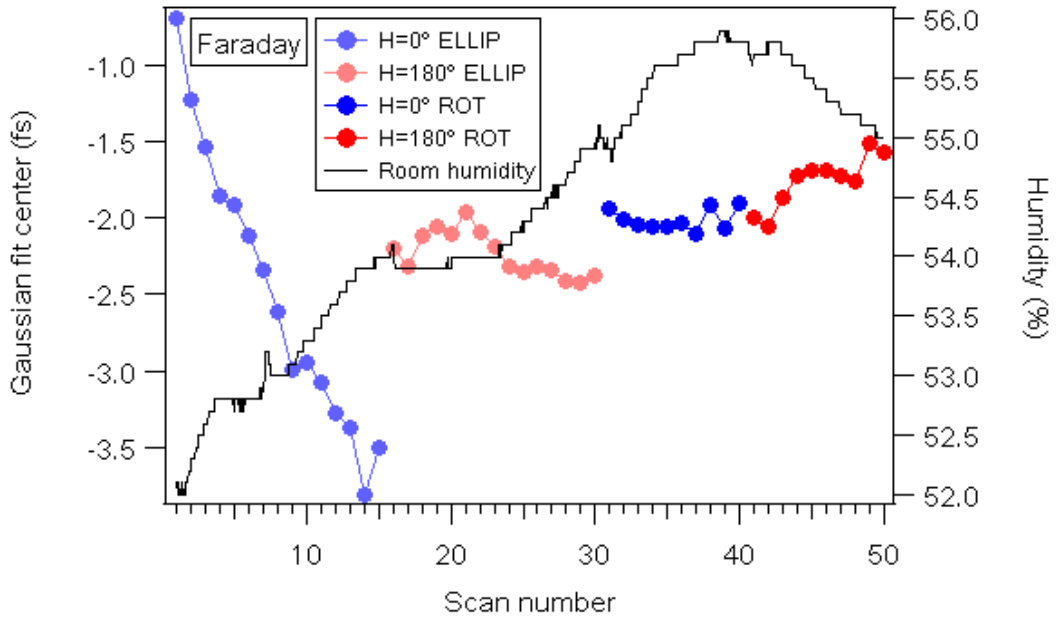

Figure 3.32: Variation of room humidity and variation of the centers of the gaussian fits made to the different scans of different sets of measurements in the direction $\overrightarrow{k}_s$.

to have the same center of the reference scans. This way, it is possible to minimize the effects of the humidity drift. Example curves before and after the zero drift correction are shown in figure 3.33.

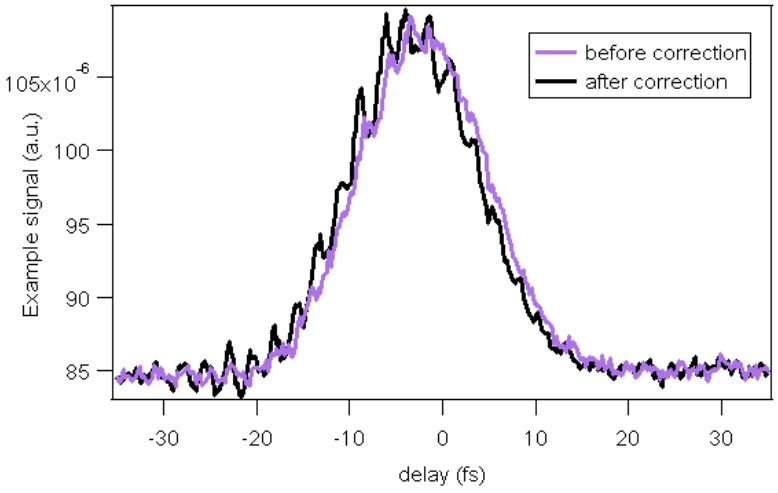

Figure 3.33: Example curves obtained before and after the zero drift correction. The gaussian fit center changed of $1fs$ with the correction and fringes present in isolated scans were acentuated.

3.5.3.3 Analysis method

The signals were analysed via a polarization bridge, as presented in appendix A and in section 3.5.2.3.

It is important to remind here that the waveplates used in this analysis were also carefully chosen for being adapted to a large spectral bandwidth.

The signals were analysed via a polarization bridge, as presented in appendix A and in section 3.5.2.3.

Chapter 4

Results and discussion

In this chapter, we present the experimental results.

First, we show the feasability and efficiency of using the magneto-optical four-wave mixing (MO-FWM) as a method to access directly the dynamics of the coherences by presenting the data obtained in a two-beam MO-FWM configuration and their analysis. We recall the set-up scheme, the system specifications and the method of analysis (crossed polarizers) and present the rough as well as the processed data. With that, we show that it is possible to measure the dynamics of the coherences separetely from the populations dynamics using a two-beam configuration by measuring the MO-FWM signal in the direction $2\overrightarrow{k}_p - \overrightarrow{k}_s$. We present also the signal detected in the $\overrightarrow{k}_s$ direction (Faraday signal) for comparison.

We show then that it is also possible to access separately the coherences and populations dynamics via a three-beam MO-FWM configuration measuring only the MO-FWM signal. We also recall the set-up scheme, the system specifications and the analysis technique (polarization bridge) and present the rough and processed data. We show that, fixing the delay τ between the first and the second pulse and varying the delay T between the first and the third pulses, we have access to the spins populations dynamics, which display a motion of precession. Fixing T and varying τ gives access to the dephasing dynamics of the magneto-optical response. These results can also be found in references [128] and [129].

Finally, we show the results obtained in the few-cycle two-beam MO-FWM configuration, with $10fs$ pulses, what allows to solve better the dynamics of the coherences. We recall the set-up scheme, the system specifications and the analysis technique (polarization bridge) and present the rough and the processed data. We show that the MO-FWM signals obtained in directions $2\overrightarrow{k}_p - \overrightarrow{k}_s$ and $2\overrightarrow{k}_s - \overrightarrow{k}_p$ are shifted in time, what allows us giving a superior limit for the coherence time.

4.1 Experimental distinction between the coherences and populations dynamics

4.1.1 Magneto-optical four-wave mixing in the two-beam configuration

4.1.1.1 System and set-up description

This section presents the results obtained with the experiments performed on the apparatus described on section 3.5.1. As a reminder, we recall here figure 3.19 that shows the experimental configuration.

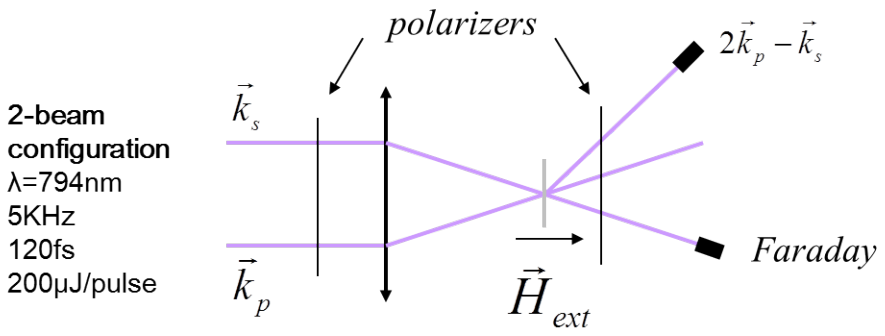

Figure 4.1: Two-beam MO-FWM configuration and system specifications.

In this set-up, we have measured the time-resolved Faraday signal in the direction $\overrightarrow{k_s}$ of the probe beam and the time-resolved MO-FWM signal in the direction $2\overrightarrow{k}_p - \overrightarrow{k}_s$. These signals were generated in a bismuth-doped $7\mu m$ garnet sample already described in section 3.1.4.

The pump and probe pulses have duration of $120fs$ and a central wavelength of $794nm$, they are focused with a spot diameter of $100\mu m$ onto the sample where they overlap spatially. Pump has an energy density of $I_p = 1,45mJ/cm^2$ and probe has an energy density of $I_s = 1,27mJ/cm^2$. We remind here that the pump and probe beams do not present the usual $10:1$ ratio used in Faraday experiments to optimize the MO-FWM signal and that the coherence time T_2 is not expected to depend on the pumping energy. However, the spins lifetime T_1 does depend on the density of excitation.

The Faraday and MO-FWM signals were analysed with the crossed polarizers technique, described on section 3.5.1.3. The outputs of the photodiodes are connected to a lock-in amplifier. A chopper is placed on the pump for the reference input.

4.1.1.2 Measured signals

The non processed signals obtained for the analyser polarizer angle $\alpha = 155°$ in the directions $\overrightarrow{k_s}$ and $2\overrightarrow{k}_p - \overrightarrow{k}_s$ are shown in figures 4.2 and 4.3. This angle was chosen for the high contrast found between the two directions of the field (perpendicular to the sample). We have obtained similar curves for all the other angles of the analyser polarizer.

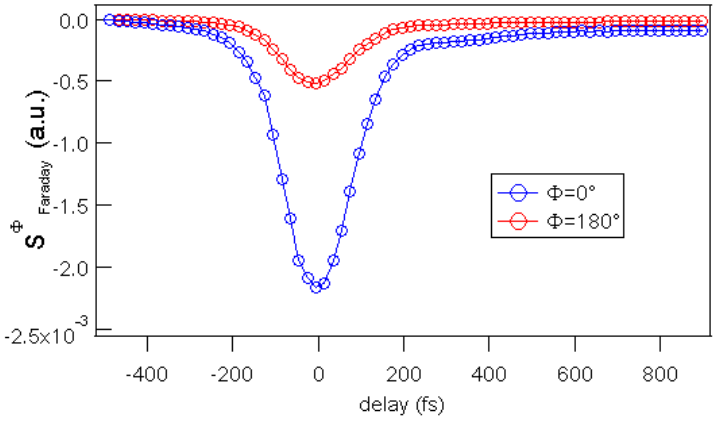

Figure 4.2: Faraday signal obtained for the two complementary directions Φ of the external magnetic field (with respect to the normal of the sample) in the two-beam configuration. The analyser polarizer angle is $\alpha = 155°$.

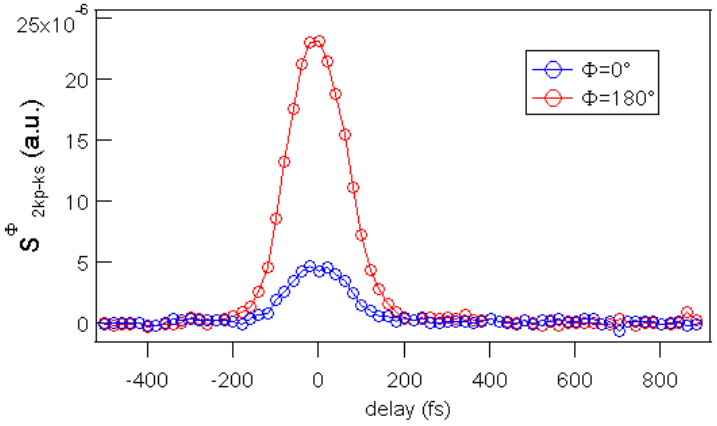

Figure 4.3: MO-FWM signal obtained for the two complementary directions Φ of the external magnetic field (with respect to the normal of the sample) in the two-beam configuration. The analyser polarizer angle is $\alpha = 155°$.

4.1.1.3 Populations and coherences dynamics

The differential signals were obtained by substracting the signals for the complementary directions of the external magnetic field applied perpendicular to the sample (of magnitude $H_{ext} = 5kG = 500mT$), as follows.

$$\Delta S_{Faraday}(\tau) = S^{180^\circ}_{Faraday}(\tau) - S^{0^\circ}_{Faraday}(\tau) \tag{4.1}$$

$$\Delta S_{2\vec{k}_p - \vec{k}_s}(\tau) = S^{180^\circ}_{2\vec{k}_p - \vec{k}_s}(\tau) - S^{0^\circ}_{2\vec{k}_p - \vec{k}_s}(\tau) \tag{4.2}$$

Here, the signals S corresponds to the difference between the arms of the polarization bridge A and B, being $S = A - B$. This procedure allows eliminating the contribution of charges, which does not depend on the magnetic field.

Figure 4.4 shows the normalized differential signals obtained in the $\vec{k}_s$ direction (Faraday signal) and in the $2\vec{k}_p - \vec{k}_s$ direction (MO-FWM signal). A reference optical four-wave mixing signal generated in a nonmagnetic TiO_2 thin film is shown for comparison.

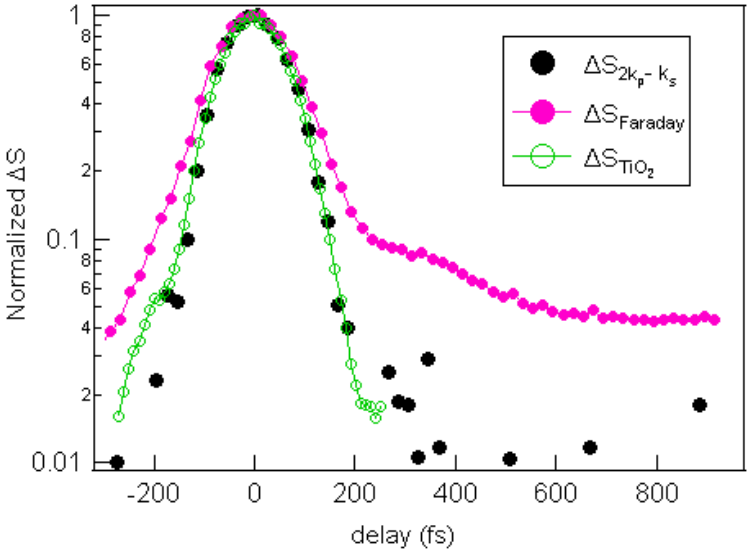

Figure 4.4: MO-FWM and Faraday normalized differential signals generated in a bismuth-doped garnet sample and optical four-wave mixing signal generated in a TiO_2 thin film in the two-beam configuration compared in logarithmic scale.

4.1.1.4 Discussion

In figure 4.4, one observes a large contribution at positive time delays in the Faraday signal that corresponds to the spin population relaxation due to the spin-lattice interaction and

the recovery of the magnetization modulus initially reduced by the laser pulse. It is clear that the MO-FWM signal does not contain this contribution. This is observed by the large difference between the Faraday and MO-FWM curves.

This proves the success of the experiment in measuring the coherent contribution of the magneto-optical response of a garnet film isolated from the populations contribution. However, the pulse duration is not short enough to solve the coherence time.

4.1.2 Magneto-optical four-wave mixing in the three-beam configuration

4.1.2.1 System and set-up description

The experiments were performed using the apparatus described in section 3.5.2. As a reminder, we recall here figure 3.20 that shows the experimental configuration.

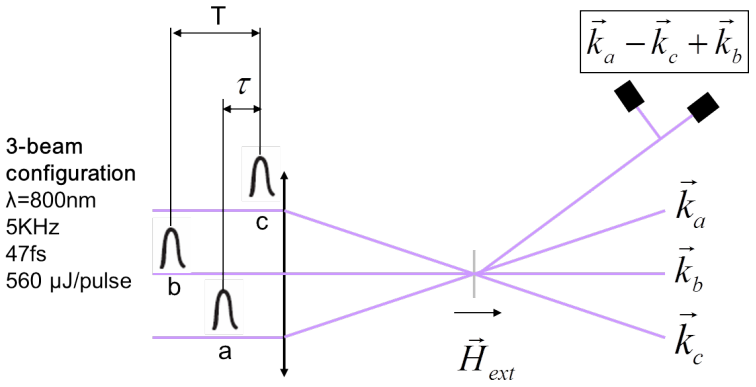

Figure 4.5: Three-beam MO-FWM configuration and system specifications.

In this set-up, we have measured the time-resolved MO-FWM signal in the direction $\vec{k}_a - \vec{k}_c + \vec{k}_b$. These signals were also generated in a bismuth-doped $7\mu m$ garnet sample already described in section 3.1.4.

Pump and probe pulses have duration of $47fs$ and a central wavelength of $800nm$. The spot diameter is $\sim 100\mu m$ and the beams fluences are: $I_{k_a} = 0,53mJ/cm^2$, $I_{k_b} = 0,68mJ/cm^2$ and $I_{k_c} = 0,56mJ/cm^2$.

The Faraday and MO-FWM signals were analysed with the polarization bridge technique, described in section 3.5.2.3. The outputs of the photodiodes are connected to a lock-in amplifier. A chopper is placed on the pump for the reference input.

4.1.2.2 Measured signals

The nontreated MO-FWM signals obtained in the direction $\overrightarrow{k}_a - \overrightarrow{k}_c + \overrightarrow{k}_b$ for the two opposite directions of the external magnetic field are shown in figure 4.6.

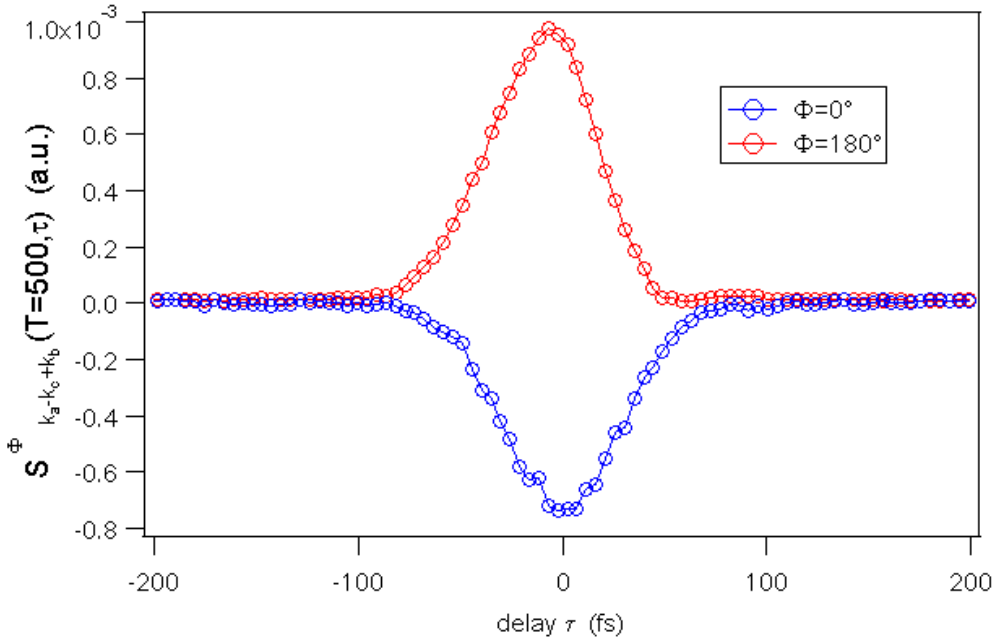

Figure 4.6: MO-FWM signals obtained in the direction $\overrightarrow{k}_a - \overrightarrow{k}_c + \overrightarrow{k}_b$ for the two complementary directions Φ of the external magnetic field (with respect to the normal of the sample) for $T = 500fs$ in the three-beam configuration.

It is important to highlight that there is a $9,8fs$ difference between the center of the signals obtained for the two opposite directions of the external field. This is due to a small displacement of the sample, caused by the magnet interaction with the 3-axis support of the sample. The correction of this shift implies a change in the center of the magneto-optical differential signal, but does not alter ist duration, point of interest of this part of the analysis. We have then corrected the shift shown in figure 4.6 before subtracting the signals.

4.1.2.3 Populations and coherences dynamics

The differential MO-FWM signal was obtained by substracting the signals generated for both directions of the external magnetic field applied perpendicular to the sample (of magnitude $H_{ext} = 3,5kG = 350mT$), as follows.

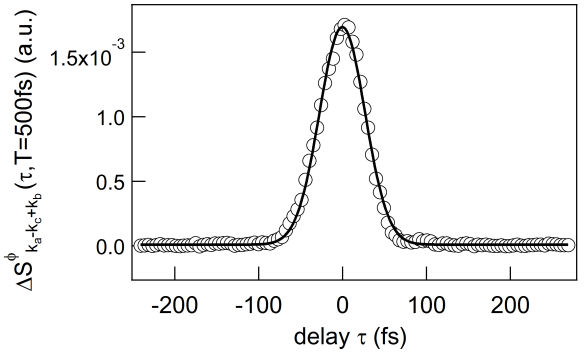

Figure 4.7: Normalized differential MO-FWM signal obtained for the three-beam configuration and its gaussian fit (duration: $(38,66 \pm 0,02)fs$). Coherent response as a function of τ for a fixed delay $T = 500fs$.

$$\Delta S_{\overrightarrow{k}_a - \overrightarrow{k}_c + \overrightarrow{k}_b}(\tau) = S^{H+}_{\overrightarrow{k}_a - \overrightarrow{k}_c + \overrightarrow{k}_b}(\tau) - S^{H-}_{\overrightarrow{k}_a - \overrightarrow{k}_c + \overrightarrow{k}_b}(\tau) \tag{4.3}$$

Here, the signals S corresponds to the difference between the arms of the polarization bridge A and B, being $S = A - B$. This procedure allows eliminating the contribution of charges, which does not depend on the magnetic field.

The differential signals obtained from the two measurements in the direction $\overrightarrow{k}_a - \overrightarrow{k}_c + \overrightarrow{k}_b$ ($H+$ and $H-$) fixing T and varying τ are shown in figure 4.7. Figure 4.8 shows the Faraday signal fixing τ and varying T.

4.1.2.4 Discussion

When the delay T is fixed, it is possible to obtain the differential signal from the two directions of the external field perpendicular to the sample. With that, one is able to access the dynamics of the coherent response by varying the delay τ, as shown on figure 4.7. Clearly, this response is still dominated by the pulse duration.

However, fixing the delay τ and applying an external field with an angle of 30° or even 60° with respect to the normal of the sample allows accessing the precession of the magnetization and seeing its difference as a function of the effective field. Therefore, we have access to the full spin population that contains the thermalization of spins, the electron/spin-lattice relaxation ($\sim 1,35ps$), the precession of the magnetization and the heat diffusion ($> 1ns$). The long delay behavior of the Faraday signal presented in figure 4.8 shows the oscillations corresponding to the projections of the motion of precession onto

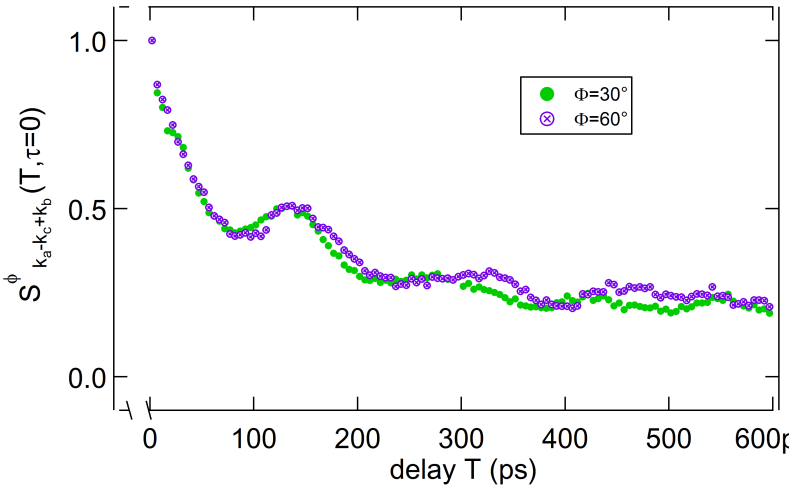

Figure 4.8: MO-FWM signals obtained for the three-beam configuration. Precession dynamics of the macrospins as a function of T for a fixed delay $\tau = 0$ and an external field angle of 30° and 60° (with respect to the normal of the sample) showing the precession with periods 146ps and 162ps, respectively. The precession damping happens in a characteristic time around 150ps.

the polar direction, perpendicular to the sample plane. The precession periods obtained were 146ps for the external field at 30° and 162ps for 60°. The damping of the precession was found around 150ps.

The coherent spin-photon interaction that leads to the emission of the MO-FWM signal is different from the coherent motion of precession of the magnetization reported earlier in transition metals [45] [47]. The analysis of the polar component of the magnetization allows understanding that the laser induced precession results from the time dependent anisotropy of the garnet film [74]. This behavior is similar to the one reported earlier in the case of a ferrimagnetic garnet [130].

It has been demonstrated that it is possible to start a precession movement of the magnetization using circularly polarized pulses and that the phase of the precession depends on the polarization (circularly right or left) [50] [52]. This phase dependance is attibuted to a coherent interaction between the photons and the spins. However, for that, the precession must start during the interaction with the laser field, as showed by our group [74]. The laser pulse modifies the modulus of the magnetization what changes the shape anisotropy and starts the precession movement.

The observation of the precession and of the different diffusion and relaxation times allow the validation of the MO-FWM three-beam configuration as a tool to well describe the magnetization dynamics.

4.2 Coherent dynamics with few-cycle pulses

As shown before in section 1.3.2, the four-wave mixing signal can be interpreted by a convolution between the gaussian pulse and the exponential decay depending on the inhomogeneous or homogeneous broadening. If the pulse duration is much more important than the dephasing time, one does not solve T_2. This is why it is important to perform experiments with few-cycle pulses.

4.2.1 Magneto-optical four-wave mixing in the two-beam configuration with nonamplified pulses

4.2.1.1 System and set-up description

This section presents the results obtained with the experiments performed on the apparatus described in section 3.5.3. As a reminder, we recall here picture 3.29 that shows the experimental configuration.

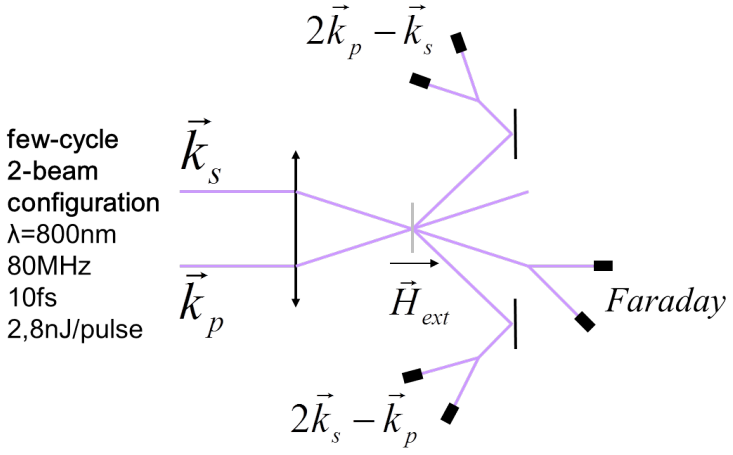

Figure 4.9: Few-cycle two-beam MO-FWM configuration and system specifications.

With this set-up, we have measured the time-resolved Faraday signal in the direction $\overrightarrow{k}_s$ of the probe beam and the time-resolved MO-FWM in the directions $2\overrightarrow{k}_p - \overrightarrow{k}_s$ and $2\overrightarrow{k}_s - \overrightarrow{k}_p$. These signals were generated in the same garnet sample described earlier in section 3.1.4.

The pump and probe pulses have a duration of $10fs$ and a central wavelength of $820nm$, they are focused with a spot diameter of $170\mu m$ onto the sample where they overlap spatially. The pump has an energy density of $I_p = (1,34 \pm 0,05)\mu J/cm^2$ and the probe has an energy density of $I_s = (1,63 \pm 0,05)\mu J/cm^2$. Once again, the probe fluence

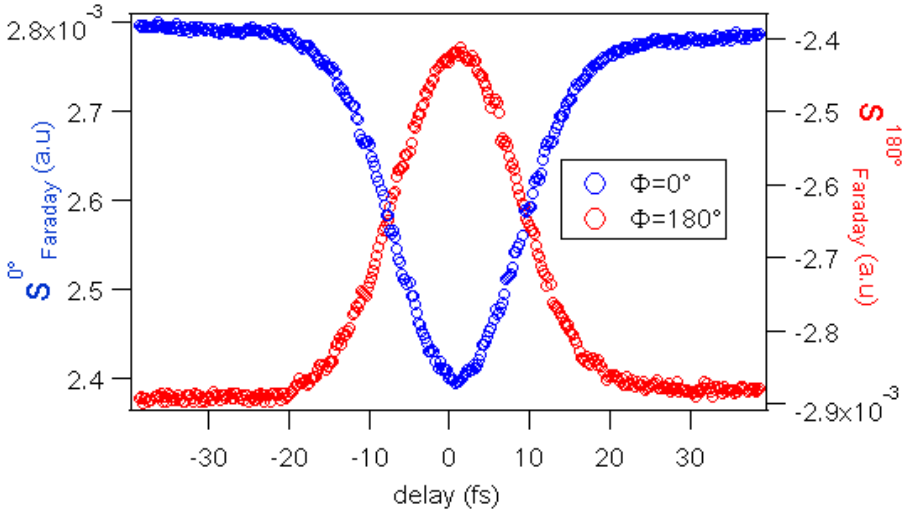

Figure 4.10: Faraday signal obtained for the two complementary directions Φ of the external magnetic field (with respect to the normal of the sample) in the few-cycle two-beam configuration.

is more important than usual in order to improve the MO-FWM signal.

The Faraday and two MO-FWM signals were analysed with the polarization bridge technique, described on section 3.5.2.3. A lock-in amplifier is used with a chopper placed on the pump beam.

4.2.1.2 Measured signals

The signals obtained in the directions $\overrightarrow{k_s}$, $2\overrightarrow{k}_p - \overrightarrow{k}_s$ and $2\overrightarrow{k}_s - \overrightarrow{k}_p$ for both directions of the external field are shown in figures 4.10, 4.11 and 4.12. For the six curves presented here, the zero drift correction, previously presented in section 3.5.3.2, has been applied.

Figures 4.11 and 4.12 show the measured signals in the MO-FWM directions. The center of these signals are shifted in comparison to the centers of the Faraday signals shown in figure 4.10. This is exactly the interesting characteristic to be explored to obtain an estimation of the coherence time. However, the signals obtained for $\Phi = 0°$ and $\Phi = 180°$ do not present the exact same center. There is a shift of $(0,18 \pm 0,02)fs$ between the signals measured in direction $2\overrightarrow{k}_p - \overrightarrow{k}_s$ and a shift of $(1,31 \pm 0,02)fs$ between the signals measured in the direction $2\overrightarrow{k}_s - \overrightarrow{k}_p$. The difference is certainly due to the influence of the magnet, as already discussed in section 4.1.2 and was already mentioned in section 3.5.3.2. This effect was minimized with the position of the sample and of the magnet. It enlarges the error bar to be considered in the definition of the center of the differential signals.

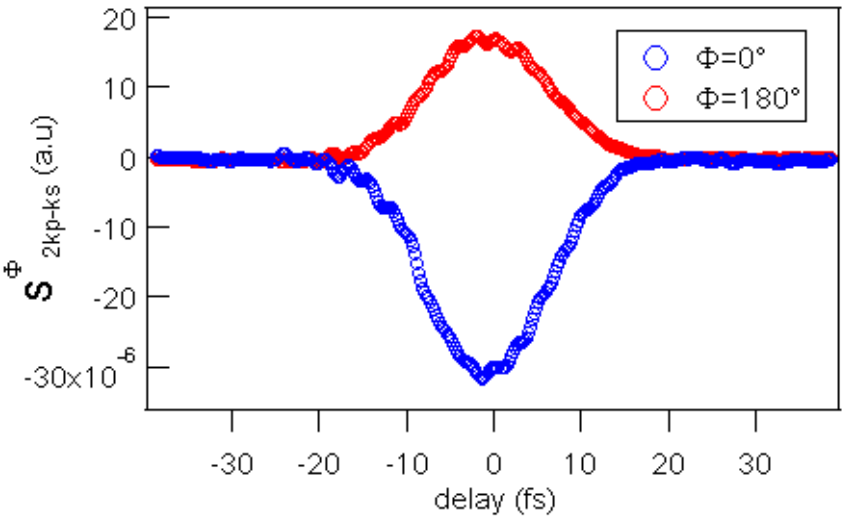

Figure 4.11: MO-FWM signal generated in the direction $2\overrightarrow{k}_p - \overrightarrow{k}_s$ obtained for the two complementary directions Φ of the external magnetic field (with respect to the normal of the sample) in the few-cycle two-beam configuration.

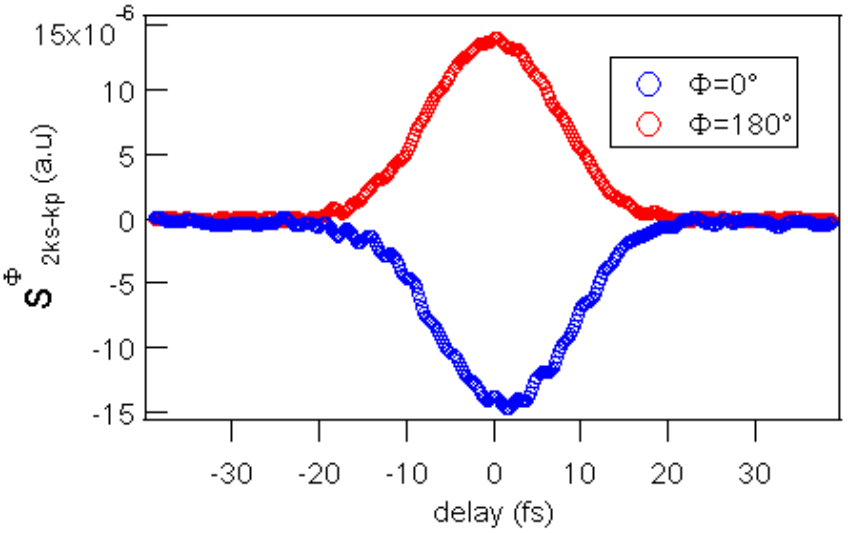

Figure 4.12: MO-FWM signal generated in the direction $2\overrightarrow{k}_s - \overrightarrow{k}_p$ obtained for the two complementary directions Φ of the external magnetic field (with respect to the normal of the sample) in the few-cycle two-beam configuration.

4.2.1.3 Populations and coherences dynamics

The differential signals were obtained by substracting the signals obtained for both directions of the external field applied perpendicular to the sample (of magnitude $H_{ext} = 3,5kG = 350mT$) as follows.

$$\Delta S_{Faraday}(\tau) = S^{H+}_{Faraday}(\tau) - S^{H-}_{Faraday}(\tau) \tag{4.4}$$

$$\Delta S_{2\vec{k}_p - \vec{k}_s}(\tau) = S^{H+}_{2\vec{k}_p - \vec{k}_s}(\tau) - S^{H-}_{2\vec{k}_p - \vec{k}_s}(\tau) \tag{4.5}$$

$$\Delta S_{2\vec{k}_s - \vec{k}_p}(\tau) = S^{H+}_{2\vec{k}_s - \vec{k}_p}(\tau) - S^{H-}_{2\vec{k}_s - \vec{k}_p}(\tau) \tag{4.6}$$

Here, the signals S corresponds to the difference between the arms of the polarization bridge A and B, being $S = A - B$. This procedure allows eliminating the contribution of charges, which does not depend on the magnetic field.

Figure 4.13 shows the normalized differential signals obtained in the $\vec{k}_s$ direction (Faraday signal) and in the $2\vec{k}_p - \vec{k}_s$ and $2\vec{k}_s - \vec{k}_p$ directions (MO-FWM signals).

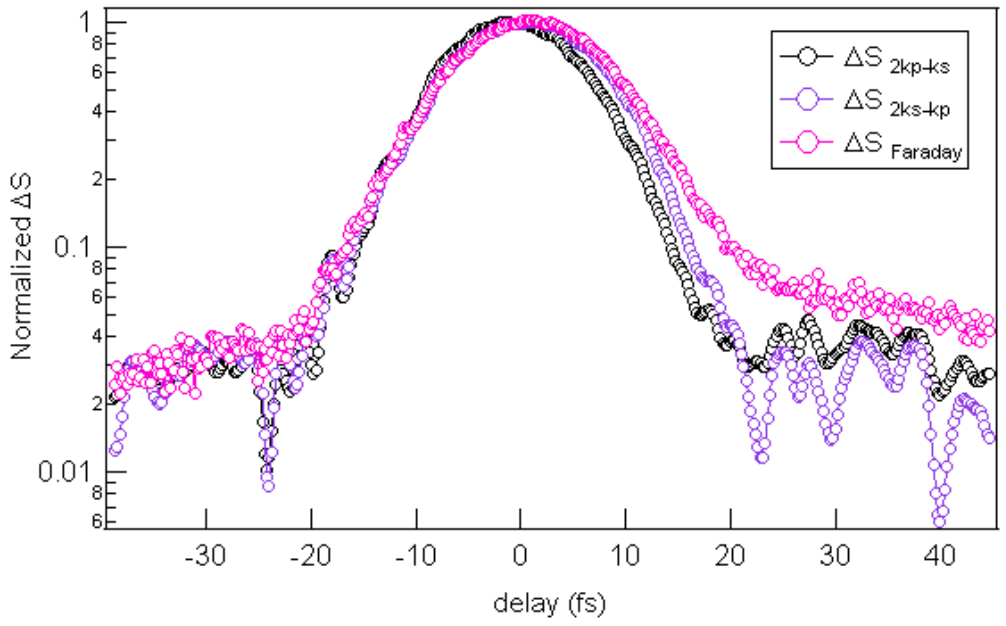

Figure 4.13: MO-FWM and Faraday normalized differential signals generated in a bismuth-doped garnet sample in the few-cycle two-beam configuration compared in logarithmic scale. Notice the noise level $\lesssim 3 \times 10^{-2}$.

Figures 4.14 shows the signals generated in the two directions of the MO-FWM, $2\vec{k}_p - \vec{k}_s$ and $2\vec{k}_s - \vec{k}_p$. They are presented non-normalized and with different scales

to highlight the temporal shift between their centers. These data were produced with the data shown previously in section 4.2.1.2, so they present the zero drift correction as well.

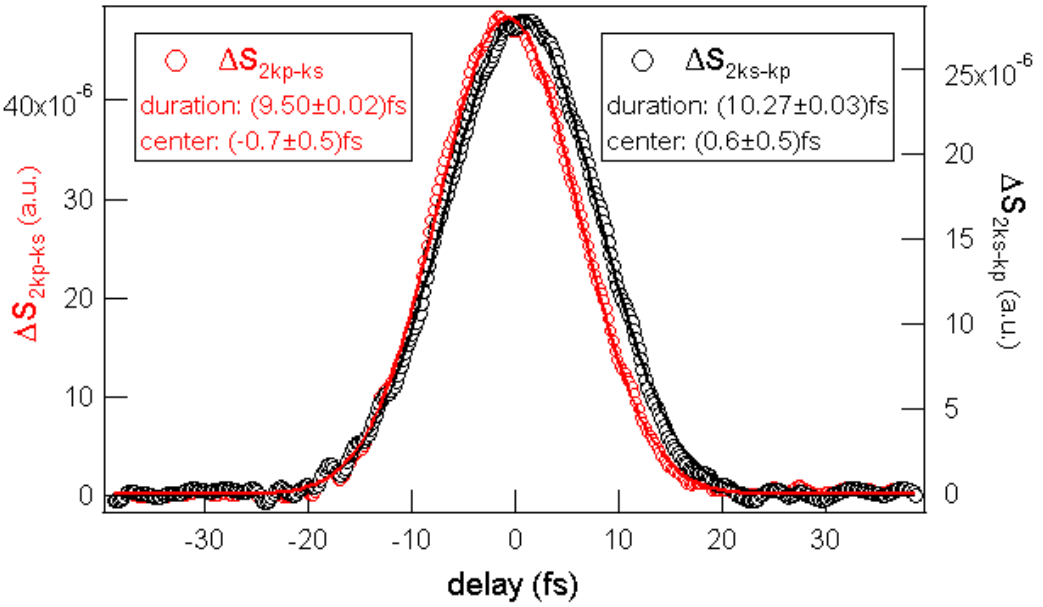

Figure 4.14: Differential MO-FWM signals generated in a bismuth-doped garnet sample in the few-cycle two-beam configuration and their gaussian fits. The signals were measured simulteneously in the directions $2\vec{k}_p - \vec{k}_s$ and $2\vec{k}_s - \vec{p}_s$. The time shift between the centers is $(1,3 \pm 0,5) fs$.

4.2.1.4 Electronic coherence time

As shown in section 3.5.2.3, the magneto-otpical signals are obtained by substracting the signals of the polarization bridge ($A-B$, difference between the two arms) for the opposite directions of the external field. It is possible then to consider the signal in only one of the arms of the polarization bridge (A) to obtain the optical signal without magnetic contribution, as follows.

$$\sum S_{2\vec{k}_s - \vec{k}_p}(\tau) = A^{H+}_{2\vec{k}_s - \vec{k}_p}(\tau) + A^{H-}_{2\vec{k}_s - \vec{k}_p}(\tau) \tag{4.7}$$

$$\sum S_{2\vec{k}_p - \vec{k}_s}(\tau) = A^{H+}_{2\vec{k}_p - \vec{k}_s}(\tau) + A^{H-}_{2\vec{k}_p - \vec{k}_s}(\tau) \tag{4.8}$$

Figure 4.15 shows the signals obtained for the two optical signals generated in the directions $2\vec{k}_p - \vec{k}_s$ and $2\vec{k}_s - \vec{k}_p$.

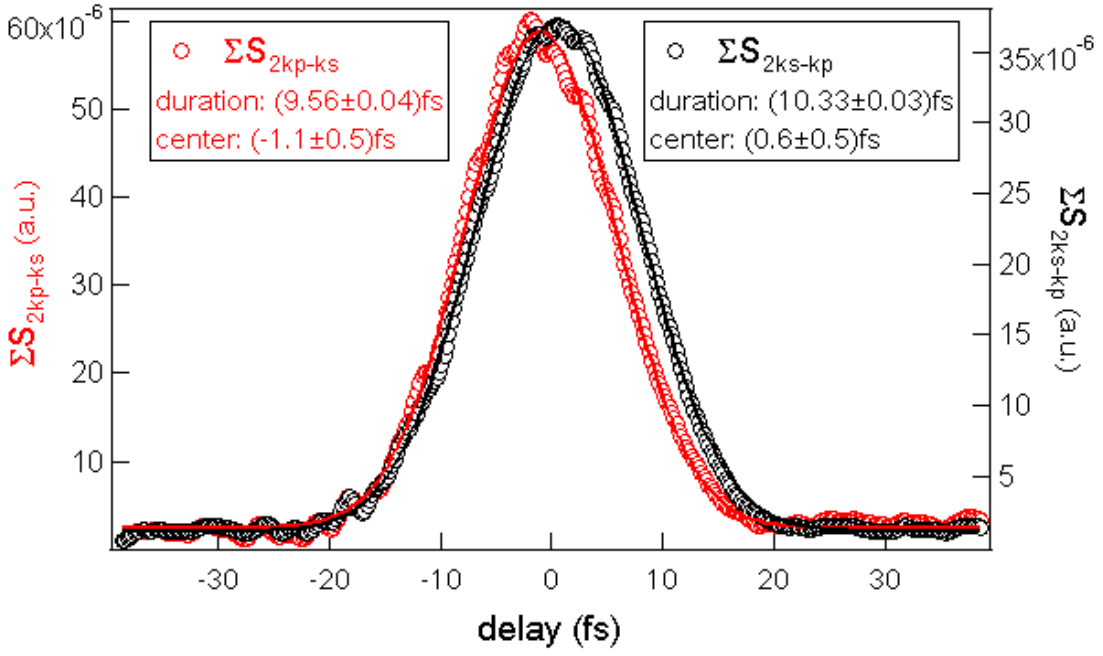

Figure 4.15: Differential optical four-wave mixing signals generated in a bismuth-doped garnet sample in the few-cycle two-beam configuration and their gaussian fits. The signals were measured simultaneously in the directions $2\overrightarrow{k}_p - \overrightarrow{k}_s$ and $2\overrightarrow{k}_s - \overrightarrow{p}_s$. The time shift between the centers is $(1,7 \pm 0,5) fs$.

4.2.1.5 Discussion

As already shown in section 4.1, we confirm from figure 4.13 that the Faraday signal contains the population component not present in any of the MO-FWM signals. Differently from the results presented in sections 4.1.1 and 4.1.2, the time resolution is shorter and the curves are better sampled and display much shorter signals.

As shown previously in section 1.2.4, the main advantage of this configuration is that it allows measuring the time shift between the centers of the two signals, what gives an indication about the dephasing time T_2. The usual method is to obtain T_2 via the exponential decays in negative time for $2\overrightarrow{k}_p - \overrightarrow{k}_s$ and in positive times for $2\overrightarrow{k}_s - \overrightarrow{k}_p$. This comes from the fact that these signals can be understood as a convolution of a gaussian pulse with an exponential decay, as presented in section 1.3.2. The exponential decay should then manifest in this convolution as an asymmetry in the signals, on the left for $2\overrightarrow{k}_p - \overrightarrow{k}_s$ and on the right for $2\overrightarrow{k}_s - \overrightarrow{k}_p$, what is not visible in figure 4.14. This happens because the pulse is still longer than T_2 and the convolution is dominated by the

gaussian shape of the pulse. This shows that the dephasing time is still shorter than the pulse duration of $\sim 10fs$.

In figure 4.16, we show the simulations presented in section 1.3.2 for an estimated T_2 of $4fs$ and $d = 10fs$ (as used for these measurements).

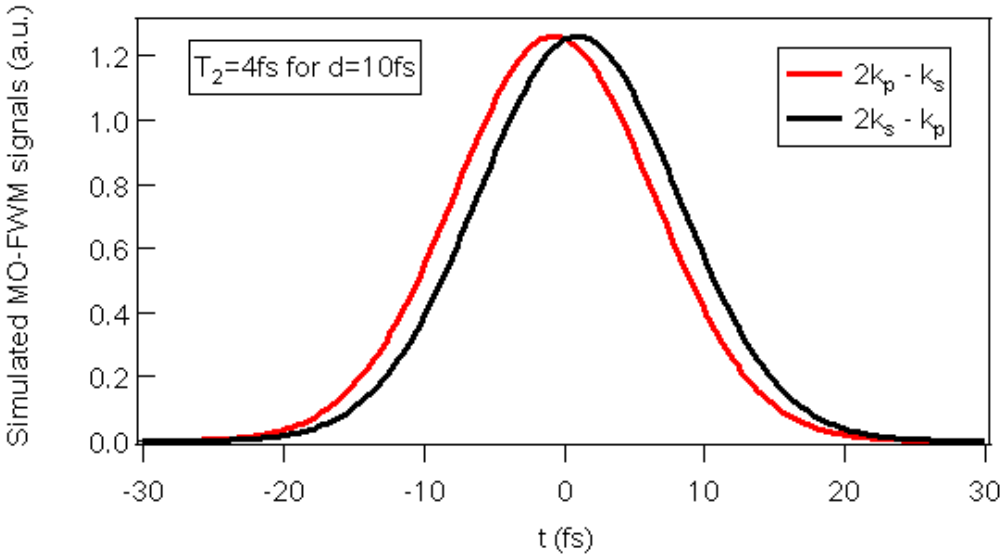

Figure 4.16: Simulation of the results of equation 1.76 for $d = 10fs$ and $T_2 = 4fs$.

Even if the lack of asymmetry does not allow obtaining T_2 from the exponential decay, as it is hidden by the gaussian shape, the difference between the centers of the signals can still give access to the coherence time. It is possible to fit the curves using equation 1.76 and to obtain the values of T_2 and d that suit better, keeping in mind that, for an important value of d, one may find an interval for T_2, as the duration is more important in the response for longer pulse durations. For the curves shown in figure 4.14, the signals ΔS_{2kp-ks} and ΔS_{2ks-kp} are better fitted for pulse durations of $d_{2kp-ks} = 9,5fs$ and $d_{2ks-kp} = 10,5fs$. The different durations for pump and probe are probably due to the different quantity of glass crossed by each beam. This quantity was minimized in both beams but is not equal, what still allowed obtaining close durations for both pulses. These simulations and fits give $2,5fs \leq T_{2\ 2kp-ks} \leq 3,5fs$ and $2fs \leq T_{2\ 2ks-kp} \leq 3fs$.

We show here that the temporal shift between the signals is present and visible and highlight that even with pulses longer than T_2 that do not allow to find it via the exponential decay, the MO-FWM configuration is still sensitive to this difference. This shows that the method is suitable for accessing ultrashort coherent phenomena.

The duration of the pulse delivered from the laser systems used in the two and three-beam configurations was much longer than T_2. It is then, needless to say that, as for the

case of $d = 10fs$, the response of the sample for a pulse of $d = 47fs$ or even $d = 120fs$ does not allow observing an asymmetry.

The optical response, shown in figure 4.15, gives access to the electronic dephasing time T_{2e} and the magneto-optical response, shown in figure 4.14, gives access to the electromagnetic dephasing time T_{2em}. Therefore, T_{2e} and T_{2em} have really close values, as the optical center difference is $(1,7 \pm 0,5)fs$ and the magneto-optical center difference is $(1,3 \pm 0,5)fs$. This shows that we are not sensitive to a possible diference between these two times. We can affirm, however, that the spins dephasing time is as short as the charges dephasing.

The present study shows that, in spite of our approach of trying to obtain the dephasing times out of resonance, using ultimate temporal resolution, there is no significant difference in the coherence of optical and magneto-optical signals. We conclude that the spin-orbit interaction is quasi instantaneous in this material.

Let us emphasize that the approach of using shorter laser pulses obtained from an oscillator has considerably improved the temporal resolution at the expense of a much larger spectrum. Unfortunately, in the case of Ti:sapphire, this spectrum extends to the infra-red range, that is in the transparent region of our garnet sample. As a consequence, the measured T_2 times (both electronic and magnetic) concern "virtual" states of the garnet level structure. Such virtual states are most likely related to an important magnetic inhomogeneity, as expected in such soft materials with domains of the order of a few microns, the laser spot being rather in the range of $100\mu m$.

General conclusions and perspectives

In this thesis, we have studied the coherent magneto-optical response of a ferrimagnetic garnet using different experimental approaches.

In a first moment, we have shown that the two-beam MO-FWM configuration is a suitable technique to provide direct access to the coherent component of the magneto-optical response of the sample. We have compared this signal to the Faraday one obtained simultaneously to highlight that the populations component present in the Faraday signal, responsible for hiding the coherent response, was not present in the MO-FWM signal. After the work published by our group in 2009, that proves the existence of the coherent component in the magneto-optical response and shows its polarization dependance, these results were of main importance to show an effective method to measure this component directly from a MO-FWM experiment. However, the pulse duration was not short enough to allow an estimation of the coherence time T_2.

We have also shown the possibility of studying the populations and coherences dynamics using a three-beam MO-FWM configuration. The main advantage of this configuration is the possibility of accessing the two components of the magneto-optical signal with the same MO-FWM signal, just by varying or fixing different delays, while in the two-beam MO-FWM configuration, the populations dynamics is obtained through the Faraday signal and the coherences dynamics is obtained through the MO-FWM signal. The configuration with T fixed, that gives access to the population dynamics via the MO-FWM signal, allowed to obtain a spin-lattice relaxation time of $1,35ps$ and a damping of the precession of $150ps$. The precession period decreases with the angle of the externals field: $162ps$ for $60°$ and $146ps$ for $30°$.

Although these two experiments revealed the efficacity of two different methods to study the coherent behavior of the magnetization separately from the populations behavior, the pulse durations used ($120fs$ for the two-beam configuration and $47fs$ for the three-beam configuration) were not short enough to measure the coherence time, expected to be

shorter than $10fs$. The coherence response, even if measured isolated, was still dominated by the pulse duration and an optimization of the pulse duration was necessary.

For that, we have performed the MO-FWM experiments with $10fs$ pulses. We have exposed in the thesis the difficulty of handling ultrashort pulses. The effects of dispersion are of great importance and demand a re-examination of all the aspects of a pump and probe experiment. Using this set-up, we have shown that with enough time resolution one can access the temporal shift present between the two directions of the MO-FWM, $2\overrightarrow{k}_p - \overrightarrow{k}_s$ and $2\overrightarrow{k}_s - \overrightarrow{k}_p$, that allows estimating the coherence time T_2.

The response of the sample can be interpreted by a convolution of a gaussian pulse and the exponential decay that represents the relaxation of the coherences (inversely proportional to T_2). We were then able to estimate the coherence time via the fits of this convolution function. This allowed to obtain $2fs \leq T_2 \leq 3,5fs$, while the distance between the center of the signals emitted in the directions $2\overrightarrow{k}_p - \overrightarrow{k}_s$ and $2\overrightarrow{k}_s - \overrightarrow{k}_p$ was $(1,3 \pm 0,5)fs$. This shows the time resolution was still not fully adapted for the temporal scales considered, but allows especulating a factor 2 between the time shift and the value of T_2. We have also simulated FWM signals based on a two-level system considering different spectral phases, what allowed us to conclude that well knowing the phase of the ultrashort pulse used to estimate T_2 is of extreme importance for obtaining the relation between the shift between the two directions of the MO-FWM and the coherence time. Simulations of IAC confirmed the low significance of the phase of the pulse used in the acquisitions in this last step.

We have found in the optical FWM configuration a shift of $(1,7 \pm 0,5)fs$ between the two directions of emission that allows to affirm that, with the experimental conditions used, there is no significant difference between the optical and magneto-optical signals.

We have also presented here a model based on an hydrogen-like atom in an eight-level system that allows to better understand the magneto-optical response measured in all the experiments mentioned above. We have shown how its interaction hamiltonian allows to obtain the evolution of the density matrix elements and we have presented simulations of the different time ordered components present in the dynamics of the spin and orbital moments.

These results open important possibilities for the future research.

As we have now excellent techniques to measure directly the coherent component of the magneto-optical response, performing the same experiments with an even shorter pulse duration would allow a complete study of the coherence time. As it allows to obtain T_2 via the exponential decay and via the temporal shift between the two directions of the MO-FWM, a comparison study can lead to a theoretical model of the response.

The three set of results presented here were obtained using pulses with spectrum centered around $800nm$. Having the garnets magneto-optical response resonant in shorter wavelenghts, the straightforward conclusion is that a study as a function of the wavelenght would be rich. It would help understanding the response of the sample for different probing energies.

Experiments in the Kerr configuration would also provide valuable information to retrieve the full magneto-optical tensor.

Studying other type of garnets as a function of the type of rare-earth and its doping percentage in the same conditions is also of great interest, as one can tune the resonance with the carrier frequency of the laser. Alternatively, one can tune the laser to study the resonant cases.

Appendix A

Polarization bridge in the static case

In the most general case, the two components of polarization of an elliptically polarized electric field can be defined in terms of the rotation and ellipticity as shown in figure A.1.

With that, one has

$$\begin{pmatrix} E_x \\ E_y \end{pmatrix} = \begin{pmatrix} cos\beta e^{-i\frac{\Delta}{2}} \\ sin\beta e^{i\frac{\Delta}{2}} \end{pmatrix}, \tag{A.1}$$

where

$$\Delta = arctan\frac{2\varepsilon}{(1-\varepsilon^2)sin(2\alpha)} \text{ and } \gamma = arctan\sqrt{\frac{1-\frac{1-\varepsilon^2}{1+\varepsilon^2}cos(2\alpha)}{1+\frac{1-\varepsilon^2}{1+\varepsilon^2}cos(2\alpha)}}. \tag{A.2}$$

In the Jones matrix formalism, the electric field that crosses a waveplate is related to the incident electric field by the transfert matrix M, given by [131]

$$M(\phi,\theta) = \begin{pmatrix} cos\frac{\phi}{2} + icos2\theta sin\frac{\phi}{2} & isen2\theta sin\frac{\phi}{2} \\ -isin2\theta sin\frac{\phi}{2} & cos\frac{\phi}{2} - icos2\theta sin\frac{\phi}{2} \end{pmatrix}, \tag{A.3}$$

where ϕ is the retardation of the wave plate (π for the half-waveplate and $\pi/2$ for the quarter-waveplate, to be more explored ahead) and θ is the angle of the waveplate with respect to its axis.

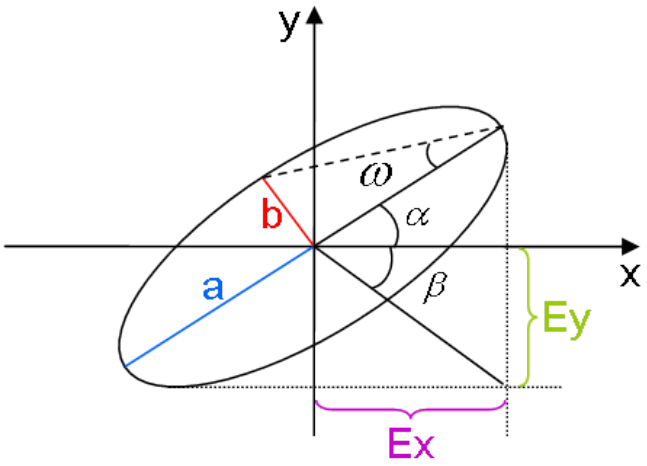

Figure A.1: Representation of angles in the rotation of an elliptically polarized beam. α corresponds to the rotation of the ellipse axis and $\varepsilon = tg\omega = b/a$ corresponds to its ellipticity.

A.1 Rotation

An elliptically polarized beam that has crossed a half-waveplate ($\lambda/2$) placed at $22,5°$ is described by

$$\begin{pmatrix} E'_x \\ E'_y \end{pmatrix} = M\left(\pi, \frac{\pi}{8}\right)\begin{pmatrix} E_x \\ E_y \end{pmatrix} = i\frac{\sqrt{2}}{2}\begin{pmatrix} 1 & 1 \\ 1 & -1 \end{pmatrix}\begin{pmatrix} cos\beta e^{-i\frac{\Delta}{2}} \\ sin\beta e^{i\frac{\Delta}{2}} \end{pmatrix}. \tag{A.4}$$

Considering that the intensity is divided by two when the beam crosses the polarizing cube, the difference of intensity measured in the two arms of the polarization bridge is then given by

$$\Delta I' = I'_x - I'_y = \left|\frac{E'_x}{\sqrt{2}}\right|^2 - \left|\frac{E'_y}{\sqrt{2}}\right|^2 = \frac{1}{2}sin2\beta cos\Delta. \tag{A.5}$$

Trigonometric relations allow to prove that $sin2\omega = (sin2\beta sin\Delta)/2$ and $tg\Delta = \frac{tg2\omega}{sin2\alpha}$. With that, we have

$$\Delta I' = \frac{1}{2}cos2\omega sin2\alpha. \tag{A.6}$$

As $\alpha \to 0$ and $\omega \to 0$, one can use the Taylor expansion of the sine and of the cosines to the second order, so

$$\Delta I' = \frac{1}{2}\left(1 - \frac{(2\omega)^2}{2!}\right)\left(2\alpha - \frac{(2\alpha)^3}{3!}\right). \tag{A.7}$$

The terms in ω^2 and in α^3 tend to zero and we have then

$$\boxed{\Delta I' \approx \alpha}\,. \tag{A.8}$$

On one hand, the pure Faraday rotation is extracted from the results by making the difference of the signal for the two directions of the external magnetic field, this way, only the magnetic contribution is not zero. The static magneto-optical rotation is then given by

$$S_{MO}^{ROT} = S_{H+}^{ROT} - S_{H-}^{ROT} = \Delta I'_{H+} - \Delta I'_{H-} = (I'_x - I'_y)_{H+} - (I'_x - I'_y)_{H-}. \tag{A.9}$$

where x and y represent the two arms of the polarization bridge.

The transmission signal is obtained by measuring only one arm of the bridge, signal this that contains the transmission information and half of the magnetic signal. In order to eliminate this last one, one can do the sum of I_x and I_y to obtain the pure optical response.

A.2 Ellipticity

The use of a quarter-wave plate, when combined with a half-waveplate allows to obtain the ellipticity of the polarization. A elliptically polarized beam that has crossed a quarter-waveplate ($\lambda/4$) at 0° and a half-waveplate ($\lambda/2$) at $22,5°$ is then described by

$$\begin{pmatrix} E''_x \\ E''_y \end{pmatrix} = M\left(\pi, \frac{\pi}{8}\right) M\left(\frac{\pi}{2}, 0\right) \begin{pmatrix} E_x \\ E_y \end{pmatrix} = \begin{pmatrix} e^{i\pi/4} & e^{-i\pi/4} \\ e^{i\pi/4} & -e^{-i\pi/4} \end{pmatrix} \begin{pmatrix} cos\beta e^{-i\frac{\Delta}{2}} \\ sin\beta e^{i\frac{\Delta}{2}} \end{pmatrix}. \tag{A.10}$$

Considering again that the intensity is divided by two when the beam crosses the cube, the difference of intensity measured in the two arms of the polarization bridge is then given by

$$\Delta I'' = I''_x - I''_y = \left|\frac{E''_x}{\sqrt{2}}\right|^2 - \left|\frac{E''_y}{\sqrt{2}}\right|^2 = \frac{1}{2} sin2\beta cos\Delta. \tag{A.11}$$

Using that $sin2\omega = (sin2\beta sin\Delta)/2$, we have

$$\Delta I'' = \frac{1}{2} sin2\omega. \tag{A.12}$$

As $\alpha \to 0$, one can use the Taylor expansion of the sine to the second order, so

$$\Delta I'' = \frac{1}{2}\left(2\omega - \frac{(2\omega)^3}{3!}\right). \tag{A.13}$$

The terms in ω^3 tends to zero and we have then

$$\Delta I'' \approx \omega. \tag{A.14}$$

As $\omega \to 0$, $\omega \approx tg\omega \approx \varepsilon$, so

$$\boxed{\Delta I'' \approx \varepsilon}\,. \tag{A.15}$$

In the frame of equation A.9, the static elipticity is given by

$$S_{MO}^{ELL} = S_{H+}^{ELL} - S_{H-}^{ELL} = \Delta I''_{H+} - \Delta I''_{H-} = (I''_x - I''_y)_{H+} - (I''_x - I''_y)_{H-}. \tag{A.16}$$

A.3 Conclusions

The differentiation in this method allows great signal to noise ratio as it eliminates fluctuations in a single arm of the bridge. However, a large spectral bandwitdth of the laser can be a limitation due dispersion properties of optics in the bridge.

Rotation and elipticity are linked to the magnetization by considering the nondiagonal terms of the dielectric tensor and these last ones can be obtained from magneto-optical pump and probe measurements as shown in reference [42] and in section 1.2.3.

Bibliography

[1] E. Beaurepaire, J.-C. Merle, A. Daunois, and J.-Y. Bigot. Ultrafast spin dynamics in ferromagnetic nickel. *Physical Review Letters*, 76(22):4250–4253, 1996.

[2] M. Faraday. On the magnetization of light and the illumination of magnetic lines of force. *Philosophical Transactions of the Royal Society of London*, 136:1–20, 1846.

[3] J. Kerr. On rotation of the plane of polarization by reflection from the pole of a magnet. *Philosophical Magazine Series 5*, 3, 1877.

[4] J.-Y. Bigot, M. Vomir, and E. Beaurepaire. Coherent ultrafast magnetism induced by femtosecond laser pulses. *Nature Physics*, 5(7):515–520, 2009.

[5] V. Joch, P. Molho, and L. Ranno. Magnetization dynamics in a dot of ferrimagnetic garnet near the compensation temperature. *Journal of Physics: Conference Series*, 303(012006), 2011.

[6] B. Ferrand, B. Chambaz, and M. Couchaud. Liquid phase epitaxy: A versatile technique for the development of miniature optical components in single crystal dielectric media. *Optical Materials*, 11:101–114, 1999.

[7] D. L. Wood and K. Nassau. Optical properties of gadolinium gallium garnet. *Applied Optics*, 29(25):3704–3707, 1990.

[8] J.B. Kortright, D.D. Awschalom, J. Stohr, S.D. Bader, Y.U. Idzerda, S.S.P. Parkin, Ivan K. Schuller, and H.-C. Siegmann. Research frontiers in magnetic materials at soft x-ray synchrotron radiation facilities. *Journal of Magnetism and Magnetic Materials*, 207:7–44, 1999.

[9] J.-Y. Bigot and M. Vomir. Ultrafast magnetization dynamics of nanostructures. *Annalen der Physik*, 525(1-2):2–30, 2013.

[10] J.-Y. Bigot. Femtosecond magneto-optical processes in metals. *Comptes Rendus de l'Académie des Sciences de Paris*, Série IV:1483–1504, 2001.

[11] M. Vomir. *Trajectoire d'aimantation induite par des impulsions laser femtosecondes: Etude tridimensionelle des effets d'anisotropie*. PhD thesis, Université de Strasbourg, 2006.

[12] F. Vallée. Ultrafast spectroscopy of metals. *Comptes Rendus de l'Académie des Sciences de Paris*, Série IV:1469–1482, 2001.

[13] J. G. Fujimoto, J. M. Liu, E. P. Ippen, and N. Bloembergen. Femtosecond laser interaction with metallic tungsten and nonequilibrium electron and lattice temperatures. *Physical Review Letters*, 53:1837–1840, 1984.

[14] K. M. Yoo, X. M. Zhao, M. Siddique, R. R. Alfano, D. P. Osterman, M. Radparvar, and J. Cunniff. Femtosecond thermal modulation measurements of electron-phonon relaxation in niobium. *Applied Physics Letters*, 56:1908–1910, 1990.

[15] C.-K. Sun, F. Vallée, L. Acioli, E. P. Ippen, and J. G. Fujimoto. Femtosecond investigation of electron thermalization in gold. *Physical Review B*, 48:12365–12368, 1993.

[16] P. Wiess. L'hypothèse du champ moléculaire et la propriété ferromagnétique. *Journal of Theoretical and Applied Physics*, 6(1):661–690, 1907.

[17] W. Heisenberg. Zur theorie des ferromanetismus. *Zeitschrift fr Physic A Hadrons and Nuclei*, 49:619–636, 1928.

[18] E. C. Stoner. Collective electrons ferromagnetism. *Proceeding of the Royal Society of London A*, 165:372–414, 1938.

[19] E. C. Stoner and E. P. Wohlfarth. A mechanism of magnetic hysteresis inheterogeneous alloys. *Phylosophical Transactions of the Royal Society of London A*, 240(826):599–642, 1948.

[20] G. L. Eesley. Observation of nonequilibrium electron heating in copper. *Physical Review Letters*, 51:2140–2143, 1983.

[21] G. L. Eesley. Generation of nonequilibrium electron and lattice temperatures in copper by picosecond laser pulses. *Physical Review B*, 33:2144–2151, 1986.

[22] H. E. Elsayed-Ali, T. B. Norris, M. A. Pessot, and G. A. Mourou. Time-resolved observation of electron-phonon relaxation in copper. *Physical Review Letters*, 58:1212–1215, 1987.

[23] R. W. Schoenlein, W. Z. Lin, J. G. Fujimoto, and G. L. Eesley. Femtosecond studies of nonequilibrium electronic processes in metals. *Physical Review Letters*, 58:1680–1683, 1987.

[24] W. S. Fann, R. Storz, H. W. K. Tom, and J. Bokor. Direct measurement of nonequilibrium electron-energy distributions in subpicosecond laser-heated gold films. *Physical Review Letters*, 68:2834–2837, 1992.

[25] M. Aeschlimann, M. Bauer, and S. Pawlik. Competing nonradiative channels for hot electron induced surface photochemistry. *Chemical Physics*, 205(1-2):127–141, 1996.

[26] S. Ogawa, H. Nagano, H. Petek, and A. P. Heberle. Optical dephasing in Cu(111) measured by interferometric two-photon time-resolved photoemission. *Physical Review Letters*, 78:1339–1342, 1997.

[27] J. Hohlfeld, S.-S. Wellershoff, J. Gudde, U. Conrad, V. Jahnke, and E. Matthias. Electron and lattice dynamics following optical excitation of metals. *Chemical Physics*, 251(1-3):237–258, 2000.

[28] N. Del Fatti and F. Vallée. Ultrafast electron interactions in metal clusters. *Comptes Rendus Physique*, 3(3):365–380, 2002.

[29] S. I. Ashitkov M. B. Agranat, A. B. Granovskii, and G. I. Rukman. Interaction of picosecond laser pulses with the electron, spin and phonon subsystems of nickel. *Sov. Phys. Journal of Experimental and Theoretical Physics*, 59(4):804–805, 1984.

[30] A. Vaterlaus, T. Beutler, and F. Meier. Spin-lattice relaxation time of ferromagnetic gadolinium determined with time-resolved spin-polarized photoemission. *Physical Review Letters*, 67:3314–3317, 1991.

[31] W. Hubner and K. H. Bennemann. Simple theory for spin-lattice relaxation in metallic rare-earth ferromagnets. *Physical Review B*, 53:3422–3427, 1996.

[32] T. Ogasawara, K. Ohgushi, Y. Tomioka, K. S. Takahashi, H. Okamoto, M. Kawasaki, and Y. Tokura. General features of photoinduced spin dynamics in ferromagnetic and ferrimagnetic compounds. *Physical Review Letters*, 94:087202, 2005.

[33] J. Hohlfeld, E. Matthias, R. Knorren, and K. H. Bennemann. Nonequilibrium magnetization dynamics of nickel. *Physical Review Letters*, 78(25):4861–4864, 1997.

[34] J. Gudde, U. Conrad, V. Jahnke, J. Hohlfeld, and E. Matthias. Magnetization dynamics of Ni and Co films on Cu(001) and of bulk nickel surfaces. *Physical Review B*, 59:R6608–R6611, 1999.

[35] A. Scholl, L. Baumgarten, R. Jacquemin, and W. Eberhardt. Ultrafast spin dynamics of ferromagnetic thin films observed by fs spin-resolved two-photon photoemission. *Physical Review Letters*, 79(25):5146–5149, 1997.

[36] E. Beaurepaire, M. Maret, V. Halté, J.-C. Merle, A. Daunois, and J.-Y. Bigot. Spin dynamics in $CoPt_3$ alloy films: A magnetic phase transition in the femtosecond scale. *Physical Review B*, 58(18):12134–12137, 1998.

[37] U. Conrad, J. Gudde, V. Jahnke, and E. Matthias. Ultrafast electron and magnetization dynamics of thin Ni and Co films on $Cu(001)$ observed by time-resolved SHG. *Applied Physics B*, 68:511–517, 1999.

[38] L. Néel. Théorie du traînage magnétique des ferromagnétiques en grains fins avec application aux terres cuites. *Annales de Géophysique*, 5:99–136, 1949.

[39] W. F. Brown. Thermal fluctuations of a single-domain particle. *Physical Review*, 130:1677–1686, 1963.

[40] W. Wernsdorfer, E. Bonet Orozco, K. Hasselbach, A. Benoit, B. Barbara, N. Demoncy, A. Loiseau, H. Pascard, and D. Mailly. Experimental evidence of the Néel-Brown model of magnetization reversal. *Physical Review Letters*, 78:1791–1794, 1997.

[41] B. Koopmans, M. van Kampen, J. T. Kohlhepp, and W. J. M. de Jonge. Ultrafast magneto-optics in nickel: magnetism or optics? *Physical Review Letters*, 85(4):844–847, 2000.

[42] L. Guidoni, E. Beaurepaire, and J.-Y. Bigot. Magneto-optics in the ultrafast regime: Thermalization of spin populations in ferromagnetic films. *Physical Review Letters*, 89(1):017401, 2002.

[43] C. Boeglin, E. Beaurepaire, V. Halté, V. López-Flores, C. Stamm, N. Pontius, H. A. Durr, and J.-Y. Bigot. Distinguishing the ultrafast dynamics of spin and orbital moments in solids. *Nature Letters*, 465:458–462, 2010.

[44] G. Ju, A. Vertikov, A. V. Nurmikko, C. Canady, G. Xiao, R. F. C. Farrow, and A. Cebollada. Ultrafast nonequilibrium spin dynamics in a ferromagnetic thin film. *Physical Review B*, 57(2):700–703, 1998.

[45] G. Ju, A. V. Nurmikko, R. F. C. Farrow, R. F. Marks, M. J. Carey, and B. A. Gurney. Ultrafast time resolved photoinduced magnetization rotation in a ferromagnetic/antiferromagnetic exchange coupled system. *Physical Review Letters*, 82(18):3705–3708, 1999.

[46] B. Koopmans, J. J. M. Ruigrok, F. Dalla Longa, and W. J. M. de Jonge. Unifying ultrafast magnetization dynamics. *Physical Review Letters*, 95(267207), 2005.

[47] M. Vomir, L. H. F. Andrade, L. Guidoni, E. Beaurepaire, and J.-Y. Bigot. Real space trajectory of the ultrafast magnetization dynamics in ferromagnetic metals. *Physical Review Letters*, 94(237601):237601, 2005.

[48] J.-W. Kim, M. Vomir, and J.-Y. Bigot. Ultrafast magnetoacoustics in nickel films. *Physical Review Letters*, 109:166601, 2012.

[49] L. H. Andrade, M. Vomir, J.-W. Kim, M. Sanches Piaia, A. D. Santos, and J.-Y. Bigot. Ultrafast demagnetization and precession damping times in rare earth doped cobalt films. page QW3D.6, 2013.

[50] A. V. Kimel, A. Kirilyuk, P. A. Usachev, R. V. Pisarev, M. Balbashov, and T. Rasing. Ultrafast non-thermal control of magnetization by instantaneous photomagnetic pulses. *Nature Letters*, 435:655–657, 2005.

[51] A. Kirilyuk, A. V. Kimel, and T. Rasing. Ultrafast optical manipulation of magnetic order. *Reviews of Modern Physics*, 82:2731–2784, 2010.

[52] F. Hansteen, A. Kimel, A. Kirilyuk, and T. Rasing. Nonthermal ultrafast optical control of the magnetization in garnet films. *Physical Review B*, 73:014421, 2006.

[53] A. Kirilyuk, A. V. Kimel, and T. Rasing. Laser-induced magnetization dynamics and reversal in ferrimagnetic alloys. *Reports on Progress in Physics*, 76:1–35, 2013.

[54] K. Vahaplar, A. M. Kalashnikova, A. Kimel, D. Hinzke, U. Nowak, R. Chantrell, A. Tsukamoto, A. Itoh, A. Kirilyuk, and T. Rasing. Ultrafast path for optical magnetization reversal via a strongly non-equilibrium state. *Physical Review Letters*, 103:117201, 2009.

[55] V. L. Vinetskii, N. V. Kukhtarev, S. G. Odulov, and M. S. Soskin. Dynamic self-diffraction of coherent light beams. *Soviet Physics Uspekhi*, 22(9):742–756, 1979.

[56] C. V. Raman and K. S. Krishnan. A new type of secondary radiation. *Nature*, 121:501–502, 1928.

[57] P. A. Franken, A. E. Hill, C.W. Peters, and G.Weinreich. Generation of optical harmonics. *Physical Review Letters*, 7(4), 1961.

[58] F. U. Hillebrecht. *Magnetism goes nano*, chapter B4 - Magnetooptics. 2005.

[59] M. Joffre. Optique non-linéaire en régimes continu et femtoseconde. Master Physique et Applications (M2) - Ecole Polytechnique - Ecole Normale Supérieure - Université Pierre et Marie Curie - Université Paris Sud, 214.

[60] J.-C. Diels and W. Rudolph. *Ultrashort laser pulse phenomena.* Academic Press, 1996.

[61] A. Huynh. *Dynamique cohérente des polaritons de microcavité de semiconducteurs.* PhD thesis, Ecole Normale Supérieure - Université Paris VI, 2002.

[62] N. A. Kurnit, I. D. Abella, and S. R. Hartmann. Observation of a photon echo. *Physical Review Letters*, 13(19):567–568, 1964.

[63] I. D. Abella, N. A. Kurnit, and S. R. Hartmann. Photon echoes. *Physical Review*, 141(1):391–406, 1966.

[64] S. I. Anisimov, B. L. Kapeliovich, and T. L. Perel'man. Electron emission from metal surfaces exposed to ultrashort laser pulses. *Sov. Phys. Journal of Experimental and Theoretical Physics*, 39(2):375–377, 1974.

[65] M. Kaganov, I. Lifshits, and L. Tanatarov. Relaxation between electrons and the crystalline lattice. *Sov. Phys. Journal of Experimental and Theoretical Physics*, 4, 1957.

[66] C. Kittel. *Introduction to solid state physics.* John Wiley and Sons, Inc., 2005.

[67] L. Landau and E. Lifshits. On the theory of the dispersion of the magnetic permeability in ferromagnetic bodies. *Phys. Zeitsch. der Sowjetunion*, 8:153–169, 1935.

[68] A. Aharoni. *Introduction to the theory of ferromagnetism.* Oxford University Press, 1996.

[69] A. H. Morrish. *The physical principles of magnetism.* John Wiley and Sons, Inc., 1966.

[70] T. L. Gilbert. A lagrangian formulation of the gyromagnetic equation of the magnetic field. *Physical Review*, 100:1243, 1955.

[71] T. L. Gilbert. A phenomenological theory of damping in ferromagnetic materials. *IEEE Transactions on Magnetics*, 40:3443–3449, 2004.

[72] F. Bloch. Nuclear induction. *Physical Review*, 70:460–474, 1946.

[73] N. Bloembergen. On the ferromagnetic resonance in nickel and supermalloy. *Physical Review*, 78:572–580, 1950.

[74] J.-Y. Bigot, M. Vomir, L.H.F. Andrade, and E. Beaurepaire. Ultrafast magnetization dynamics in ferromagnetic cobalt: The role of the anisotropy. *Chemical Physics*, 318(1-2):137–146, 2005.

[75] W. Voigt. *Magneto- und Electro-Optik*. Teubner, 1908.

[76] P. Argyres. Theory of Faraday and Kerr effects in ferromagnetics. *Physical Review*, 97(2):334–345, 1955.

[77] H. Haag, P. Gilliot, R. Lévy, B. Honerlage, O. Briot, S. Ruffenach-Clur, and R. L. Aulombard. Degenerate four-wave mixing experiments on GaN in the quasistationary regime. *Applied Physics Letters*, 74:1436–1438, 1999.

[78] E. Vanagas, J. Kudrna, D. Brinkmann, P. Gilliot, and B. Honerlage. Phase relaxation dynamics of excitons and biexcitons in $CuCl$ studied by femtosecond and picosecond degenerate four-wave mixing. *Physical Review B*, 63:153201, 2001.

[79] P. Gilliot, S. Cronenberger, H. Rahimpour Soleimani, C. Brimont, O. Crégut, M. Gallart, and B. Honerlage. Measurement of exciton spin coherence by non-degenerate four-wave mixing experiments in the $\chi^{(3)}$ regime. *Physical Review B*, 75:125209, 2007.

[80] G. Stibenz, C. Ropers, Ch. Lienau, Ch. Warmuth, A. S. Wyatt, I. A. Walmsley, and G. Steinmeyer. Advanced methods for the characterization of few-cycle pulses: a comparison. *Applied Physics B*, 83:511–519, 2006.

[81] E. Hetch. *Optics*. Addison-Wesley Publishing Company, 1974.

[82] C. Cohen-Tannoudji, B. Diu, and F. Laloe. *Mécanique quantique I*. Hermann Éditeurs des Sciences et des Arts, 1998.

[83] H. Vonesch. *Magnéto-optique ultra-rapide cohérente*. PhD thesis, Université de Strasbourg, 2011.

[84] H. Vonesch and J.-Y. Bigot. Ultrafast spin-photon interaction investigated with coherent magneto-optics. *Physical Review B*, 85(180407(R)), 2012.

[85] Y. Hinschberger and P.-A. Hervieux. Foldy-Wouthuysen transformation applied to the interaction of an electron with ultrafast electromagnetic fields. *Physics Letters A*, 376:813–819, 2012.

[86] L. L. Foldy and S. A. Wouthuysen. On the Dirac theory of spin 1/2 particles and its non-relativistic limit. *Physical Review*, 78(1):29–36, 1950.

[87] S. Mukamel. *Principles of nonlinear optical spectroscopy.* Oxford University Press, 1999.

[88] C. H. Brito Cruz, J. P. Gordon, P. C. Becker, R. L. Fork, and C. V. Shank. Dynamics of spectral hole burning. *IEEE Journal of Quantum Eletronics*, 24(2):261–269, 1988.

[89] G. F. Dionne and G. A. Allen. Molecular-orbital analysis of magneto-optical $Bi - O - Fe$ hybrid excited states. *Journal of Applied Physics*, 75(10):6372–6374, 1994.

[90] G. F. Dionne and G. A. Allen. Spectral origins of giant Faraday rotation and ellipticity in Bi-substituted magnetic garnets. *Journal of Applied Physics*, 73(10):6127–6129, 1994.

[91] S. Wittekoek, T. J. A. Popma, J. M. Robertson, and P. F. Bongers. Magneto-optic spectra and the dieletric tensor elements of bismuth-substituted iron garnets at photon energies between $2.2 - 5.2eV$. *Physical Review B*, 12(7):2777–2788, 1975.

[92] W. A. Crossley, R. W. Cooper, and J. L. Page. Faraday rotation in rare-earth iron garnets. *Physical Review*, 181(2):896–904, 1969.

[93] F. Hansteen, L. E. Helseth, O. Hunderi, A. Kirilyuk, and T. Rasing. Optical and magnetooptical properties of bismuth and gallium substituted iron garnet films. *Thin Solid Films*, 455-456:429–432, 2004.

[94] P. Hansen, C.-P. Klages, J. Schuldt, and K. Witter. Magnetic and magneto-optical properties of bismuth-substituted lutenium iron garnet films. *Physical Review B*, 31(9):5858–5864, 1985.

[95] B. Vertruyen, R. Cloots, J. S. Abell, T. J. Jackson, R. C. da Silva, E. Popova, and N. Keller. Curie temperature, exchange integrals and magneto-optical properties in off-stoichiometric bismuth iron garnet epitaxial films. *Physical Review B*, 78(9):094429, 2008.

[96] T. Oikawa, S. Suzuki, and K. Nakao. First principles study of spin-orbit interactions in bismuth iron garnet. *Journal of the Physics Society of Japan*, 74(401), 2005.

[97] L. E. Helseth, R. W. Hansen, E. I. Il'yashenko, M. Baziljevich, and T. H. Johansen. Faraday rotation spectra of bismuth-substituted ferrite garnet films with in-plane magnetization. *Physical Review B*, 64(174406), 2001.

[98] M. Deb, E. Popova, A. Fouchet, and N. Keller. Magneto-optical Faraday spectroscopy of completely bismuth-substituted $Bi_3Fe_5O_{12}$ garnet thin films. *Journal of Physics D: Applied Physics*, 45(455001), 2012.

[99] M. F. Armand, J. Daval, B. Ferrand, and H. Moriceau. Fascicule de brevet européen. EP 0186528 B1, 1989.

[100] W. E. Lamb Jr. Theory of an optical maser. *Physical Review*, 134:A1429–A1450, 1964.

[101] L. E. Hargrove, R. L. Fork, and M. A. Pollack. Locking of He-Ne laser modes induced by synchronous intracavity modulation. *Applied Physics Letters*, 5:4–5, 1964.

[102] T. Brabec, C. Spielmann, P. F. Curley, and F. Krausz. Kerr lens mode locking. *Optics Letters*, 17(18):1292–1294, 1992.

[103] K. F. Wall and A. Sanchez. Titanium sapphire laser. *The Lincoln Laboratory Journal*, 3(3):447–462, 1990.

[104] P. F. Moulton. Titanium-doped sapphire tunable solid state laser. *Optics News*, 8:9, 1982.

[105] P. F. Moulton. Spectroscopic and laser characteristics of $Ti : Al_2O_3$. *Journal of the Optical Society of America B*, 3(1):125–133, 1986.

[106] W. R. Rapoport and C. P. Khattak. Efficient, tunable Ti:sapphire laser. *Tunable solid-state lasers II - Springer Series in Optical Sciences*, 52:212–217, 1986.

[107] D. E. Spence, P. N. Kean, and W. Sibbett. $60 - fsec$ pulse generation from a self-mode-locked Ti:sapphire laser. *Optics Letters*, 16(1):42–44, 1991.

[108] H. A. Haus, J. G. Fujimoto, and E. P. Ippen. Analytic theory of additive pulse and Kerr lens mode locking. *IEEE Journal of Quantum Eletronics*, 28(10):2086–2096, 1992.

[109] R. Szipöcs, K. Ferencz, C. Spielmann, and F. Krausz. Chirped multilayer coatings for broadband dispersion control in femtosecond lasers. *Optics Letters*, 19(3):201–203, 1994.

[110] A. Stingl, M. Lenzner, C. Spielmann, F. Krausz, and R. Szipocs. Sub-10-fs mirror-dispersed-controlled Ti:sapphire laser. *Optics Letters*, 20(6):602–604, 1995.

[111] M. T. Asaki, C. Huang, D. Garvey, J. Zhou, H. C. Kapteyn, and M. M. Murnane. Generation of 11-fs pulses from a self-mode-locked Ti:sapphire laser. *Optics Letters*, 18(12):977–979, 1993.

[112] J. Zhou, G. Taft, C. Huang, M. M. Murnane, H. C. Kapteyn, and I. P. Christov. Pulse evolution in a broad-bandwidth Ti:sapphire laser. *Optics Letters*, 19(15):1149–1151, 1994.

[113] U. Morgner, F. X. Kärtner, S. H. Cho, Y. Chen, H. A. Haus, J. G. Fujimoto, E. P. Ippen, V. Scheuer, G. Angelow, and T. Tschudi. Sub-two-cycle pulses from a Kerr-lens mode-locked Ti:sapphire laser. *Optics Letters*, 24:411–413, 1999.

[114] D. H. Sutter, G. Steinmeyer, L. Gallmann, N. Matuschek, F. Morier-Genoud, U. Keller, V. Scheuer, G. Angelow, and T. Tschudi. Semiconductor saturable-absorber mirror-assisted Kerr-lens mode-locked Ti:sapphire laser producing pulses in the two-cycle regime. *Optics Letters*, 24(9):631–633, 1999.

[115] D. W. Piston, J. C. Long, and M. W. Davidson. Ti:sapphire mode-locked lasers. http://www.olympusmicro.com/primer/java/lasers/tsunami/.

[116] P. Maine, D. Strickland, P. Bado, M. Pessot, and G. Mourou. Generation of ultra-high peak power pulses by chirped pulse amplification. *IEEE Journal of Quantum Eletronics*, 24:398–403, 1988.

[117] A. Offner. U.S. patent. 3.748.015, 1971.

[118] J. E. Murray and W. H. Lowdermilk. Nd-YAG regenerative amplifier. *Journal of Applied Physics*, 51:3548–3555, 1980.

[119] J. P. Gordon and R. L. Fork. Optical resonator with negative dispersion. *Optics Letters*, 9(5):153–155, 1984.

[120] R. L. Fork, O. E. Martinez, and J. P. Gordon. Negative dispersion using pairs of prisms. *Optics Letters*, 9(5):150–152, 1984.

[121] Newport Corporation. *Application Note - Prism compressor for ultrashort laser pulses.*

[122] G. Ghosh. *Handbook of thermo-optic coefficients of optical materials with applications.* Academic Press, 1998.

[123] J.-C. M. Diels, J. J. Fontaine, I. C. McMichael, and F. Simoni. Control and measurement of ultrashort pulse shapes (in amplitude and phase) with femtosecond accuracy. *Applied Optics*, 24(9):1270–1282, 1985.

[124] D. J. Kane and R. Trebino. Characterization of arbitrary femtosecond pulses using frequency resolved optical gating. *IEEE Journal of Quantum Eletronics*, 29(2):571–579, 1993.

[125] C. Iaconis and I. A. Walmsley. Spectral phase interferometry for direct electric-field reconstruction of ultrashort optical pulses. *Optics Letters*, 23(10):792–794, 1998.

[126] V. Wong and I. A. Walmsley. Analysis of ultrashort pulse-shape measurement using linear interferometers. *Optics Letters*, 19(4):287–289, 1994.

[127] J.-Y. Bigot, E. Beaurepaire L. Guidoni, and P. N. Saeta. Femtosecond spectrotemporal magneto-optics. *Physical Review Letters*, 93(7):077401, 2004.

[128] M. Barthelemy, M. Vomir, M. Sanches Piaia, H. Vonesch, P. Molho, B. Barbara, and J.-Y. Bigot. Coherent magnetism and spin-orbit interaction in garnet films probed with femtosecond magneto-optical four wave mixing. arXiv:1311.0080 [cond-mat.mes-hall] (2013).

[129] M. Barthelemy, M. Vomir, M. Sanches Piaia, and J.-Y. Bigot. Coherent magnetization dynamics investigated with magneto optical four wave mixing. page QW3D.4, 2013.

[130] F. Hansteen, A. Kimel, A. Kirilyuk, and T. Rasing. Femtosecond photomagnetic switching of spins in ferrimagnetic garnet films. *Physical Review Letters*, 95:047402, 2005.

[131] S. Huard. *Polarisation de la lumière*. Masson, 1994.